

硕士学位论文

常压下镍氧化物薄膜超导电性的研究

**IN SEARCH OF SUPERCONDUCTIVITY IN
NICKELATE THIN FILMS
AT AMBIENT PRESSURE**

研 究 生：聂子豪

指 导 教 师：陈卓昱副教授

南方科技大学

二〇二六年六月

国内图书分类号：O469
国际图书分类号：538.9

学校代码：14325
密级：公开

物理学硕士学位论文

常压下镍氧化物薄膜超导电性的研究

学位申请人：聂子豪

指导教师：陈卓昱副教授

学科名称：物理学

答辩日期：2026年5月

培养单位：物理系

学位授予单位：南方科技大学

IN SEARCH OF SUPERCONDUCTIVITY IN NICKELATE THIN FILMS AT AMBIENT PRESSURE

A dissertation submitted to
Southern University of Science and Technology
in partial fulfillment of the requirement
for the degree of
Master of Science
in
Physics

by
Zihao Nie

Supervisor : Associate Prof. Zhuoyu Chen

May, 2026

学位论文公开评阅人和答辩委员会名单

公开评阅人名单

无（全隐名评阅）

答辩委员会名单

| | | | |
|----|-----|--------|------------------|
| 主席 | 王取泉 | 教授 | 南方科技大学 |
| 委员 | 陈卓昱 | 副教授 | 南方科技大学 |
| | 黄浩亮 | 副研究员 | 粤港澳大湾区 量子科学中心 |
| 秘书 | 李月莹 | 研究助理教授 | 南方科技大学 |

DECLARATION OF ORIGINALITY AND AUTHORIZATION OF THESIS, SOUTHERN UNIVERSITY OF SCIENCE AND TECHNOLOGY

Declaration of Originality of Thesis

I hereby declare that this thesis is my own original work under the guidance of my supervisor. It does not contain any research results that others have published or written. All sources I quoted in the thesis are indicated in references or have been indicated or acknowledged. I shall bear the legal liabilities of the above statement.

Signature: 聂子豪

Date: 2026.04.20

Declaration of Authorization of Thesis

I fully understand the regulations regarding the collection, retention, and use of the thesis of the Southern University of Science and Technology.

1. Submit the electronic version of the thesis as required by the University.
2. The University has the right to retain and send the electronic version to other institutions that allow the thesis to be read by the public.
3. The University may save all or part of the thesis in certain databases for retrieval and may save it with digital, cloud storage, or other methods for teaching and scientific research. I agree that the full text of the thesis can be viewed online or downloaded within the campus network.

(1) I agree that once submitted, the thesis can be retrieved online and the first 16 pages can be viewed within the campus network.

(2) I agree that ☒ upon submission/ ☐ _____ months after submission, the full text of the thesis can be viewed and downloaded by the public.

4. This authorization applies to the decrypted confidential thesis.

Signature of Author: 聂子豪

Date: 2026.04.20

Signature of Supervisor: 陈卓星

Date: 2026.04.20

摘 要

2019 年发现的镍基超导体已成为研究非常规超导的一个新兴重要平台。其中一类体系为无限层及多层方平面相，其费米面主要由 Ni 的 $d_{x^2-y^2}$ 轨道主导，在晶体结构和电子结构上与铜氧化物相似。另一类体系为 Ruddlesden-Popper (RP) 相镍氧化物，其中的双层相 $\text{La}_3\text{Ni}_2\text{O}_7$ 在高压下具有超导电性且超导转变起始温度接近 80 K。 $\text{La}_3\text{Ni}_2\text{O}_7$ 与方平面相之间的一个关键结构差异在于其内部顶角氧原子的存在。这些顶角氧介导了 Ni d_z 轨道间的层间耦合，形成一个被称为 γ 带的成键能带。高压下该能带穿过费米面被认为是超导出现的关键因素。然而，由于先前实现 $\text{La}_3\text{Ni}_2\text{O}_7$ 的超导均需要高压条件，角分辨光电子能谱 (ARPES) 无法探测其超导态下的电子结构。因此，实现 $\text{La}_3\text{Ni}_2\text{O}_7$ 的常压超导并探测其电子能带结构是一个关键的科学问题。

本论文系统研究了双层 RP 相镍氧化物薄膜及其相关的混合超结构中常压超导的实现及其内在机制。具体研究工作如下：

(1) 首先，本工作发展了强氧化原子逐层外延 (GAE) 技术，用于复杂 RP 相镍氧化物薄膜的生长。GAE 所具有的稳健生长动力学实现了结构相形成与氧化学计量调控的解耦。为实现高质量双层 RP 相镍氧化物薄膜的精确逐层外延生长，建立了一套阳离子化学剂量校准方案。进一步，在生长过程中引入高浓度臭氧，有效抑制了薄膜中的氧空位。

(2) 其次，实现了双层 RP 相镍氧化物薄膜 $\text{La}_{2.85}\text{Pr}_{0.15}\text{Ni}_2\text{O}_7$ 的常压超导。由 SrLaAlO_4 提供的外延压缩应变及优化的氧化学计量共同稳定该超导态。零电阻和迈斯纳抗磁效应的双重证据证实了其超导本质。其超导转变起始温度约为 45 K，超过 McMillan 极限。

(3) 最后，在 SrLaAlO_4 衬底上制备的 $(\text{La}_{0.67}\text{Pr}_{0.33})_5\text{Ni}_3\text{O}_{11}$ (1212 相) 和 $(\text{La}_{0.67}\text{Pr}_{0.33})_7\text{Ni}_5\text{O}_{17}$ (2323 相) 镍氧化物混合超结构中实现了常压超导。在相同应变条件下，混合 $(\text{La}_{0.67}\text{Pr}_{0.33})_3\text{Ni}_2\text{O}_7$ (1313 相) 未表现出超导性。通过对这些超结构和纯双层 2222 相开展对比性 ARPES 研究，阐明了超导的电子结构起源。其中，由 d_z 轨道衍生的 γ 能带穿过费米面并形成费米口袋是 RP 相镍氧化物实现超导的关键要素。此发现将 RP 相镍氧化物置于多轨道物理图景中，使其区别于铜氧化物超导体的单能带物理图像。

关键词：镍基超导；RP 相镍氧化物；脉冲激光沉积；角分辨光电子能谱

ABSTRACT

Nickelate superconductors, discovered in 2019, have emerged as a new platform for the intensive study of unconventional superconductivity. One important class comprise the infinite-layer and multilayer square-planar phase whose Fermi surfaces are dominated by the Ni $d_{x^2-y^2}$ orbital, structurally and electronically resembling the cuprates. Another class is the Ruddlesden–Popper (RP) nickelates, in which superconductivity was discovered in pressurized bilayer system $\text{La}_3\text{Ni}_2\text{O}_7$, with a superconducting onset temperature approaching 80 K. A key structural distinction between $\text{La}_3\text{Ni}_2\text{O}_7$ and square-planar nickelates lies in the presence of inner apical oxygen atoms. The interlayer coupling of Ni d_{z^2} orbitals mediated by these apical oxygen gives rise to a bonding band, known as the γ band, whose presence at the Fermi level under high pressure is believed to play a crucial role in the emergence of superconductivity. However, as superconductivity in bilayer RP nickelates was previously achieved only under high pressure, Angle-Resolved Photoemission Spectroscopy (ARPES) cannot be employed to probe the electronic structure of superconducting $\text{La}_3\text{Ni}_2\text{O}_7$. Therefore, the realization of ambient-pressure superconductivity in bilayer RP nickelates and the characterization of their electronic band structures have become important scientific challenges.

This dissertation systematically investigates the realization and underlying mechanisms of ambient-pressure superconductivity in bilayer RP nickelate thin films and related hybrid superstructures. The detailed work is as follows:

(1) First, a Gigantic-Oxidative Atomic-Layer-by-Layer Epitaxy (GAE) methodology is developed for the growth of complex RP nickelate thin films. The robust growth kinetics of GAE decouple structural phase formation from oxygen stoichiometry control. A two-step cation calibration protocol, guided by X-ray diffraction (XRD) patterns, is established to achieve precise atomic-layer-by-layer epitaxy of high-quality bilayer RP nickelate thin films. By leveraging the strong oxidation capability enabled by high-concentration ozone during growth, oxygen vacancies are effectively suppressed in the as-grown films.

(2) Second, ambient-pressure superconductivity is successfully realized in

bilayer RP nickelate thin films, by growing $\text{La}_{2.85}\text{Pr}_{0.15}\text{Ni}_2\text{O}_7$ on SrLaAlO_4 substrates. The superconducting state is stabilized by epitaxial compressive strain and optimized oxygen stoichiometry. The superconducting nature is confirmed by the observation of both zero resistance and the Meissner diamagnetic effect, with an onset temperature of approximately 45 K, notably exceeding the McMillan limit.

(3) Finally, ambient-pressure superconductivity is also realized in $(\text{La}_{0.67}\text{Pr}_{0.33})_5\text{Ni}_3\text{O}_{11}$ (1212 phase) and $(\text{La}_{0.67}\text{Pr}_{0.33})_7\text{Ni}_5\text{O}_{17}$ (2323 phase) nickelate hybrid superstructures grown on SrLaAlO_4 substrates. In contrast, the hybrid $(\text{La}_{0.67}\text{Pr}_{0.33})_3\text{Ni}_2\text{O}_7$ (1313 phase) remains non-superconducting under identical strain conditions. Comparative ARPES studies across these superstructures, together with the pure bilayer 2222 phase, are conducted to elucidate the electronic origin of superconductivity. The d_{z^2} -derived γ band, which forms the underlying Fermi pocket, is identified as the key electronic ingredient for superconductivity in RP nickelates. This finding places RP nickelates in a multi-orbital scenario, distinguishing them from the single-band physics of cuprate superconductors.

Keywords: Nickelate Superconductor; Ruddlesden–Popper Nickelates; Pulsed Laser Deposition; Angle-Resolved Photoemission Spectroscopy

TABLE OF CONTENTS

| | |
|--|----|
| 摘 要 | I |
| ABSTRACT | II |
| CHAPTER 1 INTRODUCTION | 1 |
| 1.1 History of Superconductivity | 1 |
| 1.2 Cuprate Superconductors | 4 |
| 1.3 Nickelate Superconductors | 7 |
| 1.3.1 Ruddlesden–Popper and Square-Planar Nickelates | 7 |
| 1.3.2 Infinite-Layer Nickelate Superconductors | 8 |
| 1.3.3 Bilayer Ruddlesden–Popper Nickelate Superconductors | 14 |
| 1.3.4 Other Nickelate Superconductors | 21 |
| 1.4 Motivation and Thesis Outline | 27 |
| CHAPTER 2 THIN FILM GROWTH OF BILAYER RP NICKELATES VIA GIGANTIC-OXIDATIVE ATOMIC-LAYER-BY-LAYER EPITAXY | 29 |
| 2.1 Comparative Analysis of Conventional PLD and the GAE Growth Mode | 30 |
| 2.2 Decoupling of Phase Formation and Oxygen Stoichiometry in GAE | 33 |
| 2.3 A Two-Step Protocol for Cation Stoichiometry Calibration | 37 |
| 2.4 Summary and Conclusions | 42 |
| CHAPTER 3 AMBIENT-PRESSURE SUPERCONDUCTIVITY ONSET ABOVE 40 K IN (La,Pr) ₃ Ni ₂ O ₇ FILMS | 43 |
| 3.1 Ambient-Pressure Superconductivity in (La,Pr) ₃ Ni ₂ O ₇ Thin Films | 44 |
| 3.2 Thin-Film Growth and Structural Characterization of La _{2.85} Pr _{0.15} Ni ₂ O ₇ on SrLaAlO ₄ Substrates | 47 |
| 3.3 Role of Ozone Annealing and Pr Doping | 49 |
| 3.4 Magnetotransport Properties | 52 |
| 3.5 Thermal Instability | 54 |
| 3.6 Summary and Conclusions | 55 |
| CHAPTER 4 SUPERCONDUCTIVITY AND ELECTRONIC STRUCTURES OF NICKELATE THIN FILM SUPERSTRUCTURES | 56 |
| 4.1 Comparison of Various Superstructures | 58 |

TABLE OF CONTENTS

| | |
|--|-----------|
| 4.2 Thin-Film Growth and Structural Characterization of Nickelate Superstructures | 61 |
| 4.3 Magnetotransport Properties of 1212 and 2323 Films | 67 |
| 4.4 Electronic Band Structures | 70 |
| 4.5 Summary and Conclusions | 73 |
| CHAPTER 5 CONCLUSION AND OUTLOOK | 75 |
| 5.1 Conclusion | 75 |
| 5.2 Outlook | 76 |
| REFERENCES | 77 |
| APPENDIX A AI USAGE DECLARATION | 86 |
| ACKNOWLEDGEMENTS | 87 |
| RESUME AND ACADEMIC ACHIEVEMENTS..... | 88 |

CHAPTER 1 INTRODUCTION

Superconductivity, discovered in 1911 by Heike Kamerlingh Onnes ^[1], is a macroscopic quantum phenomenon where certain materials exhibit zero electrical resistance and the complete repulsion of magnetic fields below a critical temperature (T_c). Due to the broad engineering applications of superconductors in areas such as superconducting cables, superconducting magnetic levitation, superconducting magnets for fusion reactors and superconducting quantum computing, research in this field has remained highly active for decades. Beyond these applications, superconductivity encompasses complex interactions between electrons, and is closely related to various exotic quantum states of matter. The underlying mechanisms of superconductivity have fascinated condensed matter physicists since its discovery, and remain an open question to this day. In particular, the high-temperature superconductivity mechanisms of unconventional superconductors, such as cuprates, lie at the heart of condensed matter physics. Solving this puzzle might lead to the discovery of superconductors with higher superconducting transition temperatures and, ultimately, to the achievement of room-temperature superconductivity.

This chapter provides a brief introduction to the history and basic concepts of superconductivity, followed by the research background of cuprate superconductors and the emerging nickelate superconductors. Significant emphasis is placed on the literature review of nickelate superconductors, which forms the basis of this thesis. Finally, the primary research work conducted in this thesis is introduced.

1.1 History of Superconductivity

Superconductivity was initially discovered in mercury, a material whose resistance displays a sharp jump to a vanishingly small value (less than $10^{-6} \Omega$) at a temperature as low as 4.2 K ^[1]. This breakthrough was enabled by the successful liquefaction of helium to reach such low temperatures. In addition to the zero-

resistance feature characteristic of superconductors (shown in Figure 1-1a), another fundamental property is perfect diamagnetism (shown in Figure 1-1b). Also known as the Meissner effect, it was discovered in 1933 by W. Meissner and R. Ochsenfeld ^[2]. When the material is cooled below the critical temperature T_c , the external magnetic field is completely excluded from the bulk. However, when the external magnetic field exceeds a critical value H_c , the superconducting state is destroyed, and the material returns to the normal state. The critical temperature T_c and critical magnetic field H_c are two key parameters used to evaluate the robustness of the superconducting state in a given material.

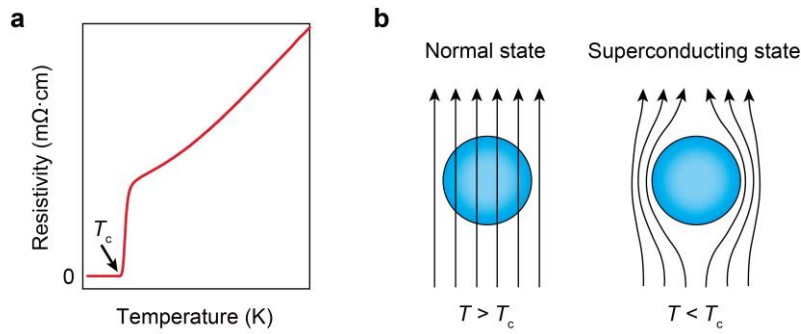


Figure 1-1 Basic properties of superconductors. (a) Representative temperature dependent resistivity curve of a superconductor. The arrow indicates the superconducting critical temperature T_c , below which zero resistance is reached. (b) Illustration of the Meissner effect. In the normal state ($T > T_c$), the magnetic field can penetrate through the material. When the material enters the superconducting state ($T < T_c$), the magnetic field is completely expelled from the interior.

In 1957, Bardeen, Cooper and Schrieffer proposed the first microscopic theory to explain superconductivity, known as the BCS theory ^[3]. The theory proposed that when an electron moves through a lattice, the resulting lattice distortion creates a region of enhanced positive charge density, which effectively attracts another electron with opposite momentum and spin. This phonon-mediated attractive interaction allows two electrons to pair up and form the so-called Cooper pair. As bosons, Cooper pairs can condense into a globally coherent quantum state, allowing them to travel through the lattice without energy dissipation, thereby giving rise to superconductivity.

According to BCS theory, the superconducting critical temperature T_c can be estimated as

$$k_B T_c = 1.14 \hbar \omega_D \exp \left[-\frac{1}{N(0)V} \right], \quad (1-1)$$

where k_B is the Boltzmann constant, ω_D is the Debye frequency, $N(0)$ is the density of states at the Fermi surface, and V is the electron–phonon coupling constant. It is clear that stronger electron–phonon coupling leads to a higher T_c . However, in conventional superconductors whose pairing relies on electron–phonon interaction, due to lattice instability at strong electron–phonon coupling, T_c is predicted to be limited to around 40 K, a threshold known as the McMillan limit [4].

A major breakthrough occurred in 1986, when Bednorz and Müller discovered superconductivity in the doped copper-based oxide $\text{La}_{2-x}\text{Ba}_x\text{CuO}_4$ system with a T_c of 35 K [5], as shown in Figure 1-2. This discovery sparked a revolution in the study of cuprate superconductors. Less than a year later, superconductivity with $T_c > 90$ K was reported in $\text{YBa}_2\text{Cu}_3\text{O}_{7-y}$ by Chu *et al.* [6] and Zhao *et al.* [7]. This high T_c , exceeding the boiling point of liquid nitrogen, significantly surpassed the McMillan limit set for conventional superconductors. Therefore, cuprate superconductors could no longer be adequately described by traditional BCS theory, and those that deviate from the BCS-scenario are termed unconventional superconductors. To date, a comprehensive understanding of the superconductivity mechanisms in unconventional superconductors remains elusive, and these puzzles remain to be answered.

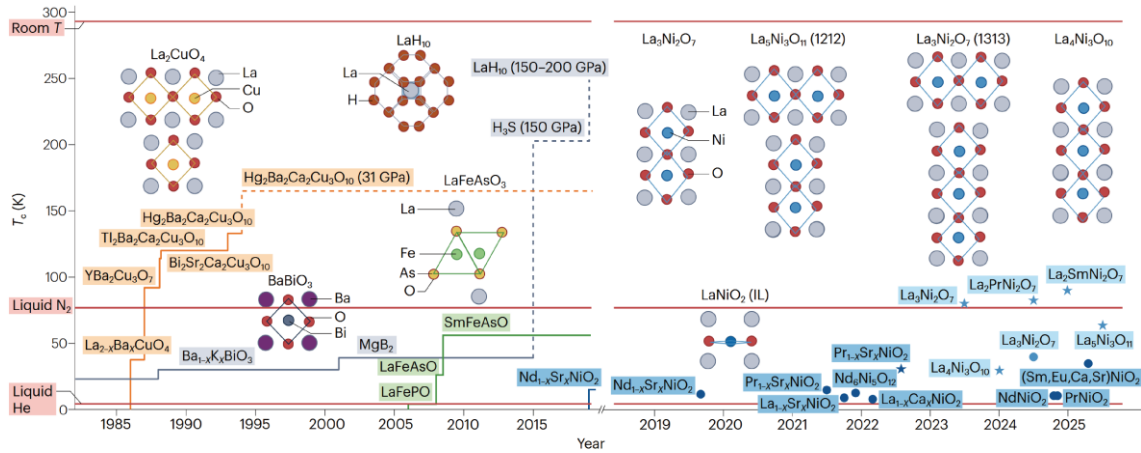


Figure 1-2 History of the discovery of various superconducting material families [8]. Three key unconventional superconductor families are denoted in different colors. Orange represents cuprates, green represents iron-based superconductors, and blue represents nickelates. Several conventional superconductors with relatively high T_c are shown in grey shaded rectangles.

Following the discovery of cuprate superconductors, several more unconventional superconductor families were identified. Heavy-fermion superconductivity was discovered by Steglich *et al.* in CeCu_2Si_2 in 1979 ^[9], and iron-based superconductors were discovered by Hosono *et al.* in $\text{LaFeAsO}_{1-x}\text{F}_x$ with $T_c = 26$ K in 2008 ^[10]. In that same year, the T_c of iron-based superconductors was quickly boosted to 43 K in $\text{SmFeAsO}_{1-x}\text{F}_x$, exceeding the McMillan limit ^[11]. In 2019, Hwang *et al.* discovered superconductivity in $\text{Nd}_{0.8}\text{Sr}_{0.2}\text{NiO}_2$ nickelate thin films by mimicking cuprates and designing an infinite-layer crystal structure ^[12]. Considering the structural similarity between cuprate and nickelate superconductors, studying nickelates is expected to help shed light on the superconductivity mechanisms in cuprates.

1.2 Cuprate Superconductors

Although various theories have been proposed to explain superconductivity in cuprates, no consensus has yet been reached. However, several fundamental aspects of cuprate superconductors are well understood.

Figure 1-3a shows the crystal structure of the parent compound La_2CuO_4 , from which superconductivity in the classical $\text{La}_{2-x}\text{Sr}_x\text{CuO}_4$ system emerges via chemical doping. This structure typifies the layered nature of cuprates, as illustrated in Figure 1-3b, where the CuO_2 planes, the primary sites for electron conduction, are separated by block-like charge reservoirs. These charge reservoirs modulate the carrier density within the CuO_2 planes but do not directly contribute to the electronic structure near the Fermi surface, resulting in the quasi-two-dimensional nature of cuprates ^[13].

In La_2CuO_4 , copper ions typically exhibit a nominal +2 charge and a $3d^9$ electron configuration. In an octahedral crystal field (Figure 1-3c), the surrounding oxygen ions create an electrostatic field that splits the copper $3d$ orbitals into t_{2g} and e_g manifolds. The e_g orbitals, which align with the oxygen $2p$ orbitals, experience stronger electrostatic repulsion due to direct overlap, raising their energy relative to the t_{2g} orbitals. Additionally, in cuprates, the apical oxygen ions (those above and below the CuO_2 plane) are either displaced farther away from the Cu^{2+} ions than the in-plane oxygen ions or, in some cases, completely absent

[14]. This Jahn–Teller-like lattice distortion further lifts the degeneracy of the e_g orbitals, pushing the $d_{x^2-y^2}$ orbital to the highest energy level. Consequently, the $d_{x^2-y^2}$ orbital is half-filled while the other orbitals are fully occupied, giving each copper ion a total spin of $S = 1/2$.

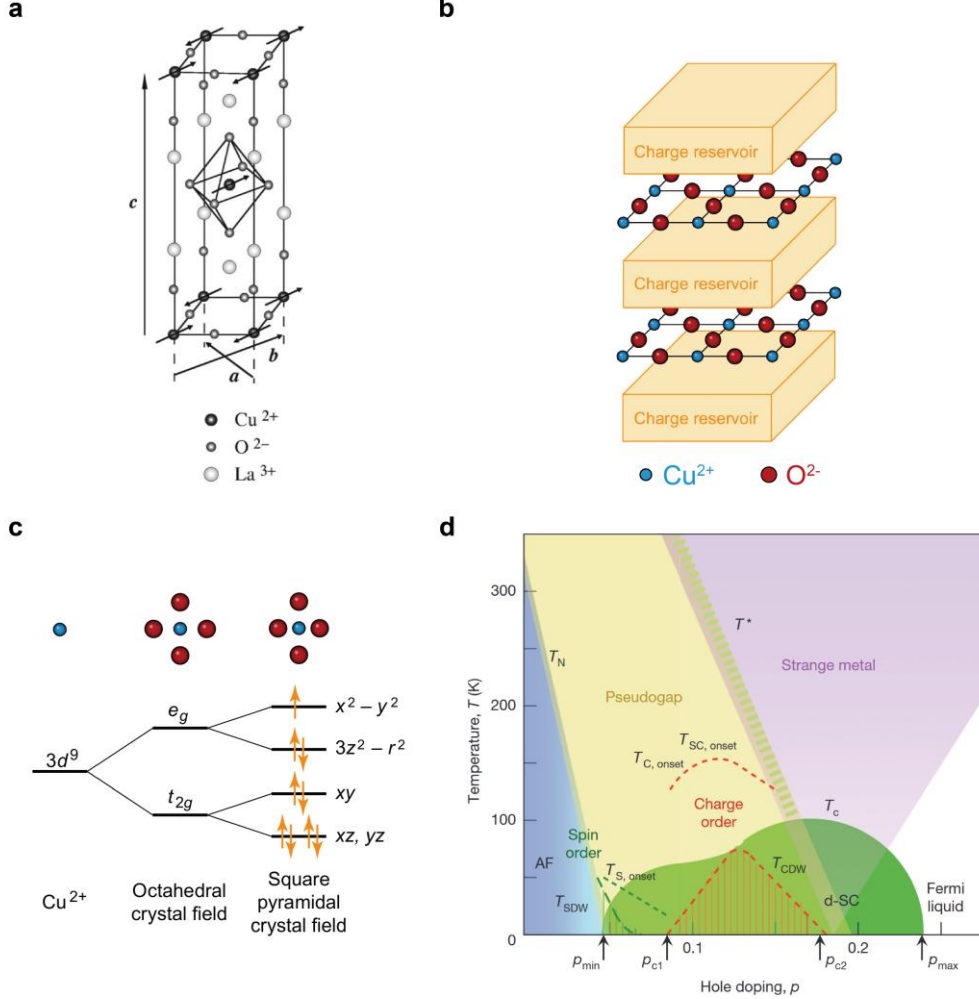


Figure 1-3 Crystal structure and phase diagram of canonical cuprates. (a) Crystal and magnetic structure of the parent compound La_2CuO_4 [15]. (b) Schematic of the layered structure of cuprates [14]. Blue and red spheres represent Cu^{2+} and O^{2-} ions, respectively. (c) Crystal field splitting of the Cu^{2+} $3d$ orbitals [14]. (d) Representative hole-doping phase diagram of cuprate superconductors [16]. The antiferromagnetic (AF) and d -wave superconducting (d-SC) phases are indicated by blue and green regions, respectively. The red striped area denotes the charge order region, while the pseudogap and strange metal regimes are shaded in yellow and purple, respectively.

A partially filled band is expected to be metallic according to conventional band theory, which neglects electron-electron interactions. However, strong electron correlation effects in cuprates introduce a large on-site Coulomb repulsion

(U). This splits the half-filled band into a fully occupied lower Hubbard band (LHB) and an empty upper Hubbard band (UHB), making the undoped parent compounds insulating ^[17]. Such materials are described by Mott physics and termed Mott insulators. Furthermore, the strong hybridization between copper $3d$ and oxygen $2p$ orbitals allows neighboring copper spins to interact via intervening oxygen atoms, leading to an antiferromagnetic (AFM) ground state ^[18]. Thus, the parent compounds are characterized as antiferromagnetic Mott insulators.

By doping the charge reservoirs (for example, replacing La^{3+} with Sr^{2+} for hole doping or with Ce^{4+} for electron doping), carriers are introduced into the CuO_2 planes ^[19]. These introduced holes primarily reside on the oxygen $2p$ orbitals ^[20], disrupting the long-range AFM order ^[21]. As the AFM order is suppressed, superconductivity emerges, as shown in the phase diagram in Figure 1-3d. The T_c exhibits a dome-shaped dependence on the hole doping level, reaching its maximum at an optimal doping point. Overdoping eventually quenches the superconductivity, leading to Fermi-liquid behavior. In addition to AFM and superconductivity, the cuprate phase diagram features a rich variety of quantum states, such as the pseudogap (where a gap exists in the normal state), strange metal behavior (characterized by linear-in-temperature resistivity), and charge/spin density waves (CDW/SDW). The intricate interplay between these states makes elucidating the mechanism of cuprate superconductivity both challenging and fascinating.

In summary, decades of study have established several key features of cuprates ^[22,23]: (1) a quasi-two-dimensional layered structure with CuO_2 planes as active layers; (2) a crystal field that favors large orbital polarization, placing the $3d_{x^2-y^2}$ orbital at the highest energy level; (3) a $3d^9$ electron configuration resulting in a total spin of $S = 1/2$; and (4) strong hybridization between oxygen $2p$ orbitals and copper $3d$ orbitals. These characteristics provide a blueprint for designing similar materials to uncover new classes of superconductors. Nickel, as the element adjacent to copper in the periodic table, has attracted significant attention.

1.3 Nickelate Superconductors

1.3.1 Ruddlesden–Popper and Square-Planar Nickelates

Nickelate superconductors, discovered in 2019 ^[12], have emerged as a promising playground for the intensive study of unconventional superconductivity. There are primarily two classes of nickelate superconductors. One is the Ruddlesden–Popper (RP) phases, whose crystal structures are shown in the upper panel of Figure 1-4. RP nickelates, with the chemical formula $R_{n+1}Ni_nO_{3n+1}$ or $(RNiO_3)_nRO$ (where R represents the rare-earth element), can be viewed as alternating stacks of n perovskite-like $RNiO_3$ layers and one rock-salt RO layer. As the number of layers n approaches infinity, the structure reduces back to the perovskite phase, $RNiO_3$. By varying n , the average $3d$ electron occupancy of nickel can be modulated from $3d^8$ (for $n = 1$) to $3d^7$ (for $n = \infty$).

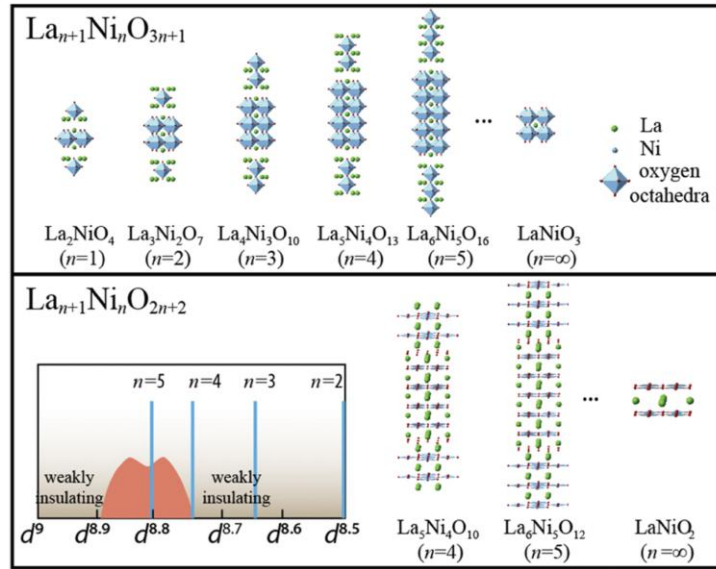


Figure 1-4 Crystal structures of La-based Ruddlesden–Popper nickelates $La_{n+1}Ni_nO_{3n+1}$ (upper panel) and square-planar nickelates $La_{n+1}Ni_nO_{2n+2}$ (lower panel) ^[24]. The inset in the lower panel depicts a typical superconducting phase diagram of infinite-layer nickelates. The $3d$ electron occupancy positions for several $La_{n+1}Ni_nO_{2n+2}$ phases are indicated by blue vertical lines.

The lower panel of Figure 1-4 shows the square-planar phases, another key class of nickelate superconductors, which are obtained through the chemical reduction of RP nickelates ^[12,25–27]. During the reduction process, the inner apical oxygen atoms are completely removed, while oxygen atoms in the $(RO)_2$ block

rearrange to form a fluorite-type slab. The resulting square-planar nickelates have a lower nickel valence state compared to their RP counterparts. By combining these two homologous series, the $3d$ electron occupancy of nickel can be tuned from $3d^7$ (in RNiO_3) to $3d^9$ (in RNiO_2), as summarized in Table 1-1.

Table 1-1 $3d$ electron occupancy of nickel in RP and square-planar phases

| Number of layers | RP phases | Square-planar phases |
|------------------|-------------|----------------------|
| $n = 1$ | $3d^8$ | |
| $n = 2$ | $3d^{7.5}$ | $3d^{8.5}$ |
| $n = 3$ | $3d^{7.33}$ | $3d^{8.67}$ |
| $n = 4$ | $3d^{7.25}$ | $3d^{8.75}$ |
| $n = 5$ | $3d^{7.2}$ | $3d^{8.8}$ |
| $n = \infty$ | $3d^7$ | $3d^9$ |

The crystal structure of these square-planar phases, where two-dimensional NiO_2 planes are separated by rare-earth blocks, is reminiscent of the quasi-two-dimensional layered structure of cuprate superconductors. Additionally, the $3d$ electron occupancy in square-planar nickelates is near $3d^9$, similar to the copper $3d$ configuration in the parent compounds of cuprate superconductors. A $(9 - 1/n)$ $3d$ occupancy effectively introduces the hole doping ^[25], while the replacement of rare-earth elements with alkaline-earth elements provides another means of hole doping ^[12,28–30], which is crucial for the emergence of superconductivity in cuprates. Given these structural and electronic similarities, square-planar nickelates hold great potential for hosting superconductivity.

1.3.2 Infinite-Layer Nickelate Superconductors

1.3.2.1 Doping-Dependent Superconducting Phase Diagram

The breakthrough in nickelate superconductivity occurred in 2019, when Li *et al.* discovered superconductivity in $\text{Nd}_{0.8}\text{Sr}_{0.2}\text{NiO}_2$ thin films ^[12]. This material is a chemical doped, infinite-layer square-planar nickelate, synthesized by reducing its perovskite precursor $\text{Nd}_{0.8}\text{Sr}_{0.2}\text{NiO}_3$ using CaH_2 as a reducing agent (Figure 1-5a). Similar to cuprates, superconductivity is induced through hole doping by substituting Nd^{3+} with Sr^{2+} , as shown in Figure 1-5b.

Despite the superficial structural and electronic similarities between infinite-layer nickelates and cuprates, such as the quasi-2D layered structure and the $3d^9$ configuration, a closer examination of their phase diagrams reveals several distinct differences. As shown in Figure 1-5c, nickelates exhibit a weakly insulating behavior at low doping levels ^[30], whereas cuprates feature an AFM Mott insulating phase in the underdoped region ^[31]. However, certain features, such as the linear-in-temperature resistivity near optimal doping, and Fermi liquid behavior in the overdoped region, are shared by both families ^[28].

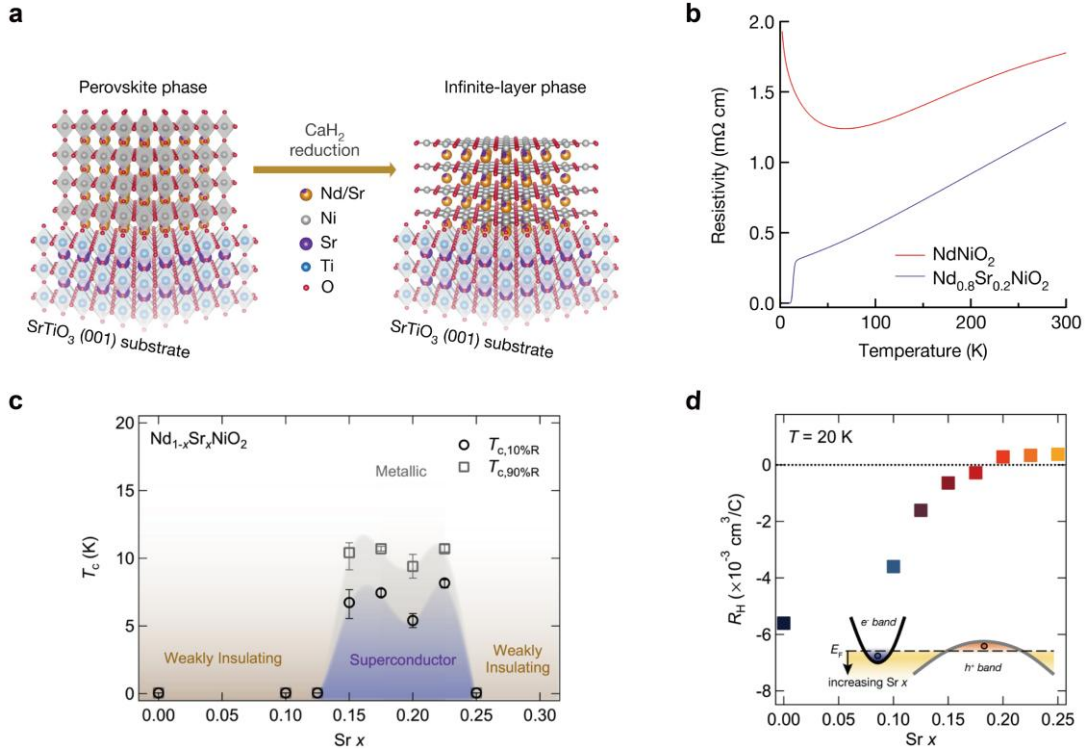


Figure 1-5 Superconductivity in infinite-layer nickelates. (a) Schematic of the topotactic reduction from the perovskite precursor $\text{Nd}_{0.8}\text{Sr}_{0.2}\text{NiO}_3$ thin films to the infinite-layer phase $\text{Nd}_{0.8}\text{Sr}_{0.2}\text{NiO}_2$ ^[12]. (b) Temperature-dependent resistivity (ρ - T) curves for the undoped parent compound NdNiO_2 and the Sr-doped $\text{Nd}_{0.8}\text{Sr}_{0.2}\text{NiO}_2$ ^[12]. (c) Doping-dependent superconducting phase diagram of $\text{Nd}_{1-x}\text{Sr}_x\text{NiO}_2$ ^[30]. (d) Doping dependence of the Hall coefficient R_H at a constant temperature of $T = 20 \text{ K}$ ^[30]. The inset illustrates the proposed two-band model for infinite-layer nickelate superconductors.

In terms of charge order and magnetism, charge density wave (CDW) order is absent in fully reduced NdNiO_2 ^[32], marking another departure from the cuprate phenomenology. Although long-range magnetic order is not observed in LaNiO_2 or NdNiO_2 ^[33,34], antiferromagnetic excitations have been detected in NdNiO_2 thin films using resonant inelastic x-ray scattering (RIXS), reported by

Lu *et al.* [35]. In addition, Fowlie *et al.* [36] reported intrinsic magnetism coexisting with superconductivity in a series of superconducting infinite-layer nickelates with various rare-earth ions, using muon spin rotation/relaxation (μ SR). This further underscores a distinction in magnetic behavior compared to cuprates.

The absence of long-range magnetic order in parent compound of infinite-layer nickelates might be attributed to the significantly reduced hybridization between O $2p$ and Ni $3d$ orbitals [37], in contrast to the strong p - d hybridization in cuprates [20]. Hepting *et al.* [38] utilized X-ray absorption spectroscopy (XAS) on undoped infinite-layer nickelates, and determined a relatively large charge-transfer energy Δ (the energy gap between the O $2p$ band and the Ni $3d$ upper Hubbard band). This supports a Mott-Hubbard description for infinite-layer nickelates, whereas cuprates are categorized as charge-transfer insulators [37,38].

Doping-dependent Hall transport (Figure 1-5d) also reveals difference from cuprates [30]. The Hall coefficient R_H is negative for the undoped sample, indicating electron-like charge carriers. As doping increases, the magnitude of R_H decreases, which suggests an increase in electron density within a simple single-band model. This observation seems to contradict the original goal of introducing holes by replacing Nd^{3+} with Sr^{2+} . However, at higher doping levels, R_H gradually transitions from negative to positive. This evolution supports a two-band model, where an electron-like band dominates the Fermi surface at low doping but is eventually depleted by further hole doping, allowing a hole-like band to dominate [30], as illustrated in the inset of Figure 1-5d.

In summary, the unique features of the nickelate phase diagram, including the absence of charge density wave order and long-range magnetic order, together with the multiband nature of infinite-layer nickelates suggest that the superconducting mechanism in nickelates may differ from that of cuprates [39].

1.3.2.2 Band Structure

Due to the strong electron correlation effects in unconventional superconductors such as nickelates, their electronic structures cannot be accurately predicted by first-principles calculations. Angle-resolved photoemission spectroscopy (ARPES) is therefore employed to determine the actual band structure,

providing a foundation upon which reasonable theoretical models can be developed. Figure 1-6 summarizes the ARPES results on infinite-layer nickelates.

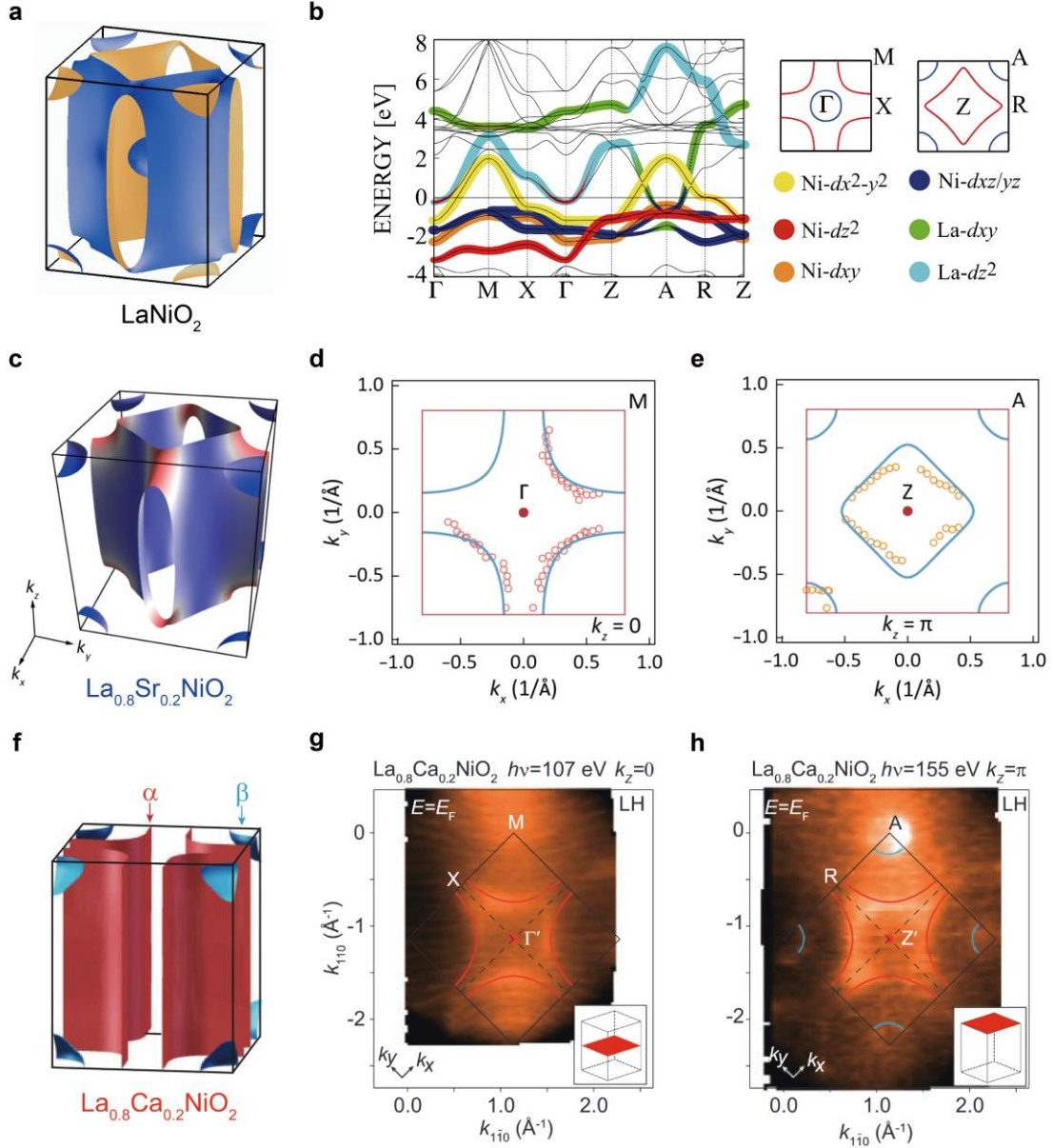


Figure 1-6 Electronic band structure and Fermi surfaces of infinite-layer nickelates. (a) First-principles calculated three-dimensional (3D) Fermi surface of LaNiO_2 [40]. (b) Energy dispersion along high-symmetry directions, and Fermi surfaces at $k_z = 0$ (top right-hand panel, left) and $k_z = \pi$ (top right-hand panel, right) [40]. Orbital contributions are highlighted with different colors. The Ni-derived and La-derived Fermi surfaces are indicated by red and blue lines, respectively. (c) DFT-calculated 3D Fermi surface of $\text{La}_{0.8}\text{Sr}_{0.2}\text{NiO}_2$ [41]. (d, e) DFT-calculated Fermi surface maps (solid lines) at $k_z = 0$ (d) and $k_z = \pi$ (e) [41]. Open circles represent Fermi momenta extracted from ARPES measurements. (f) Sketch of the 3D Fermi surface of $\text{La}_{0.8}\text{Ca}_{0.2}\text{NiO}_2$ based on ARPES data [42]. (g, h) Fermi surface maps of $\text{La}_{0.8}\text{Ca}_{0.2}\text{NiO}_2$ measured by ARPES at $k_z = 0$ (g) and $k_z = \pi$ (h), obtained using linear horizontal (LH) photon polarization [42].

Figures 1-6a and 1-6b show the first-principles calculated band structure of LaNiO_2 ^[40]. The Fermi surface consists of a dominant sheet derived from the Ni $d_{x^2-y^2}$ orbitals, which exhibits a k_z dispersion evolving from hole-like at $k_z = 0$ to electron-like at $k_z = \pi$. In addition, it features a 3D electron pocket at the Brillouin zone corner and another electron pocket at the Γ point. These two small electron pockets are characterized by La $5d$ orbitals ^[40]. Sun *et al.* ^[41] reported ARPES results for $\text{La}_{0.8}\text{Sr}_{0.2}\text{NiO}_2$ (Figures 1-6c to 1-6e), which largely agree with the first-principles calculations, except that the predicted electron pocket at the Γ point is not observed. Furthermore, the electron pocket at the A point exhibits negligible band renormalization, in contrast to the mass enhancement of 2 to 3 observed in the Ni $d_{x^2-y^2}$ -derived band. This suggests that the A pocket experiences weak electron correlation and contributes to self-doping within the system ^[41].

However, ARPES results on $\text{La}_{0.8}\text{Ca}_{0.2}\text{NiO}_2$ reported by Ding *et al.* ^[42] (Figures 1-6f to 1-6h) reveal certain discrepancies. The Ni $d_{x^2-y^2}$ -derived α band shows a quasi-2D feature with no discernible k_z dependence. Notably, the absence of electron pockets at the Γ point in both LaNiO_2 and $\text{La}_{0.8}\text{Ca}_{0.2}\text{NiO}_2$ samples is consistent with the results for $\text{La}_{0.8}\text{Sr}_{0.2}\text{NiO}_2$. Additionally, both ARPES studies observed waterfall-like dispersions at high binding energies within the Ni $d_{x^2-y^2}$ -derived α band. Regarding the orbital character of the β band at the A point, ARPES results on NdNiO_2 reported by Li *et al.* ^[43] suggest that interstitial s orbitals contribute significantly to this electron pocket, while rare-earth $5d$ electrons play a minor role at the Fermi surface.

Despite these discrepancies between various experimental reports and theoretical predictions, which necessitate rigorous and comprehensive investigation, the multi-band nature of infinite-layer nickelates arising from additional electron pockets clearly distinguishes them from cuprates, whose Fermi surfaces are dominated by $d_{x^2-y^2}$ orbitals. This distinction underscores the unique nature of superconductivity in the infinite-layer nickelate family.

1.3.2.3 Infinite-Layer Nickelate Family

Further evidence supporting the self-doping effect from the electron pockets in the infinite-layer nickelates is the observation of superconductivity in the undoped parent compounds, as shown in Figure 1-7a. This phenomenon appears to

be intrinsic, as superconductivity has been achieved in LaNiO_2 [44], NdNiO_2 [45] and PrNiO_2 [46] by improving sample quality. How these observations can be reconciled with the established phase diagram remains an intriguing question.

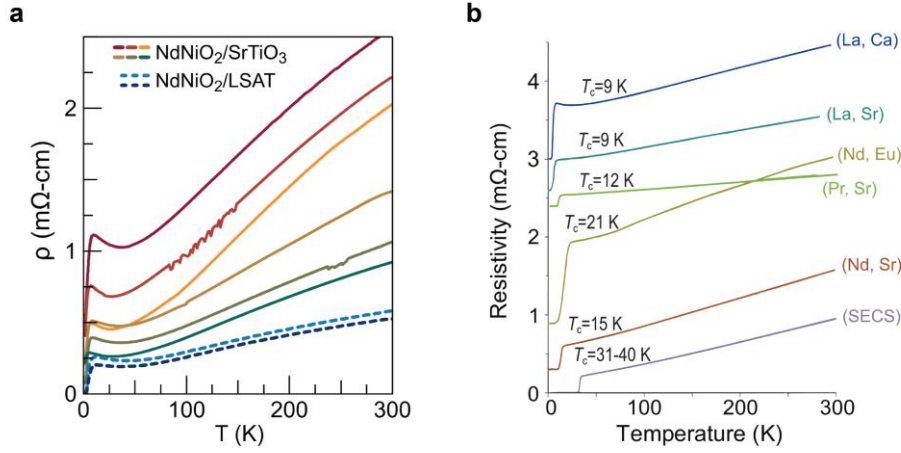


Figure 1-7 ρ - T curves of various infinite-layer nickelates. (a) ρ - T curves for undoped NdNiO_2 [45]. Solid and dashed lines represent NdNiO_2 films grown on SrTiO_3 and LSAT substrates, respectively. (b) Representative ρ - T curves of a series of infinite-layer nickelates with diverse rare-earth and dopant elements [47].

Following the discovery of superconductivity in $\text{Nd}_{1-x}\text{Sr}_x\text{NiO}_2$, the infinite-layer family has expanded to include various rare-earth and dopant elements. Superconductivity has been demonstrated in $\text{La}_{1-x}\text{Sr}_x\text{NiO}_2$ [44], $\text{La}_{1-x}\text{Ca}_x\text{NiO}_2$ [48], $\text{Pr}_{1-x}\text{Sr}_x\text{NiO}_2$ [49], $\text{Nd}_{1-x}\text{Eu}_x\text{NiO}_2$ [50] and $\text{Sm}_{1-x-y-z}\text{Eu}_x\text{Ca}_y\text{Sr}_z\text{NiO}_2$ (SECS) [47], as summarized in Figure 1-7b. Notably, the SECS nickelates reported by Chow *et al.* [47] have pushed the T_c of infinite-layer nickelates to nearly 40 K. Additionally, applying a high pressure of 12.1 GPa can raise the T_c of $\text{Pr}_{0.82}\text{Sr}_{0.18}\text{NiO}_2$ thin films from $\sim 17\text{ K}$ at ambient pressure to $\sim 31\text{ K}$ without signs of saturation, as reported by Wang *et al.* [51]. This pressure-induced T_c enhancement is partially attributed to c-axis shrinkage and the resulting strengthened hybridization between Ni $3d$ and Pr $5d$ orbitals.

The T_c enhancement induced by chemical substitution (using smaller Sm^{3+} or dopants like $\text{Ca}^{2+}/\text{Eu}^{2+/3+}$) or by external pressure may provide important insights into the superconducting mechanism of infinite-layer nickelates. Further studies are essential to identify the key ingredients responsible for this enhanced superconducting performance.

1.3.3 Bilayer Ruddlesden–Popper Nickelate Superconductors

1.3.3.1 Pressure-Dependent Superconducting Phase Diagram

In 2023, superconductivity with an onset temperature near 80 K was reported in the bilayer Ruddlesden–Popper (RP) nickelate, $\text{La}_3\text{Ni}_2\text{O}_7$, under high pressure (above 14 GPa) in single-crystal bulk samples, by Wang *et al.* [52]. This T_c not only exceeds the McMillan limit of 40 K, but also surpasses the boiling point of liquid nitrogen (77 K), suggesting an unconventional superconducting mechanism underlying this system. Theoretical calculations indicate that electron–phonon coupling alone cannot account for such a high T_c [53]. Instead, magnetic fluctuations are thought to play a crucial role in the pairing mechanism [54]. Notably, $\text{La}_3\text{Ni}_2\text{O}_7$ deviates significantly from the traditional $3d^9$ paradigm of cuprates or infinite-layer nickelates, as the nominal Ni valence state in $\text{La}_3\text{Ni}_2\text{O}_7$ is +2.5, corresponding to a $3d^{7.5}$ electron configuration.

Structurally, the major distinction between $\text{La}_3\text{Ni}_2\text{O}_7$ and infinite-layer square-planar nickelates is the presence of inner apical oxygen atoms between two adjacent NiO_2 planes. The interlayer coupling of Ni d_{z^2} orbitals through these inner apical oxygens splits the d_{z^2} states into a bonding state (lying below the Fermi level), and an antibonding state (lying above it) [52], as shown in Figure 1-8a. This d_{z^2} bonding band is designated as the γ band, and its role in the superconducting mechanism of bilayer RP nickelate is currently a subject of intense debate. In addition to strong interlayer coupling, the Jahn–Teller distortion in $\text{La}_3\text{Ni}_2\text{O}_7$ raises the $d_{x^2-y^2}$ orbital above the d_{z^2} orbital in energy. The overall electronic picture for each nickel ion consists of a fully occupied d_{z^2} bonding γ band and a quarter-filled $d_{x^2-y^2}$ orbital.

Although the nominal $3d^{7.5}$ configuration appears to deviate from the conventional $3d^9$ scenario, the antibonding state resulting from interlayer coupling remains unoccupied above the Fermi level. Consequently, the $\text{Ni}^{2.5+}$ configuration in $\text{La}_3\text{Ni}_2\text{O}_7$ also features fully occupied lower $3d$ orbitals with the exception of the partially occupied $d_{x^2-y^2}$ orbital at the highest energy level. In this sense, the electronic environment partially resembles that of Cu^{2+} in cuprates.

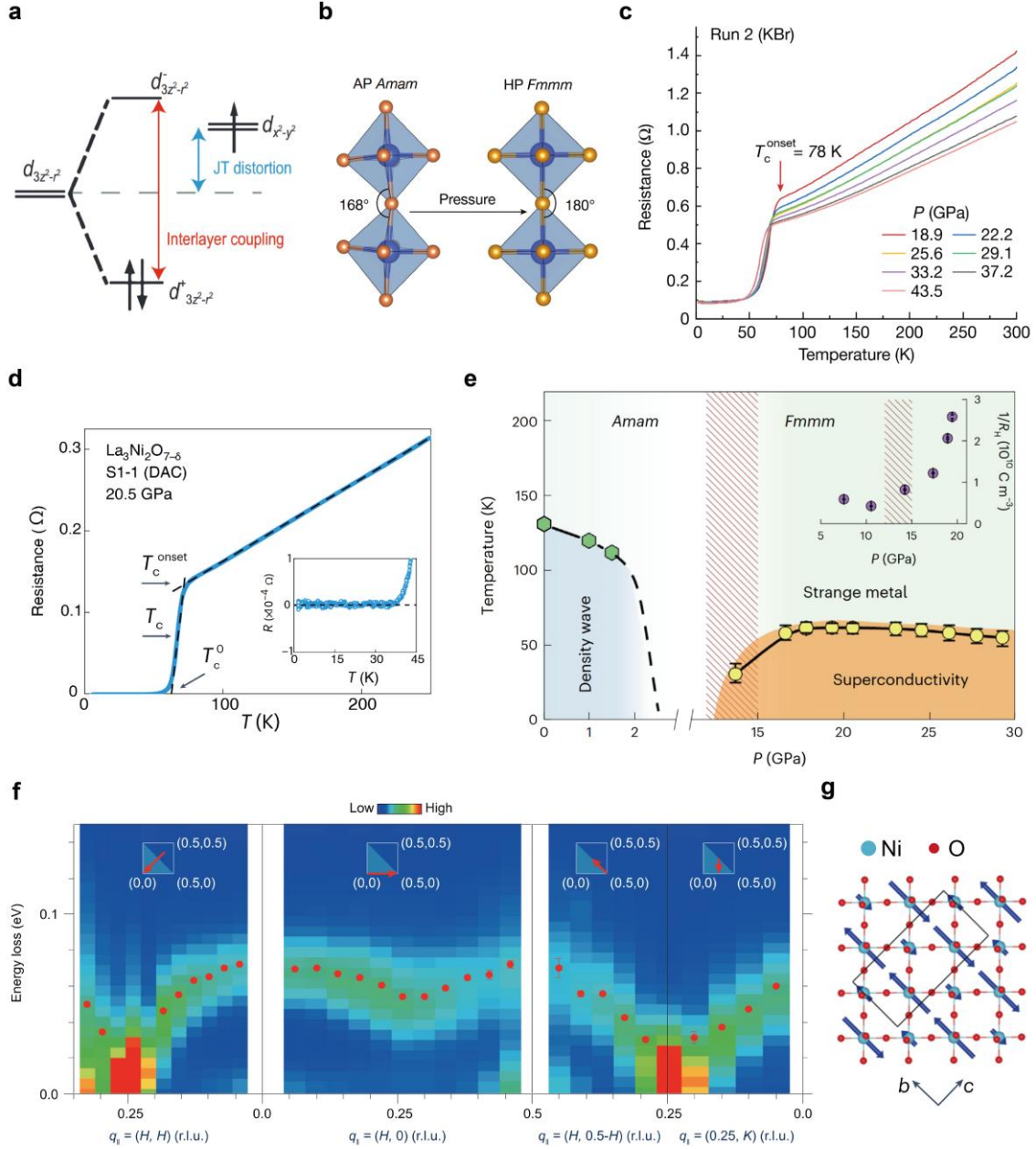


Figure 1-8 High-temperature superconductivity in $\text{La}_3\text{Ni}_2\text{O}_7$. (a) Electronic configuration of two $\text{Ni}^{2.5+}$ ions [55]. (b) Structural transition of $\text{La}_3\text{Ni}_2\text{O}_7$ from the $Amam$ to the $Fmmm$ space group under pressure [52]. (c) Pressure-dependent ρ - T curves of $\text{La}_3\text{Ni}_2\text{O}_7$ using KBr as the pressure-transmitting medium [52]. The arrow indicates the superconducting onset temperature at 18.9 GPa. (d) ρ - T curve of $\text{La}_3\text{Ni}_2\text{O}_7$ at 20.5 GPa obtained using a diamond anvil cell (DAC) [56]. The inset provides an enlarged view of the region approaching zero resistance. (e) Pressure-dependent phase diagram of $\text{La}_3\text{Ni}_2\text{O}_7$ [56]. Green hexagons and yellow circles denote the density wave and superconducting transition temperatures, respectively. The striped area represents the structural phase transition region. The inset shows the pressure-dependent reciprocal Hall coefficient ($1/R_H$) at 80 K. (f) RIXS intensity maps of $\text{La}_3\text{Ni}_2\text{O}_7$ along high-symmetry directions at 20 K and ambient pressure [57]. (g) A proposed magnetic structure of $\text{La}_3\text{Ni}_2\text{O}_7$ at ambient pressure [8]. Blue and red spheres represent Ni and O atoms, respectively. The image shows a top view projected onto the NiO_2 planes.

At ambient pressure, the NiO_6 octahedra in $\text{La}_3\text{Ni}_2\text{O}_7$ are tilted relative to the c -axis, resulting in a Ni–O–Ni bond angle of 168° and buckled NiO_2 planes. Under pressure, $\text{La}_3\text{Ni}_2\text{O}_7$ undergoes a structural phase transition from the orthorhombic $Amam$ space group to the $Fmmm$ space group ^[52] (though subsequent studies suggest the superconducting phase adopts the tetragonal $I4/mmm$ symmetry ^[58]). The most significant structural change is the straightening of the Ni–O–Ni bond, where the bond angle increases from 168° to 180° , as illustrated in Figure 1-8b. This increased structural symmetry, accompanied by the shrinkage of the unit cell volume, is thought to enhance the interlayer antiferromagnetic exchange interactions ^[54]. Concomitant with this structural transition, high-temperature superconductivity emerges, as shown in Figure 1-8e.

Figure 1-8c shows the pressure-dependent ρ – T curves from the initial discovery of superconductivity in $\text{La}_3\text{Ni}_2\text{O}_7$ ^[52]. The maximum onset T_c of 78 K was observed around 19 GPa. However, further increasing the pressure led to a decline in T_c , indicating that the T_c enhancement reaches a plateau. Notably, in early reports, the resistance dropped to a small finite value rather than reaching true zero resistance. By improving sample quality, Zhang *et al.* ^[56] achieved zero resistance near 40 K, as shown in Figure 1-8d. This improvement is also reflected in the significantly reduced normal-state resistivity. Furthermore, the resistance exhibits a linear-in-temperature behavior above onset T_c that extends up to 300 K, implying that a strange metal phase resides above the superconducting dome.

Wang *et al.* ^[59] reported bulk superconductivity in the Pr-substituted bilayer RP nickelate, $\text{La}_2\text{PrNi}_2\text{O}_7$. The partial substitution of Pr is proposed to suppress the intergrowth of other RP phases (such as $n = 1$ or $n = 3$ members), thereby ensuring a high-purity bilayer phase. Bulk superconductivity was confirmed by a noticeable diamagnetic response, with the superconducting shielding volume fraction estimated to exceed 90% at approximately 19 GPa. This work provides definite evidence that the bilayer RP phase is intrinsically responsible for high-temperature superconductivity.

The current T_c record is held by Sm-substituted $\text{La}_2\text{SmNi}_2\text{O}_7$, which exhibits a maximum $T_{c,\text{onset}}$ of 92 K and a $T_{c,\text{zero}}$ of 73 K at 21.6 GPa, reported by Li *et al.* ^[60]. Interestingly, T_c records in both the infinite-layer and bilayer RP families involve Sm-based compounds, suggesting a potential “Sm-effect” that warrants

further investigations to uncover the underlying mechanism of T_c enhancement.

In addition to efforts aimed at improving sample quality and enhancing T_c through chemical doping or optimized single-crystal growth, the density-wave phase that precedes superconductivity in the $\text{La}_3\text{Ni}_2\text{O}_7$ phase diagram has attracted significant attention. It has been intensively studied using various experimental techniques, including RIXS ^[57], μSR ^[61,62], resonant soft X-ray scattering (RSXS) ^[63], and nuclear magnetic resonance (NMR) ^[64]. The ρ - T curves of $\text{La}_3\text{Ni}_2\text{O}_7$ exhibit a distinct transport anomaly around 130–140 K at ambient pressure, which is attributed to a density-wave transition ^[56,62]. NMR measurements reported by Kakoi *et al.* ^[64] confirmed this density-wave transition below 150 K, and subsequent μSR experiments identified a spin-density-wave (SDW) transition at $T_{\text{SDW}} \sim 150$ K ^[61]. Furthermore, Khasanov *et al.* ^[62] reported that T_{SDW} increases with pressure up to approximately 2 GPa, indicating a strengthening of the magnetic order. This contrasts with the pressure dependence of the density-wave transition temperature (T_{DW}) observed in transport measurements, which decreases with pressure. This discrepancy has led to the hypothesis that the density wave in $\text{La}_3\text{Ni}_2\text{O}_7$ features the coexistence of an SDW and a charge-density-wave (CDW), the latter of which is likely responsible for the transport anomalies ^[55]. Optical conductivity measurements reported by Liu *et al.* ^[65] support the existence of this CDW, showing an energy gap opened below 115 K.

RIXS measurements reported by Chen *et al.* ^[57] reveal dispersive magnetic excitations in $\text{La}_3\text{Ni}_2\text{O}_7$, as shown in Figure 1-8f. The dispersion softens toward zero energy at the wave vector (0.25, 0.25), implying the formation of an SDW order with this propagation vector. A possible magnetic structure has been proposed (Figure 1-8g), where stripes with alternating low and high magnetic moments run along the diagonal direction of the NiO_2 planes, and are stacked antiferromagnetically along the c -axis ^[8]. However, no consensus has yet been reached regarding the exact magnetic structure of $\text{La}_3\text{Ni}_2\text{O}_7$ largely due to sample inhomogeneity ^[8,55]. The quality of $\text{La}_3\text{Ni}_2\text{O}_7$ crystals, which are particularly susceptible to the intergrowth of other RP phases and oxygen off-stoichiometry, must be further improved to facilitate more rigorous studies.

In summary, the emergence of a strange metal phase, CDW and SDW within

the superconducting phase diagram of $\text{La}_3\text{Ni}_2\text{O}_7$ is reminiscent of the phenomenology observed in cuprates. Exploring the mechanisms underlying superconductivity in $\text{La}_3\text{Ni}_2\text{O}_7$ and comparing them with cuprates may unveil universal ingredients required for high-temperature superconductivity.

1.3.3.2 Sensitivity to Oxygen Off-Stoichiometry

The stoichiometric formula $\text{La}_3\text{Ni}_2\text{O}_7$ frequently used for the bilayer RP nickelate is somewhat imprecise, as this material is highly susceptible to oxygen loss. Instead, $\text{La}_3\text{Ni}_2\text{O}_{7-\delta}$ provides a more accurate representation by accounting for potential oxygen vacancies. The resistivity of $\text{La}_3\text{Ni}_2\text{O}_{7-\delta}$ is highly sensitive to the oxygen deficiency level δ . Its transport can evolve from metallic behavior in the fully oxidized state ($\delta \approx 0$), to weakly insulating at low temperatures with minimal oxygen vacancies ($\delta = 0.08$), and finally to a completely insulating state as δ exceeds 0.16 [66]. Furthermore, insulating samples with a detrimental concentration of oxygen vacancies show no signature of superconductivity under pressure [52], underscoring the critical importance of maintaining proper oxygen stoichiometry.

There are several distinct oxygen sites in $\text{La}_3\text{Ni}_2\text{O}_{7-\delta}$, as illustrated in Figure 1-9a. The oxygen atoms within the NiO_2 planes are referred to as planar oxygens. Those positioned between two adjacent NiO_2 planes are termed inner apical oxygens, while those located between the bilayer blocks are outer apical oxygens. Furthermore, in Pr-substituted $\text{La}_2\text{PrNi}_2\text{O}_{7+\delta}$ samples, Dong *et al.* [67] reported the direct visualization of interstitial oxygen atoms using multislice electron ptychography (MEP) (Figures 1-9b and 1-9c). The partial substitution of Pr^{3+} , which has a smaller ionic radius relative to La^{3+} , expands the interstitial spaces between the bilayers, making them prone to accommodating excess oxygen during high-pressure oxygen annealing. These interstitial oxygens can form ordered structures with various periodicities, which negatively impact superconductivity. Although the over-oxidized $\text{La}_2\text{PrNi}_2\text{O}_{7+\delta}$ samples exhibit lower resistivity and more metallic behavior compared to as-grown samples, superconductivity is absent even under high pressure. This interstitial oxygen order is proposed to suppress superconductivity by altering the hole doping level and enhancing density-

wave correlations. Nevertheless, the combination of Pr substitution and appropriate annealing facilitates the achievement of near-stoichiometric oxygen content, thereby enhancing the superconducting performance of $\text{La}_2\text{PrNi}_2\text{O}_7$.

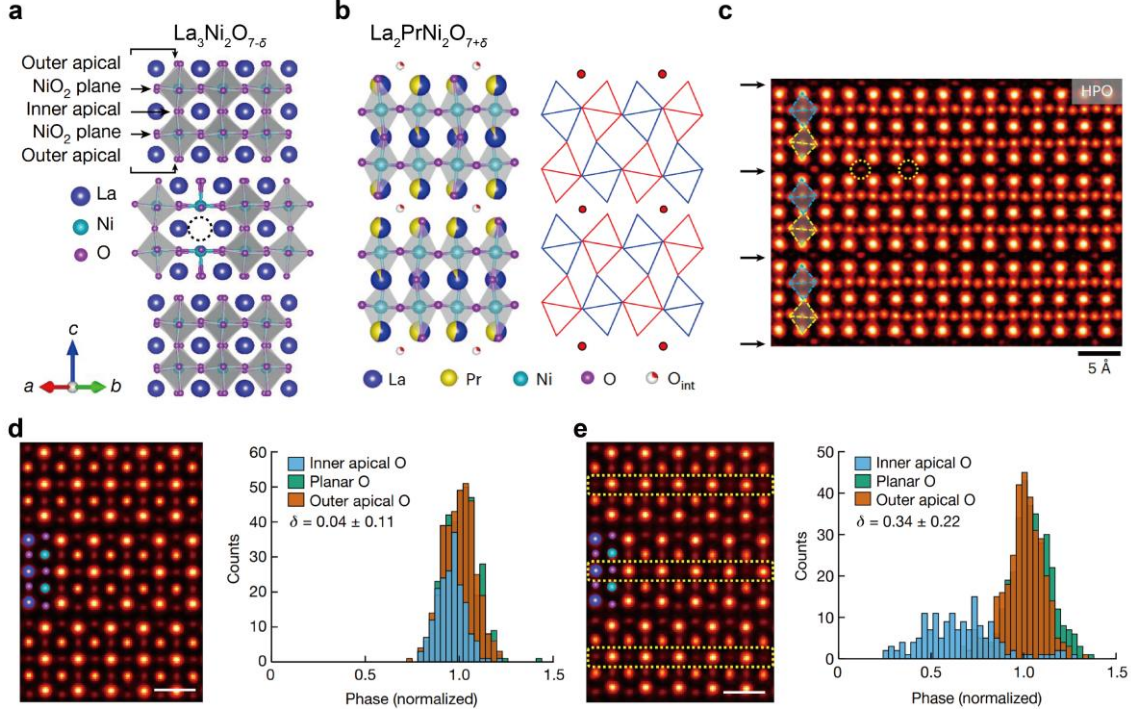


Figure 1-9 Sensitivity of $\text{La}_3\text{Ni}_2\text{O}_7$ to oxygen off-stoichiometry. (a) Crystal structure of $\text{La}_3\text{Ni}_2\text{O}_{7-\delta}$, indicating various oxygen sites [68]. The dashed circle denotes an inner apical oxygen vacancy. (b) Crystal structure (left) and NiO_6 octahedral tilt pattern (right) of $\text{La}_2\text{PrNi}_2\text{O}_{7+\delta}$ [67]. Interstitial oxygen atoms are represented by white spheres with red shading (left) and red circles (right). (c) Projected MEP phase image of a representative region in $\text{La}_2\text{PrNi}_2\text{O}_{7+\delta}$ [67]. Black arrows indicate interstitial layers and yellow dashed circles mark two interstitial oxygens atoms. “HPO” denotes high-pressure oxygen annealing. (d) Projected MEP phase image of a selected region in $\text{La}_3\text{Ni}_2\text{O}_{7-\delta}$ (left) and the corresponding phase-count histogram for three oxygen sites (right) [68]. Scale bar: 5 Å. (e) Projected MEP phase image (left) and histogram (right) of a region with higher oxygen vacancy concentration [68]. Yellow dashed rectangles highlight prominent inner apical oxygen vacancies.

Dong *et al.* [68] also investigated the non-uniform distribution of oxygen vacancies among different sites in $\text{La}_3\text{Ni}_2\text{O}_{7-\delta}$ using the MEP technique, which provides quantitative mapping of light atoms such as oxygen (Figures 1-9d and 1-9e). The intensity of the MEP phase can be used to identify and quantify vacancy sites, which exhibit attenuated phase intensity, as illustrated by the regions enclosed by yellow dashed rectangles Figure 1-9e. By analyzing the phase-count histograms for the three oxygen sites (planar, inner apical and outer apical) across

different regions, the oxygen deficiency δ was estimated to be 0.04 in one area and 0.34 in another. Notably, the oxygen vacancies reside predominantly in the inner apical sites, as shown in the right panel of Figure 1-9e. Since oxygens at these sites act as bridges between adjacent NiO_2 planes and contribute to strong interlayer coupling, their depletion is considered detrimental to superconductivity^[69]. Furthermore, oxygen K-edge electron energy loss spectroscopy (EELS) of the region with fewer oxygen vacancies ($\delta \approx 0.04$) revealed a prominent pre-peak at approximately 528 eV, which signifies strong p - d hybridization. Conversely, this pre-peak intensity was significantly suppressed in the region with a higher vacancy concentration ($\delta \approx 0.34$), indicating reduced p - d hybridization. This reduction in hybridization is likely a reason for the suppressed superconductivity in oxygen-deficient $\text{La}_3\text{Ni}_2\text{O}_{7-\delta}$ samples.

In summary, these two pivotal works leveraging the MEP technique highlight the complex variability of oxygen content in bilayer RP nickelates. The necessity of optimized oxygen stoichiometry for achieving superior superconducting performance imposes stringent requirements on sample synthesis.

1.3.3.3 Band Structure

Figures 1-10a and 1-10b present the ARPES results for $\text{La}_3\text{Ni}_2\text{O}_7$ at ambient pressure, as reported by Yang *et al.*^[70]. The Fermi surface consists of an electron-like pocket centered at the Brillouin zone (BZ) center, denoted as the α band, and a large hole-like β band. Both bands exhibit Ni $d_{x^2-y^2}$ character, as confirmed by polarization-dependent measurements. Furthermore, a Ni d_{z^2} -derived γ band, originating from d_{z^2} bonding states, is observed approximately 50 meV below the Fermi level near the BZ corner (Figure 1-10b). This γ band is remarkably flat and exhibits significantly stronger band renormalization compared to the α and β bands, indicating enhanced electron correlations within the γ band.

Moreover, DFT calculations suggest that the most significant evolution of the electronic structure under pressure is the upward shift of this γ band to cross the Fermi level, as shown in Figure 1-10c^[52]. The presence of this d_{z^2} -derived γ band at the Fermi surface under high pressure is considered a critical factor in the emergence of superconductivity^[52,69,71-73]. The two-component theory proposed by Yang *et al.*^[71], emphasizes the importance of the γ band, positing that

localized d_{z^2} electrons form Cooper pairs through strong interlayer superexchange interactions mediated by the inner apical oxygen. Subsequently, global phase coherence is achieved via the hybridization of d_{z^2} orbitals with itinerant $d_{x^2-y^2}$ electrons, thereby inducing high-temperature superconductivity.

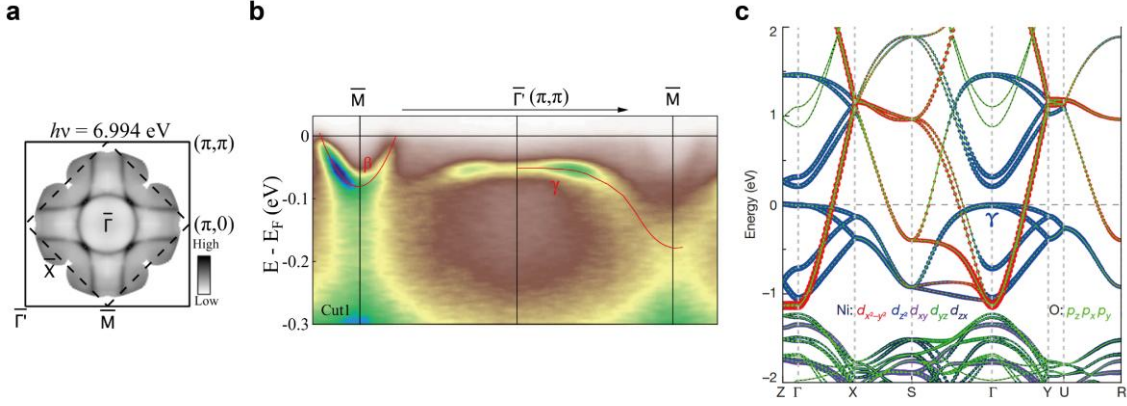


Figure 1-10 Electronic band structure of $\text{La}_3\text{Ni}_2\text{O}_7$. (a) Fermi surface map of $\text{La}_3\text{Ni}_2\text{O}_7$ measured by laser-ARPES at 18 K [70]. (b) Spectral cut along a high-symmetry direction [70]. Red solid lines indicate the dispersions of the β and γ bands. (c) DFT-calculated band structure of $\text{La}_3\text{Ni}_2\text{O}_7$ at 29.5 GPa [52]. Orbital characters of the bands are highlighted with different colors.

However, the exact role of the γ band in $\text{La}_3\text{Ni}_2\text{O}_7$ remains a subject of intense debate [8,54,55]. Due to the extreme high-pressure conditions required for superconductivity in bilayer RP nickelate, ARPES cannot be directly utilized to probe the electronic structure in the superconducting state. Therefore, achieving superconductivity at ambient pressure is imperative to elucidate the vital electronic ingredients responsible for high- T_c superconductivity. Such a breakthrough is necessary to establish definitive theoretical models, and to further explore the underlying superconducting mechanisms.

1.3.4 Other Nickelate Superconductors

1.3.4.1 Trilayer Ruddlesden–Popper Nickelate Superconductors

Following the discovery of pressured-induced high temperature superconductivity in $\text{La}_3\text{Ni}_2\text{O}_7$, the trilayer RP nickelate $\text{La}_4\text{Ni}_3\text{O}_{10}$ was also found to exhibit superconductivity under high pressure, as reported by Zhu *et al.* [74]. Figure 1-11 presents the pressure-dependent phase diagram of $\text{La}_4\text{Ni}_3\text{O}_{10}$. At ambient pressure, the transport behavior of $\text{La}_4\text{Ni}_3\text{O}_{10}$ shows a more prominent anomaly

near 135 K compared to $\text{La}_3\text{Ni}_2\text{O}_7$, indicating a density-wave transition. This is consistent with the intertwined CDW and SDW orders in $\text{La}_4\text{Ni}_3\text{O}_{10}$ revealed by synchrotron X-ray diffraction [75], neutron diffraction [75] and nuclear quadrupole resonance (NQR) [76]. Upon applying pressure, both the SDW and CDW are suppressed and abruptly disappear during a structural transition from the monoclinic $P2_1/a$ space group to tetragonal $I4/mmm$ symmetry [77]. Similar to the bilayer system, this structural transition involves the straightening of the Ni–O–Ni bond angle from 165.6° to 180° .

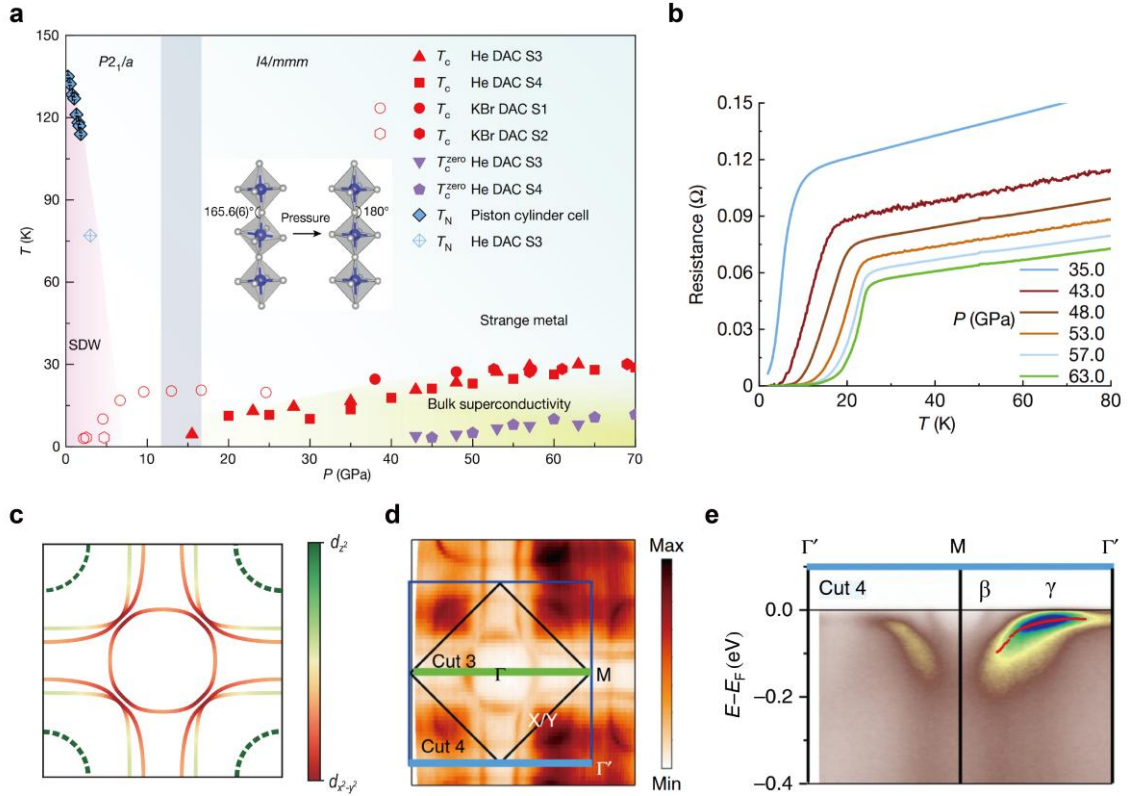


Figure 1-11 Pressure-induced superconductivity and electronic structure of $\text{La}_4\text{Ni}_3\text{O}_{10}$. (a) Pressure-dependent phase diagram of $\text{La}_4\text{Ni}_3\text{O}_{10}$ [74]. The shaded area represents the structural phase transition region, with the inset illustrating the structural evolution under pressure. (b) ρ – T curves of $\text{La}_4\text{Ni}_3\text{O}_{10}$ under pressures ranging from 35.0 GPa to 63.0 GPa [74]. (c) Calculated Fermi surface of $\text{La}_4\text{Ni}_3\text{O}_{10}$, with orbital characters indicated by color [55]. (d) ARPES-measured Fermi surface map of $\text{La}_4\text{Ni}_3\text{O}_{10}$ [78]. (e) ARPES spectral cut along the direction indicated by the blue line in (d), measured at 30 K [78]. Red dots, representing fitted peak positions from energy distribution curves (EDCs), trace the dispersion of the γ band.

Superconductivity gradually emerges following the suppression of the density wave and the structural transition. However, unlike $\text{La}_3\text{Ni}_2\text{O}_7$ where T_c saturates and subsequently declines with increasing pressure [52,56], the maximum T_c

of $\text{La}_4\text{Ni}_3\text{O}_{10}$ reaches approximately 30 K at the highest exerted pressure of 69.0 GPa (Figure 1-11b). Notably, the significant reduction in T_c for $\text{La}_4\text{Ni}_3\text{O}_{10}$ compared to $\text{La}_3\text{Ni}_2\text{O}_7$ stands in stark contrast to the cuprates, where the highest T_c is typically achieved in the trilayer compounds ^[79–81]. This discrepancy in layer-dependent superconductivity between the two systems suggests fundamental differences in their interlayer coupling and underlying superconducting mechanisms.

Electronically, the proximity of the Ni d_{z^2} -derived γ band to the Fermi level under high pressure is also considered a key ingredient for superconductivity in $\text{La}_4\text{Ni}_3\text{O}_{10}$ ^[74]. Figures 1-11c to 1-11e illustrate the electronic band structure of $\text{La}_4\text{Ni}_3\text{O}_{10}$. At ambient pressure, the Fermi surface of $\text{La}_4\text{Ni}_3\text{O}_{10}$ (Figures 1-11c and 1-11d) resembles that of $\text{La}_3\text{Ni}_2\text{O}_7$, consisting of a circular electron pocket α at the Brillouin zone center, a large hole pocket β , and an additional smaller pocket near the zone corner ^[78]. ARPES spectral cuts (Figure 1-11e) reveal a flat γ band located approximately 20 meV below the Fermi level at low temperatures, as reported by Li *et al.* ^[78]. Interestingly, this energy gap closes, and the γ band crosses the Fermi level above the density-wave transition temperature ($T_{\text{DW}} \approx 140$ K), suggesting the gap is density-wave-like in nature. This temperature-dependent evolution contrasts with $\text{La}_3\text{Ni}_2\text{O}_7$ where the position of the γ band remains nearly stationary even above its T_{DW} ^[70]. The distinct behaviors of the γ band in $\text{La}_3\text{Ni}_2\text{O}_7$ and $\text{La}_4\text{Ni}_3\text{O}_{10}$ highlight the subtle differences between these two materials, and the exact role of the γ band in the emergence of superconductivity in both systems warrants further investigation.

1.3.4.2 Hybrid Ruddlesden–Popper Nickelate Superconductors

Hybrid RP nickelates are characterized by the alternating stacking of two different RP phases along the c-axis ^[82]. Figure 1-12a illustrates one such hybrid system, $\text{La}_5\text{Ni}_3\text{O}_{11}$, which comprises alternating layers of the bilayer $\text{La}_3\text{Ni}_2\text{O}_7$ and monolayer La_2NiO_4 phases. Pressure-induced superconductivity was discovered in this compound by Shi *et al.* ^[83]. Figures 1-12b and 1-12c present the ρ – T curves and the corresponding phase diagram of $\text{La}_5\text{Ni}_3\text{O}_{11}$. At ambient pressure, $\text{La}_5\text{Ni}_3\text{O}_{11}$ adopts an orthorhombic $Cmmm$ space group and exhibits a prominent transport anomaly near 170 K, attributed to a density-wave transition. Under

pressure, $\text{La}_5\text{Ni}_3\text{O}_{11}$ undergoes a structural transition to tetragonal $P4/mmm$ symmetry at approximately 4.5 GPa, a significantly lower pressure than that required for $\text{La}_3\text{Ni}_2\text{O}_7$ or $\text{La}_4\text{Ni}_3\text{O}_{10}$. Interestingly, T_{DW} continues to rise with increasing pressure, a behavior that stands in contrast to the observations in $\text{La}_3\text{Ni}_2\text{O}_7$ and $\text{La}_4\text{Ni}_3\text{O}_{10}$. Above 11.7 GPa, the density-wave transition is suppressed while T_{DW} remains unchanged; concurrently, superconductivity begins to emerge. The density-wave transition completely disappears above approximately 13 GPa. Optimal superconductivity is achieved at 23.5 GPa, with a maximum $T_{\text{c,onset}}$ of 64 K and a $T_{\text{c,zero}}$ of 54 K. The pressure-dependent phase diagram of $\text{La}_5\text{Ni}_3\text{O}_{11}$ also exhibits a dome-like feature, similar to $\text{La}_3\text{Ni}_2\text{O}_7$.

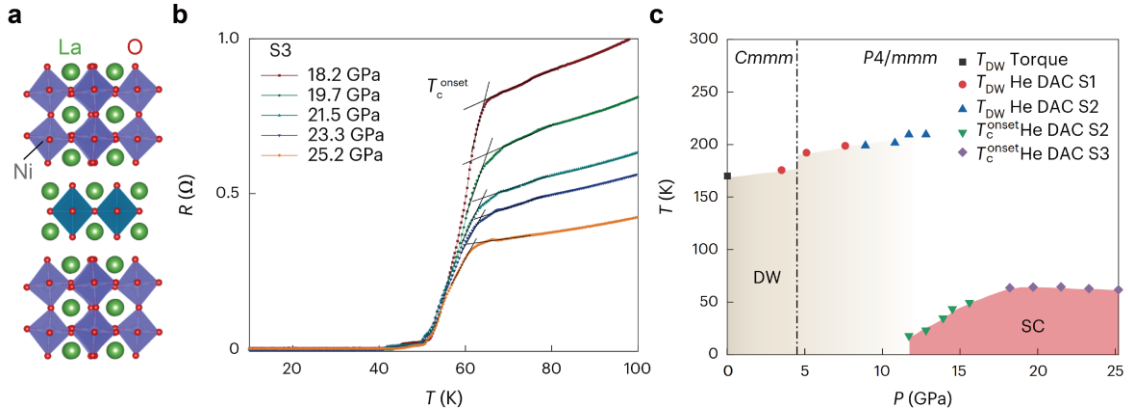


Figure 1-12 Pressure-induced superconductivity in the hybrid RP nickelate $\text{La}_5\text{Ni}_3\text{O}_{11}$. (a) Crystal structure of $\text{La}_5\text{Ni}_3\text{O}_{11}$ showing the alternating stacking of monolayer and bilayer units^[82]. (b) ρ - T curves of $\text{La}_5\text{Ni}_3\text{O}_{11}$ under pressures ranging from 18.2 to 25.2 GPa^[83]. (c) Pressure-temperature phase diagram of $\text{La}_5\text{Ni}_3\text{O}_{11}$ ^[83]. The dash-dotted line denotes the structural transition boundary.

Notably, the onset of superconductivity in $\text{La}_5\text{Ni}_3\text{O}_{11}$ is not concomitant with the structural transition to tetragonal symmetry, which differs phenomenologically from the case of $\text{La}_3\text{Ni}_2\text{O}_7$ and $\text{La}_4\text{Ni}_3\text{O}_{10}$. Shi *et al.*^[84,85] further reported the absence of both density-wave transitions and pressure-induced superconductivity in $\text{La}_3\text{Ni}_2\text{O}_7$ and $\text{La}_4\text{Ni}_3\text{O}_{10}$ samples where the tetragonal structure was stabilized at ambient pressure. Given that the emergence of superconductivity in $\text{La}_5\text{Ni}_3\text{O}_{11}$ aligns more closely with the disappearance of the density-wave transition rather than the structural transition, these findings suggest that the density-wave order rather than the tetragonal symmetry is the essential prerequisite for pressure-induced superconductivity in nickelates.

In addition to the $\text{La}_5\text{Ni}_3\text{O}_{11}$ hybrid phase, pressure-induced superconductivity has also been observed in a hybrid system comprising alternating monolayer and trilayer phases (Figure 1-13a), reported by Puphal *et al.* [86]. Although this hybrid phase shares the same stoichiometric formula, $\text{La}_3\text{Ni}_2\text{O}_7$, as the pure bilayer RP phase, it is designated as the “1313” phase to distinguish its structure, where “1” and “3” represent the monolayer and trilayer units, respectively. A maximum $T_{c,\text{onset}}$ of approximately 80 K was achieved at a pressure of 17.3 GPa (Figure 1-13b). However, zero resistance was not observed. Furthermore, the dependence of the ρ - T curves on the applied electrical current below $T_{c,\text{onset}}$ suggests a possible filamentary nature of the superconductivity in this system. Conversely, a recent study on the 1313 phase by Huang *et al.* [87] reported a significantly lower T_c of approximately 3 K, and successfully observed zero resistance under pressure. Despite these experimental discrepancies, the electronic band structure of the 1313 phase has been investigated using ARPES, reported by Abadi *et al.* [88]. Their results reveal that the Ni d_{z^2} -derived γ band, which is of central interest in RP nickelate superconductivity, lies approximately 20 meV below the Fermi level (Figure 1-13c). This energy position is consistent with that of the γ band observed in $\text{La}_4\text{Ni}_3\text{O}_{10}$.

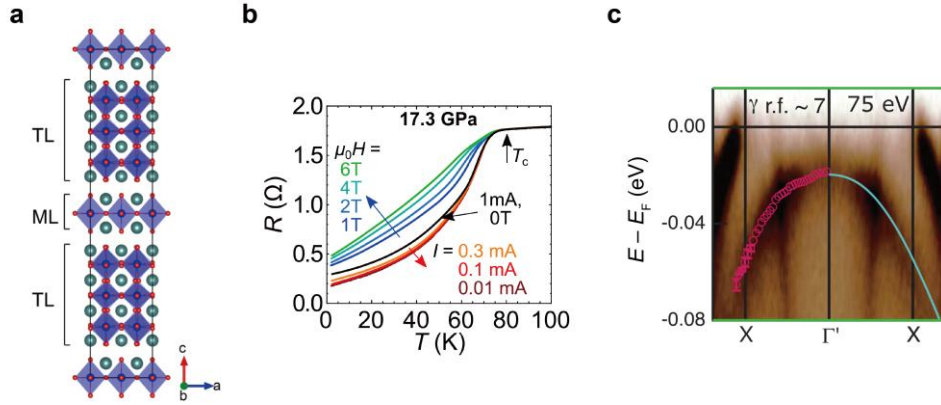


Figure 1-13 Pressured-induced superconductivity in the hybrid 1313-type nickelate $\text{La}_3\text{Ni}_2\text{O}_7$. (a) Crystal structure of the hybrid $\text{La}_3\text{Ni}_2\text{O}_7$ phase, characterized by the alternating stacking of monolayer and trilayer units [86]. (b) ρ - T curves of the hybrid $\text{La}_3\text{Ni}_2\text{O}_7$ phase at 17.3 GPa, measured under various magnetic fields and electrical currents [86]. (c) ARPES spectral cut along a high-symmetry direction, obtained with a photon energy of 75 eV at 7 K [88]. The renormalization factor (r.f.) for the γ band is approximately 7.

In summary, the lattice degrees of freedom provided by these hybrid

nickelates offer a versatile platform to explore the interplay between crystalline structure and superconductivity, paving the way for discovering emergent properties through artificially engineered heterostructures.

1.3.4.3 Multi-Layer Square-Planar Nickelate Superconductors

Figure 1-14a depicts the crystal structures of a series of multi-layer square-planar nickelates, $\text{Nd}_{n+1}\text{Ni}_n\text{O}_{2n+2}$. Their basic structural unit consists of n layers of square-planar NdNiO_2 , separated by a fluorite-type slab. These compounds are typically synthesized via the chemical reduction of their corresponding RP precursor phases to remove the apical oxygen atoms.

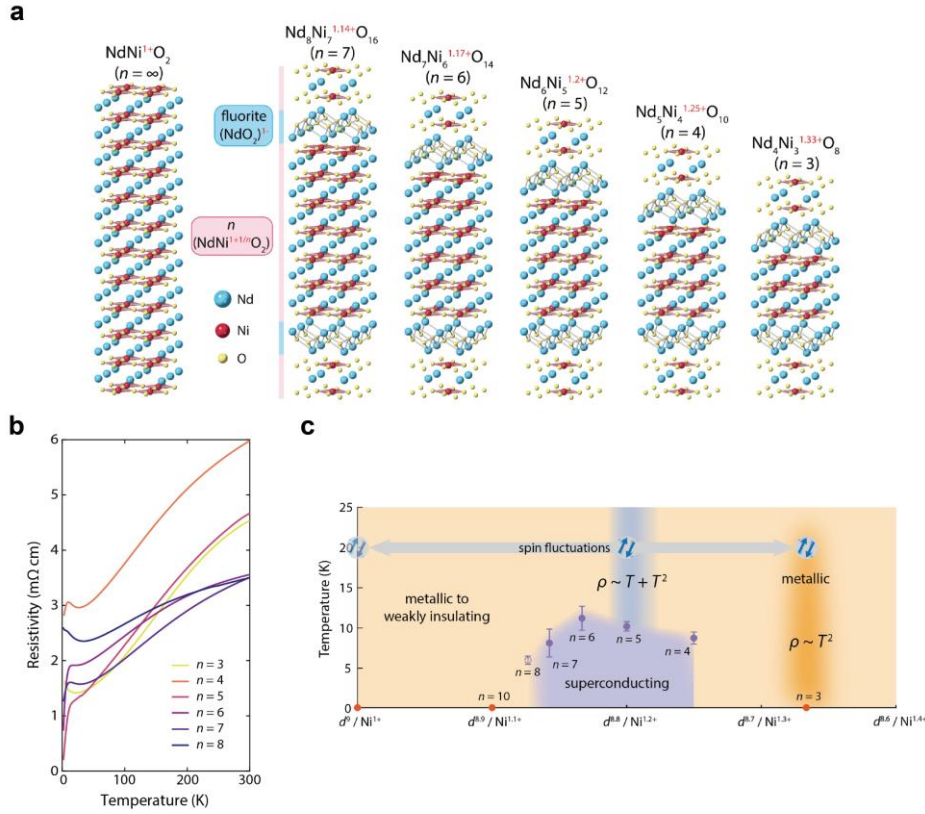


Figure 1-14 Superconductivity in multi-layer square-planar nickelates ^[89]. (a) Crystal structures of multi-layer square-planar nickelates $\text{Nd}_{n+1}\text{Ni}_n\text{O}_{2n+2}$ ($n = 3-7$). (b) ρ - T curves of $\text{Nd}_{n+1}\text{Ni}_n\text{O}_{2n+2}$ for $n = 3-7$. (c) Phase diagram of the $\text{Nd}_{n+1}\text{Ni}_n\text{O}_{2n+2}$ family, as a function of the Ni 3d electron count. The $n = 8$ phase is indicated by a dashed circle, signifying the absence of a distinct superconducting transition in the resistivity.

By varying n , the Ni 3d electron occupancy can be tuned from 8.67 in $\text{Nd}_4\text{Ni}_3\text{O}_8$ to 8.86 in $\text{Nd}_8\text{Ni}_7\text{O}_{16}$, effectively inducing hole doping. $\text{Nd}_6\text{Ni}_5\text{O}_{12}$, whose nominal hole doping level derived from the 3d electron count falls within

the superconducting dome of infinite-layer nickelates, was the first member of this series reported to exhibit superconductivity by Pan *et al.* ^[25]. Recently, additional multi-layer square-planar phases (with n ranging from 4 to 8) have been incorporated into this superconducting family (Figure 1-14b) ^[89]. The resulting phase diagram based on the d electron count (Figure 1-14c) exhibits a dome-like feature similar to that of the infinite-layer nickelates. This structural tuning provides an alternative route to achieve effective hole doping in square-planar nickelates and facilitates the exploration of layer-dependent superconductivity.

In summary, a vast family of nickelate superconductors has been established in the brief period since its discovery in 2019. Active research is ongoing to identify new systems and to elucidate the underlying mechanisms. In particular, given the structural and phenomenological resemblances to cuprate superconductors, comparative studies between these two systems are expected to yield pivotal insights into the long-standing problem of high-temperature superconductivity.

1.4 Motivation and Thesis Outline

Although pressure-induced superconductivity is well established in bilayer, trilayer and related hybrid RP nickelates, the required extreme high-pressure conditions hinder the application of many spectroscopic techniques, such as ARPES and scanning tunneling spectroscopy (STS), to probe their electronic structure in the superconducting state. These characterization methods are essential for providing experimental evidence to address issues specific to RP nickelates such as the emergence of the Ni d_{z^2} -derived γ band at the Fermi surface, as well as broader questions in superconductivity such as pairing symmetry. Therefore, achieving ambient-pressure superconductivity in these compounds is a prerequisite for enabling such characterizations. Furthermore, the T_c record for nickelates at ambient pressure remains stuck near 40 K in the Sm-based infinite-layer system, failing to surpass the McMillan limit which is the traditional threshold between conventional and unconventional superconductors. Given that bilayer RP nickelates exhibit a T_c as high as 96 K under pressure, they possess the potential to exceed the 40 K threshold at ambient pressure.

Based on the above analysis, two fundamental problems motivated the research conducted in this thesis: (1) How to achieve ambient-pressure superconductivity in bilayer RP nickelates, and (2) whether the Fermi surface of superconducting RP nickelates involves the γ band. The outline of this thesis is as follows:

Chapter Two describes the growth of bilayer RP nickelate thin films using gigantic-oxidative atomic-layer-by-layer epitaxy (GAE). A protocol for determining pulse numbers during cation calibration in layer-by-layer epitaxy is primarily introduced. Additionally, the wide thermodynamic window for the phase formation of bilayer RP nickelates enabled by this unique GAE methodology is discussed. The GAE is demonstrated to be a powerful, versatile and flexible tool for oxide thin-film growth.

Chapter Three presents the discovery of ambient-pressure superconductivity in $(\text{La,Pr})_3\text{Ni}_2\text{O}_7$ films, with $T_{\text{c,onset}}$ exceeding the McMillan limit of 40 K. By utilizing compressive epitaxial strain exerted by SrLaAlO_4 substrates and ozone post-annealing, superconductivity is achieved in $(\text{La,Pr})_3\text{Ni}_2\text{O}_7$ at ambient pressure, as confirmed by the dual evidence of zero resistance and the Meissner effect. Furthermore, its magnetic field response, the role of Pr-doping, and its sensitivity to oxygen loss are systematically investigated.

Chapter Four explores the ambient-pressure superconductivity in two nickelate superstructures $(\text{La,Pr})_5\text{Ni}_3\text{O}_{11}$ and $(\text{La,Pr})_7\text{Ni}_5\text{O}_{17}$, which are hybrid structures of monolayer/bilayer and bilayer/trilayer phases, respectively. Comparative ARPES studies of the electronic band structures among pure bilayer $(\text{La,Pr})_3\text{Ni}_2\text{O}_7$, hybrid $(\text{La,Pr})_3\text{Ni}_2\text{O}_7$ (1313 phase), $(\text{La,Pr})_5\text{Ni}_3\text{O}_{11}$ and $(\text{La,Pr})_7\text{Ni}_5\text{O}_{17}$ reveal a direct correlation between the d_{z^2} -derived γ band crossing the Fermi level and the emergence of superconductivity. These findings provide rigorous experimental evidence regarding the role of the γ band, facilitating theoretical studies of the superconducting mechanisms in bilayer nickelates.

The thesis concludes with a summary, and a brief outlook discussing future research directions in the field of nickelate superconductors.

CHAPTER 2 THIN FILM GROWTH OF BILAYER RP NICKELATES VIA GIGANTIC-OXIDATIVE ATOMIC-LAYER-BY-LAYER EPITAXY

The bilayer RP nickelate $\text{La}_3\text{Ni}_2\text{O}_7$, with a formal nickel valence of +2.5, is thermodynamically less stable than either La_2NiO_4 (Ni^{2+}) or LaNiO_3 (Ni^{3+}). Consequently, bulk single-crystal or polycrystalline samples are highly susceptible to the intergrowth of competing RP phases and oxygen loss, imposing stringent requirements on growth parameters ^[54]. Traditionally, the synthesis of RP nickelates $\text{R}_{n+1}\text{Ni}_n\text{O}_{3n+1}$ ($\text{R} = \text{La}, \text{Nd}$) thin films has relied on Oxide Molecular Beam Epitaxy (OMBE) ^[24,90,91]. OMBE, characterized by alternately shuttered evaporation sources and layer-by-layer epitaxy, offers precise control over stoichiometry. However, due to the high-vacuum requirements for molecular beam transport, only low partial pressures of oxidants can be maintained. For instance, even with distilled ozone at 10^{-5} Torr (10^{-3} Pa), as-grown $\text{La}_3\text{Ni}_2\text{O}_7$ films exhibits insulating behavior despite excellent crystallinity confirmed by X-ray diffraction (XRD), as reported by Li *et al.* ^[24]. This transport behavior mirrors that of oxygen-deficient bulk $\text{La}_3\text{Ni}_2\text{O}_{7-\delta}$ samples ($\delta > 0.08$), revealing a limitation in the oxidation potential of conventional OMBE.

Pulse Laser Deposition (PLD) is another mainstream thin-film deposition technique exploited to overcome these oxidative limitations. Unlike OMBE, PLD can operate under relatively high-pressure environments, facilitated by the high kinetic energy of the ejected species generated during laser ablation. Liu *et al.* ^[92] reported $\text{La}_3\text{Ni}_2\text{O}_7$ films grown at 800 °C under 20–35 Pa of oxygen, followed by *in situ* high-pressure annealing (0.5–0.8 atm O_2) at 450 °C. While these samples exhibited an improvement in metallic behavior, XRD analysis revealed inferior crystalline quality compared to samples grown by OMBE. Furthermore, the conventional “block-by-block” growth of PLD hinders precise stoichiometric control, making it difficult to obtain pure-phase samples of complex structures like $\text{La}_3\text{Ni}_2\text{O}_7$ or higher- n RP members.

To address this, Atomic Layer-by-Layer Laser MBE (ALL-Laser MBE) was

developed to mimic the layer-by-layer mode of OMBE within a PLD system, as reported by Lei *et al.* [93]. By alternating the ablation of separate oxide targets (e.g., NiO_x and LaO_y) rather than a single target in the conventional way, high-quality $\text{La}_5\text{Ni}_4\text{O}_{13}$ films were successfully realized.

Building upon this evolution, a Gigantic-Oxidative Atomic-Layer-by-Layer Epitaxy (GAE) methodology was developed [94]. By combining the atomic-scale precision of layer-by-layer growth with the powerful oxidizing capability of high-pressure ozone, GAE accommodates the dual requirements of accurate cation stoichiometry and optimal oxygen content.

All thin-film samples discussed in this thesis were synthesized using this GAE methodology. As its unique growth mode is rarely detailed in the literature, this chapter provides a comprehensive introduction to the GAE growth of bilayer RP nickelates. First, the phase formation of bilayer RP nickelates, which is primarily governed by robust growth kinetics in GAE rather than thermodynamic conditions, is discussed. Subsequently, a growth strategy designed to achieve robust and rapid calibration of cation stoichiometry is introduced. The methodological insights and growth expertise accumulated in this chapter serve as a solid foundation for the subsequent experimental works.

2.1 Comparative Analysis of Conventional PLD and the GAE Growth Mode

Figure 2-1a illustrates the conventional PLD growth routine, using the deposition of $\text{La}_3\text{Ni}_2\text{O}_7$ as an example. The process begins with the synthesis of a polycrystalline $\text{La}_3\text{Ni}_2\text{O}_7$ target from a stoichiometric mixture of La_2O_3 and NiO powders. This mixture is subjected to repeated cycles (at least twice) grinding, pelletizing, and high-temperature sintering to ensure a dense and homogenous target for ultraviolet (UV) laser ablation. Once placed in a high-vacuum chamber, the target is ablated by the laser in the presence of a reactant gas, typically oxygen for oxide synthesis. Upon laser impact, the target surface undergoes rapid heating, resulting in localized melting and vaporization, and the formation of a highly ionized plasma plume. This plume expands and propagates through the background gas, transporting the ablated species towards the heated substrate. These

species subsequently undergo absorption, surface diffusion and nucleation, eventually forming a thin film. By optimizing the laser energy and spot size, the stoichiometry of the target can be effectively transferred to the film, making PLD a convenient and versatile deposition technique [95].

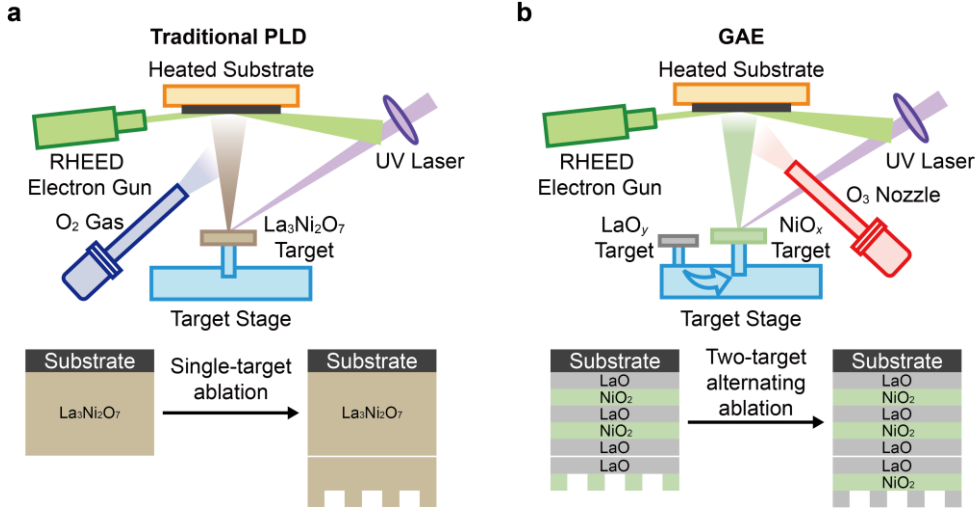


Figure 2-1 Comparison between conventional pulsed laser deposition (PLD) and gigantic-oxidative atomic-layer-by-layer epitaxy (GAE). (a) Schematic illustration of the thin-film growth process in traditional PLD, where a single $\text{La}_3\text{Ni}_2\text{O}_7$ target is ablated, resulting in growth without atomic-layer precision. (b) Schematic illustration of GAE, where NiO_x and LaO_y targets are ablated alternatively to achieve atomic layer-by-layer epitaxy. Ozone is utilized to provide an exceptionally strong oxidizing environment.

While PLD is highly effective for synthesizing oxides with relatively simple structure, such as the perovskite precursors of infinite-layer nickelates [12,28,47], it faces significant challenges with complex structures like $\text{La}_3\text{Ni}_2\text{O}_7$ [92,96]. Precise stoichiometric control is difficult to achieve using a single target, making the film highly susceptible to the intergrowth of competing RP phases such as La_2NiO_4 and $\text{La}_4\text{Ni}_3\text{O}_{10}$ which are thermodynamically more stable. Furthermore, the successful formation of the $\text{La}_3\text{Ni}_2\text{O}_7$ phase in single-target mode relies heavily on the narrow growth window of substrate temperature and oxygen partial pressure, which is difficult to navigate [97]. A further complication is that these parameters simultaneously dictate the oxidizing environment, thereby preventing the independent optimization of phase formation and oxygen stoichiometry.

In contrast, the GAE methodology, characterized by the alternating ablation of two targets and the integration of ozone (O_3) as a highly reactive oxidant, offers a powerful solution for synthesizing RP nickelates with superior crystalline

quality and optimal oxygen content. The growth process is illustrated in Figure 2-1b. To grow $\text{La}_3\text{Ni}_2\text{O}_7$, which possesses a characteristic $\text{LaO-NiO}_2\text{-LaO-NiO}_2\text{-LaO}$ stacking sequence, NiO_x and LaO_y targets are ablated sequentially to replicate the desired atomic stacking order. This approach assumes that interface discontinuities have been addressed through substrate treatment or the deposition of a buffer layer, details of which will be discussed in subsequent chapters.

Interestingly, the typical deposition sequence for bilayer nickelates in the MBE is $\text{LaO-LaNiO}_2\text{-NiO}_2\text{-LaO}$ [98]. This counterintuitive sequence is deliberately designed to account for the layer rearrangement phenomenon observed during MBE growth [98,99]. If the deposition strictly followed the crystal structure, the successive deposition of two LaO layers (one terminating the previous bilayer and the other initiating the next) would form a $\text{LaO}]\text{-[LaO-NiO}_2$ configuration. This configuration is thermodynamically unstable under MBE growth configuration and tends to rearrange into a more stable perovskite-like structure $\text{LaO}]\text{-[NiO}_2\text{-LaO}$, where the NiO_2 layer inverts with the LaO layer beneath it. By adopting the $\text{LaO-LaNiO}_2\text{-NiO}_2\text{-LaO}$ sequence, the intended bilayer structure $\text{LaO-NiO}_2\text{-LaO-NiO}_2\text{-LaO}$ is successfully obtained after this inversion.

Notably, this layer rearrangement is also observed in GAE when using the same $\text{LaO-LaNiO}_2\text{-NiO}_2\text{-LaO}$ sequence. However, a deposition sequence that directly follows the crystal structure also yields high-quality films in GAE, at least when using LaAlO_3 and SrLaAlO_4 substrates. The origin of this intriguing discrepancy between MBE and GAE growth mechanisms remains an open question and warrants further investigation.

To maximize the oxidative potential, purified ozone is delivered through a specially designed nozzle positioned in close proximity to the heated substrate (approximately 4 cm) [94]. This configuration allows ozone to be ejected directly onto the sample surface, thereby minimizing thermal decomposition and ozone loss, given its instability at high temperatures.

The GAE system utilized in this work is a custom-designed apparatus manufactured by Arrayed Materials (China). It is equipped with a Coherent KrF excimer laser operating at a wavelength of 248 nm with a pulse duration of 25 ns.

2.2 Decoupling of Phase Formation and Oxygen Stoichiometry in GAE

In both the bulk single-crystal growth of $\text{La}_3\text{Ni}_2\text{O}_7$ using an optical floating zone furnace and thin film growth via single-target PLD, the successful formation of the $\text{La}_3\text{Ni}_2\text{O}_7$ phase relies on the precise tuning of two critical thermodynamic parameters, temperature and oxygen partial pressure (P_{O_2}) [97,100]. Figure 2-2 illustrates the growth phase diagrams for RP nickelates in single-crystal growth (Figure 2-2a) and PLD thin-film deposition (Figure 2-2b). It is evident that LaNiO_3 (Ni^{3+}) requires the strongest oxidizing environment due to its high nickel valence state, whereas La_2NiO_4 (Ni^{2+}) requires the lowest P_{O_2} . For $\text{La}_3\text{Ni}_2\text{O}_7$ ($\text{Ni}^{2.5+}$) and $\text{La}_4\text{Ni}_3\text{O}_{10}$ ($\text{Ni}^{2.67+}$), the required P_{O_2} windows are nested within a narrow region between those of LaNiO_3 and La_2NiO_4 . Specifically, the growth window for bulk $\text{La}_3\text{Ni}_2\text{O}_7$ ranges from approximately 10–20 bar, while for single-target PLD, it spans 50–150 mTorr. In both cases, the ratio between the upper and lower limits is only about 2–3, representing an extremely narrow operational window. Consequently, this thermodynamic growth window is not only difficult to locate but also makes the suppression of intergrown competing phases a significant challenge.

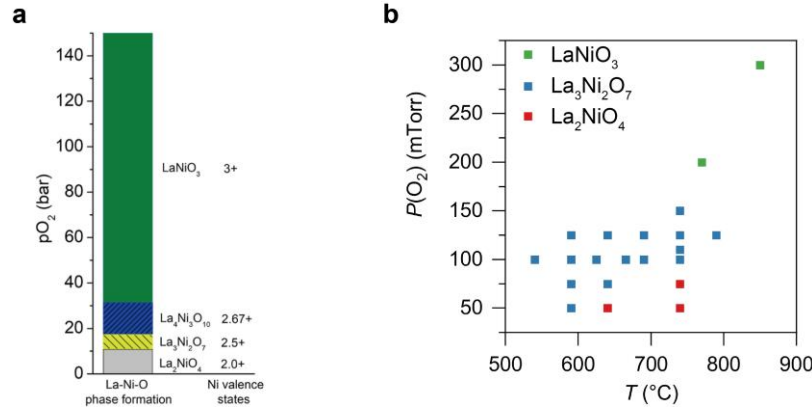


Figure 2-2 Empirical growth phase diagrams of RP nickelates. (a) Phase diagram for the growth of bulk RP nickelate single crystals using the optical floating zone method, shown as a function of oxygen partial pressure (P_{O_2}) [100]. (b) Phase diagram for epitaxial thin-film growth of RP nickelates on SrLaAlO_4 substrates via conventional single-target PLD, as a function of P_{O_2} and substrate temperature [97].

In contrast, the GAE methodology offers a significantly broader thermodynamic growth window for bilayer RP nickelates. Facilitated by the high kinetic

energy of the species ablated by the laser, these particles undergo sufficient surface diffusion across the substrate. The exact amount of material required to complete an atomic layer is primarily determined by the number of laser pulses applied to the targets. Once the pulse numbers for full-layer coverage (e.g., for NiO_x and LaO_y in the case of $\text{La}_3\text{Ni}_2\text{O}_7$) are calibrated, the crystal structure can be assembled through the sequential deposition of each atomic layer. This phase formation mechanism, governed by robust growth kinetics, facilitates the synthesis of thermodynamically metastable bilayer nickelates across a wide range of oxidizing environments and temperatures, as shown in Figure 2-3a.

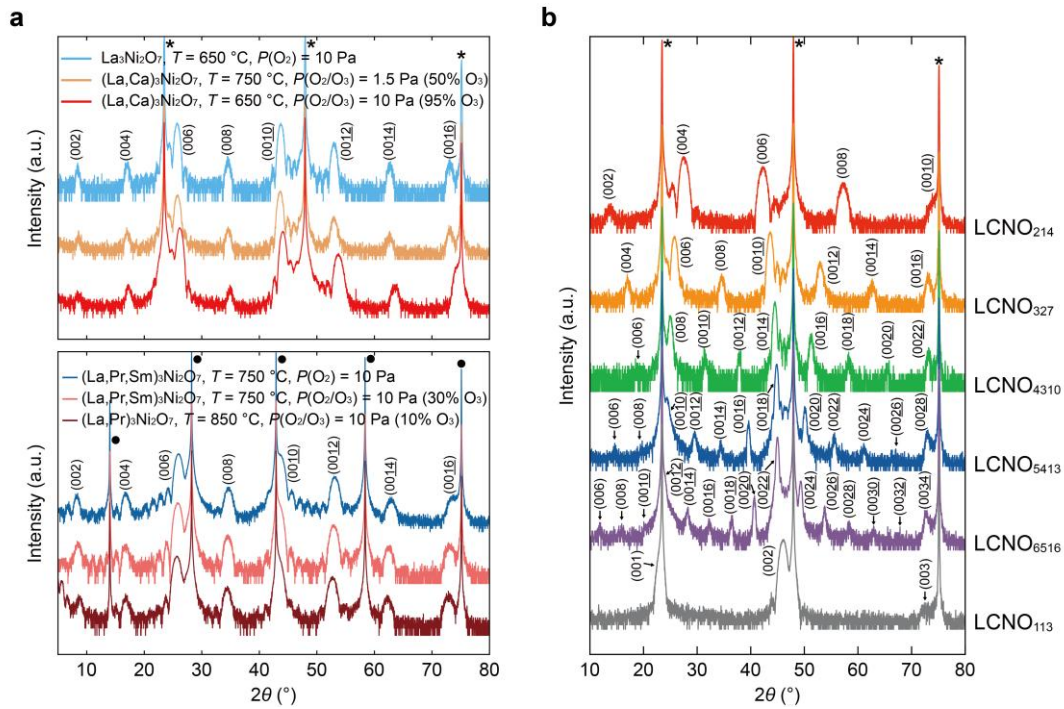


Figure 2-3 Structural characterization of GAE-grown nickelates. (a) Out-of-plane XRD patterns for various bilayer RP nickelates synthesized under different temperature and oxidizing environments. The upper and lower panels represent films grown on LaAlO_3 and SrLaAlO_4 substrates, respectively. Substrate peaks for LaAlO_3 and SrLaAlO_4 are marked with asterisks and solid spheres, respectively. Detailed chemical compositions for $(\text{La,Ca})_3\text{Ni}_2\text{O}_7$ include $\text{La}_{2.76}\text{Ca}_{0.24}\text{Ni}_2\text{O}_7$ (yellow curve) and $\text{La}_{2.52}\text{Ca}_{0.48}\text{Ni}_2\text{O}_7$ (red curve). Both $(\text{La,Pr,Sm})_3\text{Ni}_2\text{O}_7$ samples correspond to $\text{La}_2\text{Pr}_{0.5}\text{Sm}_{0.5}\text{Ni}_2\text{O}_7$, and $(\text{La,Pr})_3\text{Ni}_2\text{O}_7$ corresponds to $\text{La}_2\text{PrNi}_2\text{O}_7$. Films on LaAlO_3 are 5 unit cells (UC) thick, while those on SrLaAlO_4 are 3 UC thick (1 UC = two bilayer structures). (b) Out-of-plane XRD patterns for Ca-doped RP nickelates $(\text{La}_{0.92}\text{Ca}_{0.08})_{n+1}\text{Ni}_n\text{O}_{3n+1}$ ($n = 1-5, \infty$) on LaAlO_3 substrates, grown under identical thermodynamic conditions (750°C , 1.5 Pa O_2/O_3 mixture with 50% O_3). Film thicknesses from top to bottom are 6.4 nm ($n = 1$), 10.5 nm ($n = 2$), 14.3 nm ($n = 3$), 18.2 nm ($n = 4$), 22.1 nm ($n = 5$) and 7.6 nm ($n = \infty$), respectively.

Bilayer RP nickelate thin films can be successfully synthesized using GAE across a wide range of oxidizing environments, extending from the relatively weak conditions (10 Pa pure O₂), to moderately strong (1.5 Pa O₂/O₃ mixture with 50% O₃), and up to the exceptionally strong oxidizing potentials (10 Pa O₂/O₃ mixture with 95% O₃). The high crystalline quality of these films is evidenced by X-ray diffraction (XRD) patterns, which exhibit sharp diffraction peaks characteristic of bilayer RP nickelates, accompanied by distinct Kiessig fringes that indicate smooth surfaces and interfaces. This growth window, in terms of oxidation potential, is significantly broader than that available to conventional single-target PLD.

The typical growth temperature for films on LaAlO₃ substrates ranges from 650–750 °C, while for SrLaAlO₄ substrates, it is shifted higher to 750–850 °C. This temperature is monitored during growth using an infrared pyrometer directed at the back of the sample holder. It should be noted that a deviation exists between the setpoint temperature and the actual substrate surface temperature due to varying thermal properties. Specifically, for SrLaAlO₄ substrates which possess lower thermal conductivity, a higher setpoint temperature is required to ensure that the substrate surface provides sufficient energy for effective adatom diffusion.

Beyond the stabilization of the bilayer phase, GAE can accommodate the growth of an entire series of RP members, (La_{0.92}Ca_{0.08})_{n+1}Ni_nO_{3n+1} ($n = 1-5$ and ∞), under identical thermodynamic conditions (750 °C and 1.5 Pa O₂/O₃ mixture with 50% O₃), as shown in Figure 2-3b. This capability further demonstrates that phase formation in the GAE methodology is largely decoupled from strict thermodynamic selection. Such a feature grants GAE a definitive advantage in overcoming thermodynamic limitations, enabling the growth of hybrid nickelate thin films such as the 1212 phase. These complex structures, containing components with distinct nickel valence state such as La₃Ni₂O₇ (Ni^{2.5+}) and La₂NiO₄ (Ni²⁺), can thus be synthesized within a single, uniform oxidizing environment [94].

In the GAE methodology, growth temperature and the partial pressures of oxygen or ozone are primarily employed to modulate oxygen content and achieve optimal oxygen stoichiometry. Figure 2-4 demonstrates a significant change in

thermodynamic conditions to enhance oxidative capability and eliminate oxygen vacancies in bilayer nickelates. In this experiment, the oxidizing environment was elevated from a 1.5 Pa O_2/O_3 mixture with 20% O_3 to a 10 Pa mixture with 95% O_3 , creating a nearly pure ozone environment. This transition plays a critical role in strengthening the oxidation potential. Consequently, the resulting film exhibits a substantial decline in room-temperature resistance (from 336 to 123 Ω at 300 K), and evolves from insulating to metallic behavior with only a subtle resistivity upturn near 30 K (Figure 2-4b). This trend suggests an effective suppression of oxygen vacancies during growth. Furthermore, the XRD patterns of both samples are comparable (Figure 2-4a), which excludes the possibility of intergrowth with more conducting RP phases (such as $n = 3$ trilayer phases) as the cause of improved conductivity. Although the growth temperature was decreased from 750 to 650 $^{\circ}\text{C}$, which has a complex effect on oxidation, it further highlights the flexibility of GAE in maintaining phase stability while significantly altering the thermodynamic parameters.

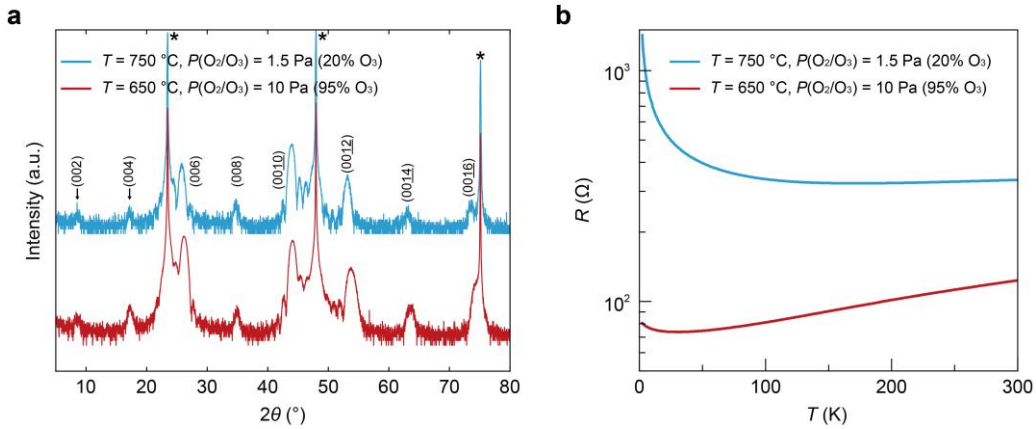


Figure 2-4 Structural and transport properties of $\text{La}_{2.52}\text{Ca}_{0.48}\text{Ni}_2\text{O}_7/\text{LaAlO}_3$ under varying growth conditions. (a) Out-of-plane XRD patterns and (b) temperature-dependent resistance curves for two samples grown under different temperatures and oxidizing environments. Both films are 5UC thick and electrical transport was measured using an identical van der Pauw geometry, allowing for a direct comparison of resistances to reflect the intrinsic evolution of resistivity.

Notably, the XRD diffraction peaks of the fully oxidized sample (red curve) exhibits an overall shift toward higher angles (right) compared to the less oxidized sample (blue curve), indicating a shrinkage of the c -axis lattice constant. This contraction is likely due to the removal of oxygen vacancies, whose presence

typically expands the lattice. It is also noteworthy that the red XRD pattern displays superior peak intensity. This improvement is attributed to enhanced stoichiometric precision enabled by higher pulsed counts. Specifically, the pulse required for monolayer coverage of NiO_x and $(\text{La,Ca})\text{O}_y$ targets increased from 91/80 to 140/185 (at identical laser fluence) when the background gas was switched to 10 Pa nearly pure ozone. The denser background gas scatters the ablated species more significantly during transport, necessitating more laser pulses to achieve full atomic layer coverage. A large pulse number such as 185 allows for a finer adjustment of cation stoichiometry compared to 80. The deviation of a single pulse from the optimal 185 results in an error of only 0.5%, thereby achieving a stoichiometric precision better than 1%.

In summary, within the GAE framework, thermodynamic conditions do not determine the phase formation of RP nickelates but instead serve as a versatile tool for the precise modulation of oxygen stoichiometry.

2.3 A Two-Step Protocol for Cation Stoichiometry Calibration

In the GAE mode, calibrating the cation stoichiometry relies on determining the precise number of laser pulses required to deposit exactly one atomic monolayer from each target. These pulse numbers are sensitive to several experimental factors, including chamber pressure, background gas composition, laser fluence and target density. Rapid and accurate calibration is essential whenever these conditions are modified.

The cation stoichiometry of RP nickelates ($\text{La}_{n+1}\text{Ni}_n\text{O}_{3n+1}$) is governed by two decoupled parameters that can be optimized independently. The first is the cation ratio (the La/Ni ratio), which is $(n + 1)/n$ for a specific n -layer phase. The second is the structural periodicity, representing the cumulative thickness of a single deposition cycle (e.g., $\text{LaO-NiO}_2\text{-LaO-NiO}_2\text{-LaO}$ for the bilayer phase). To ensure that each atomic layer achieves full monolayer coverage without under- or over-deposition, the periodicity of one complete cycle must be precisely calibrated to match half of the c -axis lattice constant of the target phase.

The La/Ni ratio is primarily reflected by the position of the most prominent

peak in the XRD pattern, typically the $(00\ 4n+2)$ peak for a standard RP phase. This peak corresponds to the average monolayer thickness and exhibits the highest diffraction intensity. (Note: $4n + 2$ arises because 1 UC of $\text{La}_{n+1}\text{Ni}_n\text{O}_{3n+1}$ contains two n -layer blocks, totaling $2 \times (n + n + 1) = 4n + 2$ atomic layers).

This peak position is highly sensitive to La/Ni ratio, but relatively insensitive to the overall structural periodicity^[101]. As n increases, La/Ni ratio decreases, leading to higher proportion of NiO_2 layers. Since NiO_2 layers thinner than LaO layers, the average monolayer thickness is reduced, shifting the $(00\ 4n+2)$ peak toward higher angles. As shown in Figure 2-5a, the XRD 2θ positions of the $(00\ 4n+2)$ peaks for $n = 2$ to 5 members on LaAlO_3 substrates exhibit a remarkably linear relationship with the cation ratio. This linear regime allows the La/Ni ratio of an off-stoichiometric film to be precisely calculated from its peak position, even if it does not represent a standard RP phase.

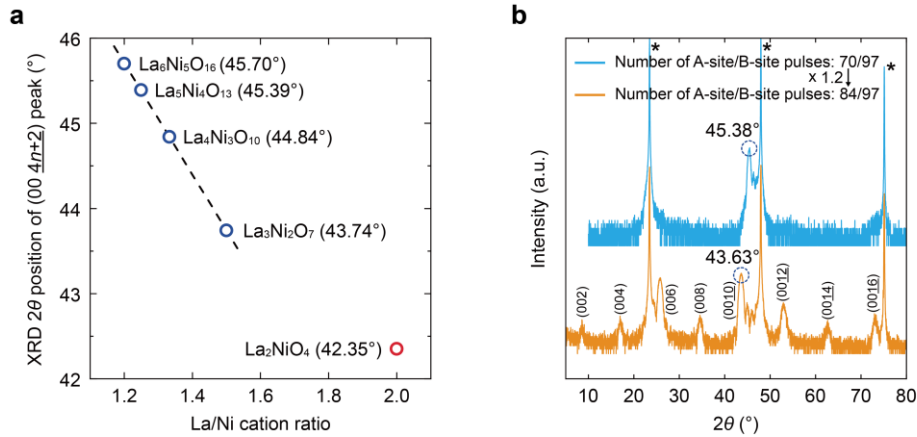


Figure 2-5 Calibration of the La/Ni cation ratio. (a) XRD 2θ position of the $(00\ 4n+2)$ peak as a function of the La/Ni cation ratio $(n + 1)/n$ for $\text{La}_{n+1}\text{Ni}_n\text{O}_{3n+1}$ on LaAlO_3 ($n = 1-5$). The data point for La_2NiO_4 ($n = 1$, red) deviates from the linear trend observed in high- n members. Data adapted from ref. [24]. (b) XRD evolution of 5UC thick $(\text{La}_{0.92}\text{Ca}_{0.08})_3\text{Ni}_2\text{O}_7/\text{LaAlO}_3$ films as the pulse ratio is adjusted from 70/97 to 84/97. The shift of the primary diffraction peak (dashed circle) toward the bilayer position confirms the successful stoichiometry correction.

Figure 2-5b demonstrates a practical application of this calibration during the growth of $(\text{La}_{0.92}\text{Ca}_{0.08})_3\text{Ni}_2\text{O}_7$ on LaAlO_3 . For clarity, the rare-earth $(\text{La,Ca})\text{O}_y$ target is referred to as the A-site, and the NiO_x target as the B-site. With the B-site pulses already optimized for full coverage, an initial A-site pulse count of 70 yielded a peak at 45.38° . This position is higher than the ideal $n = 2$

position (43.74°) and closely matches the $(00\ \underline{18})$ peak of $\text{La}_5\text{Ni}_4\text{O}_{13}$ (45.39° , $n = 4$). This indicates an A-site deficiency, with the current 70/97 pulses corresponding to a La/Ni ratio of 5/4. To achieve the $n = 2$ ratio ($\text{La/Ni} = 3/2 = 6/4$), the A-site pulses were multiplied by a factor of 6/5 to 84. Applying the corrected pulses of 84/97 successfully yielded the bilayer phase, as evidenced by the complete series of diffraction peaks (orange curve).

The aforementioned example assumes an already optimized B-site pulse count. In a more general scenario, such as that shown in Figure 2-6, both A-site and B-site pulses may deviate significantly from their optimal values. This specific case occurred during the growth of $(\text{La}_{0.84}\text{Ca}_{0.16})_3\text{Ni}_2\text{O}_7$ on LaAlO_3 when the background environment was transitioned from a 1.5 Pa O_2/O_3 mixture to a nearly pure 10 Pa ozone atmosphere. Both the increase in total chamber pressure and the shift to a denser O_3 medium enhance the scattering of the ablated species, thereby necessitating a substantial increase in the required pulse numbers for monolayer coverage.

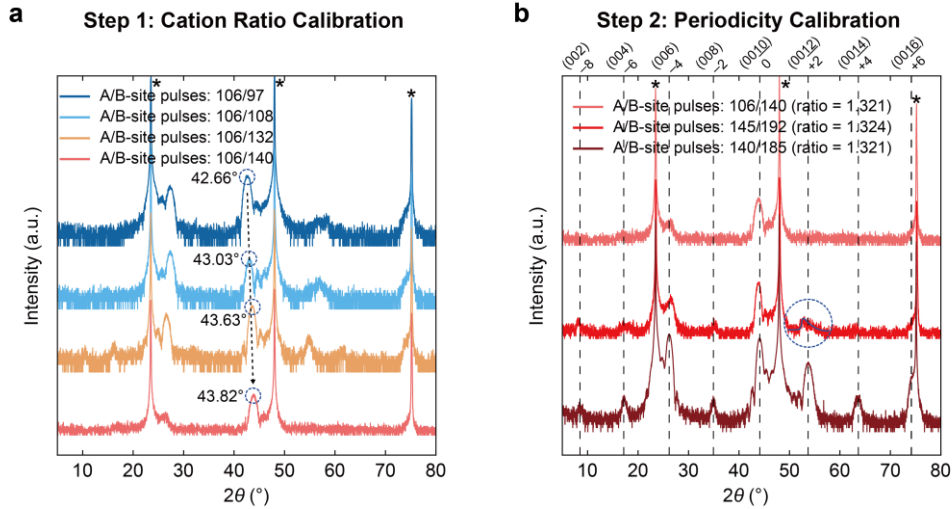


Figure 2-6 Two-step calibration of cation stoichiometry. (a) XRD evolution during the first step: cation ratio calibration. The B-site pulse count is incrementally increased to shift the “ratio peak” (indicated by the dashed circle) to the target 2θ position corresponding to the $n = 2$ phase. (b) XRD evolution during the second step: periodicity calibration. The A/B-site pulse counts are scaled proportionally to maintain the cation ratio while optimizing layer coverage. A $(00\ \underline{12})$ peak with an asymmetric, non-Gaussian contour is highlighted with a dashed circle and sketched outline. Vertical dashed lines indicate the optimized $(00\ l)$ peak positions for reference. Indices below the $(00\ l)$ labels show the relative order of each peak with respect to the $(00\ \underline{10})$ reflection. All samples are 5UC $(\text{La}_{0.84}\text{Ca}_{0.16})_3\text{Ni}_2\text{O}_7$ films on LaAlO_3 , grown under identical temperature, oxidizing environment and laser fluence, with pulse numbers as the sole variables.

The first step of the calibration involves optimizing the cation ratio. This is achieved by pushing the specific XRD reflection that is sensitive to the La/Ni ratio (hereafter referred to as the “ratio peak”) to the desired 2θ position (Figure 2-6a). Based on the previous analysis, increasing the A-site pulses or decreasing the B-site pulses elevates the La/Ni ratio, pushing the ratio peak toward lower 2θ angles. Conversely, the peak shifts toward higher angles when the A-site count is reduced or the B-site count is increased. The initial XRD pattern (dark blue curve) exhibited a ratio peak at 42.66° , which is lower than the ideal (00 $\underline{10}$) position for pure $\text{La}_3\text{Ni}_2\text{O}_7/\text{LaAlO}_3$ (43.74°). Accounting for the chemical pressure effect induced by the smaller Ca^{2+} dopants, the target (00 $\underline{10}$) position was estimated to be 43.85° . To compensate for the reduced deposition rate caused by the higher pressure and ozone concentration, increasing the B-site pulses, rather than decreasing the A-site pulses, was chosen to shift the peak while simultaneously increasing the film thickness. Following the synthesis of three additional samples where B-site pulses were increased from 97 to 140, the ratio peak was successfully shifted to 43.82° , effectively achieving the target cation ratio.

The second step involves the calibration of structural periodicity by scaling the A-site and B-site pulse numbers proportionally. This follows a systematic approach proposed by Barone *et al.* ^[101], which utilizes satellite peaks to determine the proper periodicity. As shown in Figure 2-6b, the XRD pattern of a standard bilayer RP nickelate can be modeled as a series of satellite peaks distributed around the (00 $\underline{10}$) peak (indexed as $L = 0$). This central peak is primarily determined by the cation ratio and remains relatively insensitive to periodicity. The surrounding satellite peaks are indexed as $L = \pm 2, \pm 4, \dots$ based on their relative positions. The spacing between these satellite peaks and the 0-index peak directly reflects the average out-of-plane periodicity (Δ) and serves as a gauge for calibration ^[101].

In cases where the initial film thickness deviates significantly from the ideal periodicity, as seen in the top curve of Figure 2-6b, few satellite peaks are discernible. In such instances, the thickness is first roughly adjusted toward the target value. For this sample, the thickness estimated from the fit of its X-ray reflectivity (XRR) curve was 7.75 nm, while the theoretical thickness for a 5 UC

bilayer nickelate (based on the ideal (00 10) position) is approximately 10.6 nm. Consequently, a scaling factor of 1.37 (10.6/7.75) was applied to the initial pulse counts (106/140), resulting in a new set of 145/192.

In the resulting film (middle curve), multiple satellite peaks emerge while the (00 10) peak position remains unchanged, confirming its decoupling from periodicity. Notably, the (00 12) peak (highlighted by the dashed circle) exhibits an asymmetric, non-Gaussian contour and tilts toward the 0-index peak. This reduced spacing between the +2 satellite and the 0-index peak indicates a periodicity larger than the optimal value. To quantify this deviation, a correction factor, c , is introduced to calculate the adjusted periodicity, Λ_i , using the following relation ^[101]:

$$\Lambda_i = \frac{(L_i + l_0 c) \lambda}{2 \sin(\theta_i)}, \quad (2-1)$$

where L_i is the satellite index of the selected peak relative to 0-index peak (00 l_0), θ_i is the XRD position of the selected peak, and λ is the X-ray wavelength. For this sample, a reliable set of satellite peaks ($L = -4, -2, 0, +2$) were selected to generate an array Λ of four adjusted periodicities. By varying c between 0.8 and 1.2, the optimal factor was determined as the one that minimized the standard deviation of the Λ array. Detailed derivation of this algorithm can be found in ref. [101].

From a physical perspective, in a perfect RP crystal structure, the c-axis lattice constant (and thus the periodicity) derived from every (00 l) diffraction peak must be identical. This requirement provides the fundamental motivation for the algorithm, to find a factor c that yields the minimal variance among adjusted periodicities. This process can be operated iteratively to converge on the ideal periodicity. In this case, the first iteration yielded $c = 1.037$. Dividing the previous pulse counts (145/192) by this factor resulted in the corrected pulses of 140/185. This optimized set yielded a superior bilayer nickelate film (bottom curve).

In summary, a robust two-step cation stoichiometry calibration protocol has been established during the growth of bilayer nickelates on LaAlO₃ substrates. This reproducible and versatile method has been successfully extended to other

substrates such as SrLaAO_4 and NdGaO_3 , significantly improving the efficiency of sample optimization.

2.4 Summary and Conclusions

This chapter provides a systematic introduction to the thin-film growth of bilayer RP nickelates utilizing the unconventional GAE methodology. The discussion is centered on two primary perspectives, the role of thermodynamic conditions in GAE and the establishment of a robust two-step protocol for cation stoichiometry calibration.

By successfully synthesizing bilayer nickelate thin films across a wide range of temperature and oxidizing environments, and by stabilizing a series of RP phases $(\text{La,Ca})_{n+1}\text{Ni}_n\text{O}_{3n+1}$ ($n = 1-5, \infty$) under identical thermodynamic conditions, it is demonstrated that GAE bypasses the stringent thermodynamic selection inherent in conventional single-target PLD. In the GAE framework, the growth temperature and oxidizing environment serve as versatile tools for modulating oxygen stoichiometry rather than determining phase formation. Furthermore, the exceptional oxidative power provided by high-concentration ozone is shown to be effective in suppressing oxygen vacancies in bilayer nickelates.

Phase stabilization in GAE is shown to depend on the precise control of cation stoichiometry through its unique layer-by-layer growth mode. Accurate stoichiometry is achieved by determining the exact pulse numbers required for each target to ensure full atomic monolayer coverage without under- or over-deposition. A two-step calibration protocol has been established. First, the cation ratio is optimized by shifting the “ratio peak” in the XRD pattern to the target position. Subsequently, the A-site and B-site pulse numbers are scaled proportionally to match the ideal structural periodicity, guided by the analysis of satellite peaks.

In conclusion, the GAE methodology is demonstrated to be a powerful, robust and flexible tool for the thin film growth of complex RP nickelates. The growth expertise and calibration strategies summarized in this chapter provide a solid experimental foundation for the sample optimization and physical investigations presented in the subsequent chapters of this thesis.

CHAPTER 3 AMBIENT-PRESSURE SUPERCONDUCTIVITY ONSET ABOVE 40 K IN (La,Pr)₃Ni₂O₇ FILMS

The discovery of pressure-induced superconductivity in La₃Ni₂O₇ has provided a fertile playground for exploring the mechanisms of high-temperature superconductivity [52]. However, the requirement of extreme hydrostatic pressure (typically > 14 GPa) significantly hinders the application of diverse characterization techniques for comprehensive studies. This limitation underscores the urgent need to achieve ambient-pressure superconductivity in La₃Ni₂O₇.

At ambient pressure, bulk La₃Ni₂O₇ possesses a pseudo-tetragonal in-plane lattice constant of approximately 3.83 Å and a c-axis lattice constant of 20.53 Å [102]. Upon increasing the pressure to approximately 14 GPa, the in-plane and c-axis lattice constants contract to 3.75 Å and 19.94 Å, respectively [52]. This represents a substantial compressive strain of approximately 2% in-plane and 3% out-of-plane (Figure 3-1a). Within this pressure regime, the material undergoes a structural transition accompanied by a distinct superconducting transition in resistivity. Epitaxial thin films, which inherently exhibit lattice-mismatch-induced strain, are a promising platform to emulate these high-pressure effects at ambient pressure.

In thin film heterostructures, the epitaxial strain is governed by the relative difference between the in-plane lattice constants of the bulk material and the substrate (Figure 3-1b). Such substrate-induced strain can stabilize emergent properties non-existent in the bulk [103]. Notably, in cuprates such as (La,Sr)₂CuO₄, compressive strain has been shown to significantly enhance T_c [104,105]. However, unlike hydrostatic pressure which compresses the lattice isotropically, epitaxial strain follows a Poisson-like relation. In-plane compression typically results in out-of-plane elongation, and vice versa. This anisotropy makes the selection of an appropriate substrate a critical challenge.

Figure 3-1c compares the in-plane lattice constant of bulk La₃Ni₂O₇ at ambient pressure with those of commonly used substrates. The lattice mismatch (f) between a SrLaAlO₄ (SLAO) substrate (a_s , the in-plane lattice constant of the

substrate) and the bulk La₃Ni₂O₇ (a_e , the in-plane pseudo-tetragonal lattice constant of the bulk material), calculated as $f = (a_s - a_e)/a_e$, yields a biaxial compressive strain of approximately 2%. This value closely matches the in-plane compression observed in superconducting bulk La₃Ni₂O₇ under high pressure.

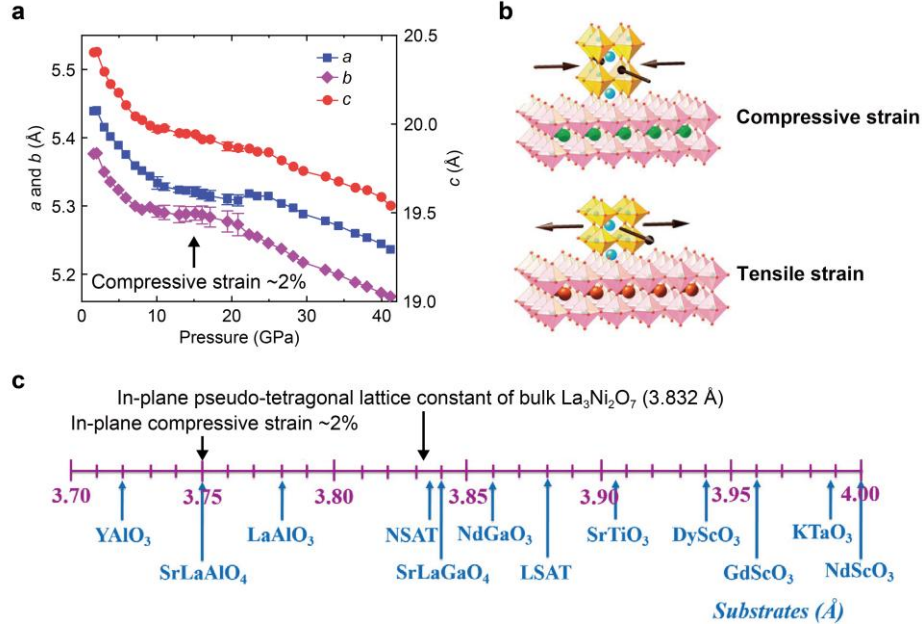


Figure 3-1 Comparison between bulk La₃Ni₂O₇ lattice constants and candidate substrates. (a) Pressure-dependence of the a , b and c -axis lattice constants of La₃Ni₂O₇ ^[52]. (b) Schematic illustration of epitaxial compressive (top) and tensile (bottom) strain exerted by the substrate on the thin film ^[106]. (c) In-plane lattice constants of various commercial substrates in comparison with bulk La₃Ni₂O₇ ^[107].

This chapter reports the realization of ambient-pressure superconductivity in (La,Pr)₃Ni₂O₇ thin films grown on SLAO substrates. The growth process and structural characterization are first detailed. Beyond compressive strain, the critical role of post-annealing in optimizing the superconducting properties is discussed. Finally, the magnetotransport properties and thermal instability of the (La,Pr)₃Ni₂O₇ thin films are investigated.

3.1 Ambient-Pressure Superconductivity in (La,Pr)₃Ni₂O₇ Thin Films

La_{2.85}Pr_{0.15}Ni₂O₇ thin films with a thickness 3UC were epitaxially grown on treated SrLaAlO₄ (SLAO) substrates (Figure 3-2a). Ambient-pressure superconductivity is achieved through the in-plane compressive strain exerted by the

SLAO substrate, and post-growth ozone annealing which effectively suppresses oxygen vacancies. Figure 3-2b presents the temperature-dependent sheet resistivity (R_s – T) for an optimally grown and annealed sample. The superconducting onset temperature, $T_{c,onset}$, is defined as the point where the R_s – T curve deviates from its linear fit from 50–60 K (Figure 3-2c). For this sample, $T_{c,onset}$ reaches 45 K, exceeding the McMillan limit (40 K). In this temperature regime, the application of a 14 T magnetic field suppresses the resistivity drop, confirming that the transition originates from the emergence of superconducting phases. Below $T_{c,onset}$, the resistivity gradually declines toward a zero-resistance state (Figure 3-2d). The broad transition width and a discernible two-step feature, can be interpreted within the framework of Josephson-coupled superconducting puddles^[108]. This behavior likely stems from inhomogeneities within the film, potentially due to localized variations in crystalline quality or a non-uniform oxygen distribution. In this scenario, superconductivity first emerges locally below $T_{c,onset}$, while global phase coherence is only established at much lower temperatures through Josephson coupling between separated superconducting puddles, resulting in the substantially lower $T_{c,zero}$.

Beyond zero resistance, the Meissner effect, another definitive hallmark of superconductivity, was characterized using a two-coil mutual inductance technique (Figure 3-2e). In this setup, a primary driving coil (operating at an alternating current of 20 kHz and 5 μ A) generates a magnetic field. In the normal state, this field penetrates the film and induces a voltage in the pickup coil located beneath the sample. Upon transitioning into the superconducting state, the establishment of global phase coherence leads to magnetic field expulsion, causing a decline in the real part of the pickup voltage ($\text{Re}(V_P)$). The temperature at which this diamagnetic signal emerges is defined as the Meissner temperature (T_M). As shown in Figure 3-2f, a 3UC La_{2.85}Pr_{0.15}Ni₂O₇ film exhibits a clear diamagnetic response with $T_M = 8$ K, identified by the deviation of the imaginary component $\text{Im}(V_P)$ from its horizontal linear baseline. This robust diamagnetic signal further confirms superconductivity in these La_{2.85}Pr_{0.15}Ni₂O₇ films.

Figure 3-2g displays the R – T curves for several La_{2.85}Pr_{0.15}Ni₂O₇/SrLaAlO₄ samples, all exhibiting superconducting transitions and thus demonstrating the

reproducibility. Nevertheless, achieving a stable zero-resistance state remains challenging, suggesting that further optimization of film quality is required.

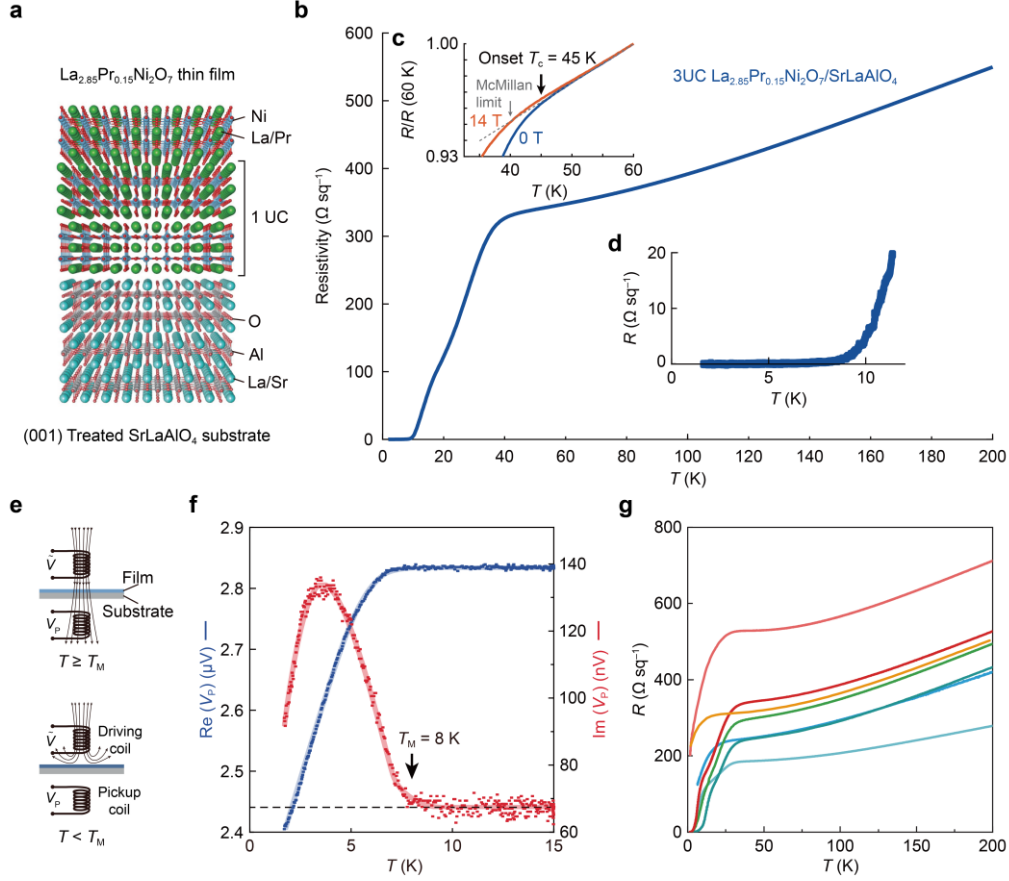


Figure 3-2 Ambient-pressure superconductivity in (La,Pr)₃Ni₂O₇ thin films. (a) Schematic illustration of the crystal structure. (b) Temperature-dependent sheet resistivity (R_s) curve of a representative 3UC La_{2.85}Pr_{0.15}Ni₂O₇ film on SrLaAlO₄. Resistance (R) was measured using a Hall bar geometry with current and voltage channel widths of 5 mm and 1.5 mm, respectively. The sheet resistivity was derived using the geometric factor $R_s = R \times (5/1.5)$. For thickness normalization, the 3UC film thickness was determined to be approximately 6.6 nm via X-ray reflectivity (XRR) analysis. (c) Magnified view of the R – T curve near the superconducting onset. Blue and orange curves represent data under perpendicular magnetic fields of 0 T and 14 T, respectively. The onset T_c is defined as the temperature where the R_s – T curve deviates from the linear fit from 50 to 60 K (grey dashed line). The McMillan limit (40 K) is indicated by the grey arrow. (d) Magnified view of the low-temperature R – T region, highlighting the approach to zero-resistance. (e) Schematic illustration of the two-coil mutual inductance setup. (f) Diamagnetic response of a 3UC La_{2.85}Pr_{0.15}Ni₂O₇ film. Blue and red symbols represent the real ($\text{Re}(V_p)$) and imaginary ($\text{Im}(V_p)$) components of the pickup coil voltage as a function of temperature, respectively. The Meissner temperature (T_M) is identified by the deviation of $\text{Im}(V_p)$ from its high-temperature horizontal baseline (dashed line). (g) R_s – T curves of multiple 3UC La_{2.85}Pr_{0.15}Ni₂O₇/SrLaAlO₄ samples. The variability between samples stems from differences in cation stoichiometry during synthesis or varying oxygen content resulting from different post-annealing conditions.

3.2 Thin-Film Growth and Structural Characterization of La_{2.85}Pr_{0.15}Ni₂O₇ on SrLaAlO₄ Substrates

La_{2.85}Pr_{0.15}Ni₂O₇ thin films were synthesized using the GAE methodology by alternately ablating NiO_x and La_{0.95}Pr_{0.05}O_y targets, following the stacking sequence of bilayer RP nickelates. The NiO_x target was prepared by sintering NiO powder at 1100 °C for 6 hours. The La_{0.95}Pr_{0.05}O_y binary target was synthesized from a stoichiometric mixture of La₂O₃ and Pr₆O₁₁ powders, subjected to two cycles of grinding and sintering at 1100 °C for 6 hours to ensure chemical homogeneity. Film growth was conducted at a substrate temperature of 750 °C under a mixed O₂/O₃ atmosphere, with partial pressures of 3 Pa and 7 Pa, respectively. The laser fluence ranged from 1.4 to 1.8 J·cm⁻² with a repetition rate of 4 Hz. Following deposition, samples were cooled at a rate of 100 °C/min to improve the experimental efficiency.

Precise cation stoichiometry was achieved by determining the pulse counts required for full monolayer coverage from each target. Following the two-step calibration protocol established in Chapter 2, the optimal pulse counts for NiO_x and La_{0.95}Pr_{0.05}O_y targets can be obtained for bilayer nickelate films grown on as-received LaAlO₃ substrates. These pulse parameters can then be transferred to SrLaAlO₄ (SLAO) substrates, provided that the SLAO substrate is properly treated in advance to reduce interfacial defects ^[109]. The (001)-oriented SLAO substrates were purchased from MTI (China). Prior to growth, the substrates were treated by placing a LaAlO₃ substrate face to face with a SLAO substrate, followed by annealing at 1030 °C or 1080 °C for 2 hours in air, similar to previous reports ^[110]. Figure 3-3a presents the atomic force microscopy (AFM) images of the SLAO surfaces after annealing at 1030 °C (left) and 1080 °C (right), respectively. The SLAO annealed at the higher temperature exhibits more well-defined terrace edges, wider terraces and reduced roughness (with a root-mean-square roughness of 439.6 pm), indicating a more favorable surface for the growth of high-quality films. The AFM image of the La_{2.85}Pr_{0.15}Ni₂O₇ film grown on the SLAO substrate annealed at 1080 °C is shown in Figure 3-3b. The film surface also displays a clear step-and-terrace morphology.

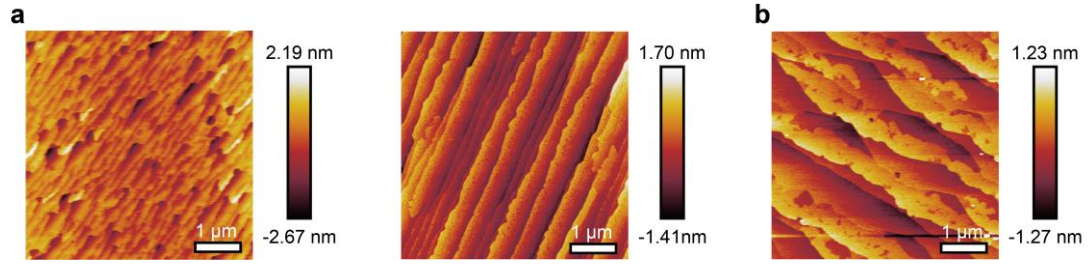


Figure 3-3 Surface morphology characterized by atomic force microscope (AFM). (a) AFM images of SrLaAlO₄ substrates annealed at 1030 °C (left) and 1080 °C (right). The root-mean-square (rms) roughness values are 536.6 pm and 439.6 pm, respectively. (b) AFM image of a La_{2.85}Pr_{0.15}Ni₂O₇ film grown on the SrLaAlO₄ substrate annealed at 1080 °C. The rms roughness is 407.3 pm.

Figure 3-4 presents the scanning transmission electron microscopy (STEM) image and the atomically resolved energy-dispersive X-ray spectroscopy (EDS) map of a 3UC La_{2.85}Pr_{0.15}Ni₂O₇ film grown on a SrLaAlO₄ substrate. No impurity phases are observed within the large-field-of-view STEM image (Figure 3-4a), indicating high crystalline quality. EDS mapping (Figure 3-4b) confirms the characteristic alternating stacking of bilayer NiO₂ planes. In addition, the epitaxial strain is maintained throughout the 3UC thickness without relaxation.

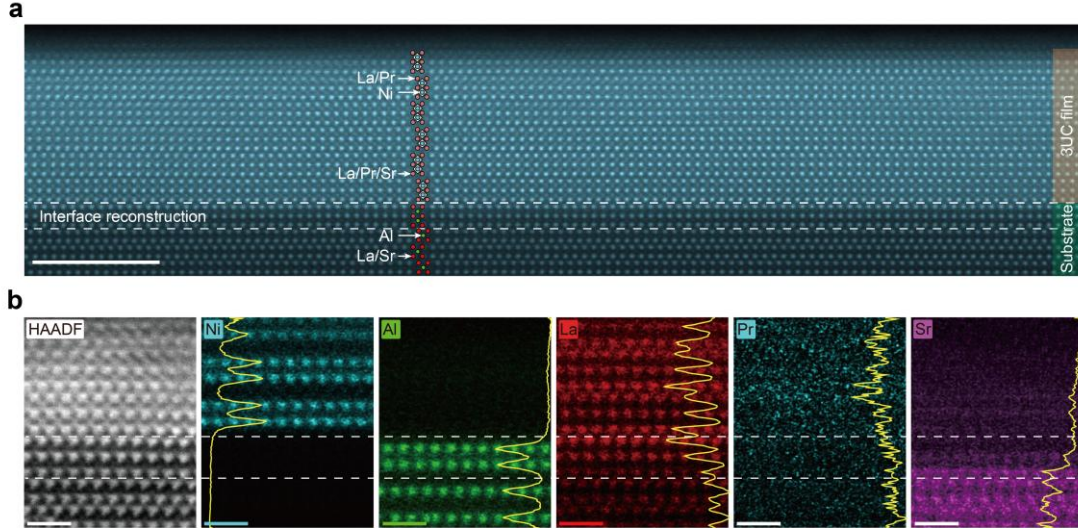


Figure 3-4 STEM and EDS characterization of superconducting La_{2.85}Pr_{0.15}Ni₂O₇ thin films. (a) High-angle annular dark-field (HAADF) STEM image of a 3UC La_{2.85}Pr_{0.15}Ni₂O₇ film on an SrLaAlO₄ substrate. Boundaries between the film, interfacial reconstruction layer and substrate are indicated by white dashed lines. (b) Atomically resolved EDS maps of Ni, Al, La, Pr and Sr elements for the La_{2.85}Pr_{0.15}Ni₂O₇/SrLaAlO₄ heterostructure. The SLAO substrate was pre-annealed prior to film growth. The yellow curves represent the intensity profiles obtained by horizontal integration across the mapped area. Scale bars: 5 nm for (a) and 1 nm for (b).

Notably, the SLAO substrate undergoes a structural reconstruction, probably during the pre-annealing process, forming a (La,Sr)₃Al₂O₇ bilayer structure at the interface. This reconstructed bilayer buffer serves as a structural template that facilitates the defect-free, layer-by-layer epitaxy of the subsequent nickelate layers ^[109].

3.3 Role of Ozone Annealing and Pr Doping

As emphasized in Chapter 1, oxygen vacancies in bulk La₃Ni₂O_{7- δ} , particularly those at the inner apical sites, not only strongly affect the normal-state transport properties but are also detrimental to superconductivity^[52,68]. The implementation of a highly oxidizing growth environment (10 Pa total pressure with nearly pure ozone), as discussed in Chapter 2, successfully lowered the resistivity by suppressing oxygen vacancies in bilayer nickelate thin films. This experience underscores the importance of sufficient oxygen supply for optimizing oxygen stoichiometry. In addition to growth optimization, post-annealing in an ozone-rich environment is found to be highly effective in further eliminating oxygen vacancies and inducing superconductivity in bilayer nickelate thin films, as shown in Figure 3-5a and 3-5b.

The post-annealing process was carried out by heating the as-grown samples at 575 °C in the growth chamber for 30 mins, while continuously supplying purified ozone (roughly 15 Pa) through a nozzle directed onto the heated sample. After annealing, the samples were cooled at a rate of 100 °C/min in the same oxidizing atmosphere to below at least 100 °C before being transferred from the growth chamber to the load-lock chamber, in order to minimize oxygen loss. Immediately after transfer, the load-lock chamber was vented with oxygen for the same purpose. The annealed samples were then taken out, and aluminum wires were promptly bonded onto the Hall-bar electrodes (previously deposited by magnetron sputtering) using an ultrasonic wire bonder. The samples were subsequently loaded into a Physical Property Measurement System (PPMS, Quantum Design) for transport measurements.

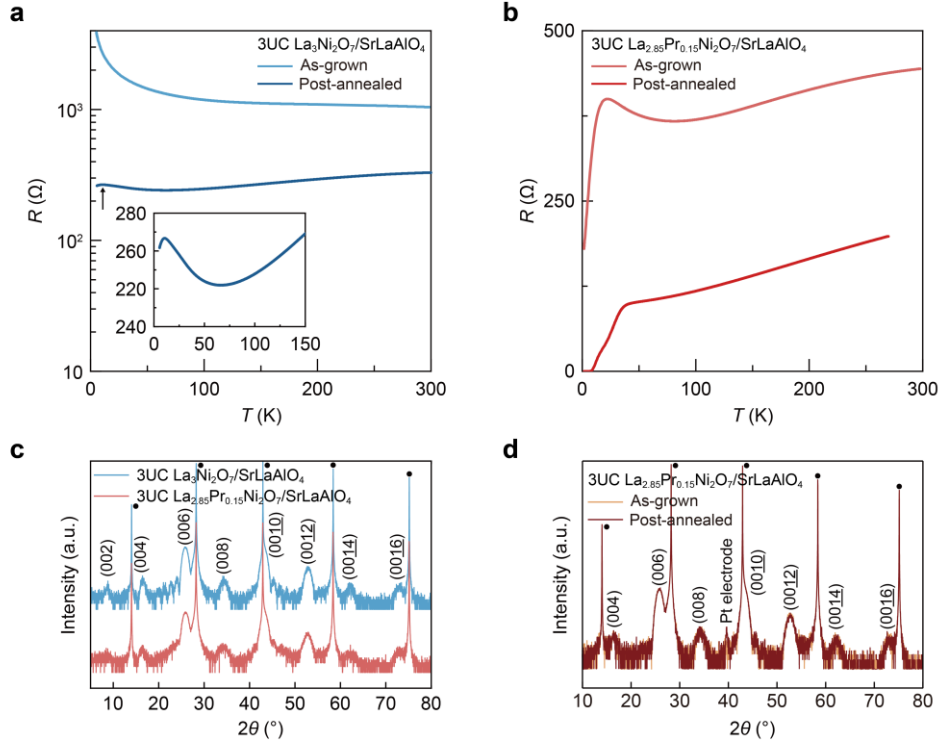


Figure 3-5 Role of ozone annealing and Pr doping. (a) Temperature-dependent resistance (R - T) curves of a 3UC La₃Ni₂O₇/SrLaAlO₄ sample before (light blue) and after (dark blue) post-annealing. The inset shows the enlarged view of the post-annealed curve, highlighting a small resistance drop. (b) R - T curves of a 3UC La_{2.85}Pr_{0.15}Ni₂O₇/SrLaAlO₄ sample before (light red) and after (dark red) post-annealing. The two samples have identical thickness and Hall-bar geometry, allowing direct comparison of resistance. (c) XRD patterns of the same as-grown La₃Ni₂O₇/SrLaAlO₄ (light blue) and La_{2.85}Pr_{0.15}Ni₂O₇/SrLaAlO₄ (light red) samples shown in (a) and (b). Peaks from the SLAO substrate are marked by black solid circles. (d) XRD patterns of another 3UC La_{2.85}Pr_{0.15}Ni₂O₇/SrLaAlO₄ sample before (yellow) and after (brown) post-annealing. The post-annealed sample shows additional diffraction peak from the Pt electrodes deposited after film growth for transport measurements.

After undergoing this post-annealing process, both La₃Ni₂O₇ (Figure 3-5a) and La_{2.85}Pr_{0.15}Ni₂O₇ (Figure 3-5b) exhibited a pronounced reduction in resistance compared to their as-grown states. In addition, the La₃Ni₂O₇ sample transitioned from insulating behavior to metallic behavior at high temperatures. After a slight resistance upturn near 65 K, a superconducting-like drop appeared at approximately 10 K. This demonstrates the critical role of ozone annealing in inducing superconductivity through the suppression of oxygen vacancies and reduction of normal-state resistance.

In contrast, the as-grown La_{2.85}Pr_{0.15}Ni₂O₇ sample exhibited a lower room-

temperature resistance ($R_{300\text{ K}} = 445\ \Omega$) compared to the as-grown La₃Ni₂O₇ sample ($R_{300\text{ K}} = 1043\ \Omega$), and already possessed a noticeable resistance drop at 22 K after undergoing a metal-insulator-superconductor transition. After post-annealing, the superconducting onset temperature exceeded 40 K, accompanied by the achievement of zero resistance.

Since both undoped and Pr-doped samples were grown under identical thermodynamic conditions (grown temperature of 750 °C and an oxidizing environment of 10 Pa O₂/O₃ mixture with 3 Pa O₃), the significant reduction in the room-temperature resistance in the Pr-doped sample can be attributed to the slight isovalent substitution of La by Pr (5%). This substitution effectively suppresses the formation of oxygen vacancies during thin film growth, and facilitates oxygen incorporation during post-annealing.

Previous studies on pressurized bulk La₂PrNi₂O₇ suggest that Pr doping suppresses the intergrowth of other RP phases and improve bilayer phase purity, thereby enhancing the superconducting performance [59]. However, the present comparison suggests an additional mechanism that Pr doping can also effectively suppress oxygen deficiency. This is supported by the observation that the XRD quality of La_{2.85}Pr_{0.15}Ni₂O₇ is not superior to that of La₃Ni₂O₇ (likely due to less optimized cation stoichiometry), as shown in Figure 3-5c. This enhanced oxygen incorporation associated with Pr doping is also consistent with the tendency toward over-oxidization in La₂PrNi₂O_{7+δ} samples under high-pressure oxygen annealing [67].

Figure 3-5d compares the XRD patterns of a La_{2.85}Pr_{0.15}Ni₂O₇ sample before and after post-annealing. No significant changes in peak position or intensity are observed, indicating that the annealing process does not degrade the structural quality. This also suggests that the oxygen vacancy concentration in the as-grown film is not sufficiently large to induce detectable lattice distortion in XRD. Nevertheless, the removal of even a small amount of oxygen vacancies plays a crucial role in inducing or enhancing superconductivity.

In summary, ozone post-annealing and Pr doping act synergistically to suppress oxygen vacancies and improve the superconducting performance of bilayer nickelates.

3.4 Magnetotransport Properties

The La_{2.85}Pr_{0.15}Ni₂O₇ thin film exhibits a pronounced anisotropy in its response to out-of-plane and in-plane magnetic fields, as shown in Figure 3-6a and 3-6b. The superconducting transition undergoes a weaker suppression under in-plane fields compared to out-of-plane fields, suggesting a more robust superconductivity within the NiO₂ planes. To quantify this anisotropy, the out-of-plane ($B_{c,\perp}$) and in-plane ($B_{c,\parallel}$) critical fields are extracted using both $T_{c,90\%}$ and $T_{c,50\%}$, defined as the temperatures where the resistance drops to 90% and 50% of the normal-state resistance (R_N), respectively (Figure 3-6c). $B_{c,\perp}$ displays a linear temperature dependence, while $B_{c,\parallel}$ follows a square-root dependence. The data were fitted using the two-dimensional (2D) Ginzburg–Landau formulas ^[111]:

$$B_{c,\perp}(T) = \frac{\Phi_0}{2\pi\xi_{ab}^2(0)} \left(1 - \frac{T}{T_c}\right) \quad (3-1)$$

$$B_{c,\parallel}(T) = \frac{\sqrt{12}\Phi_0}{2\pi\xi_{ab}(0)d} \left(1 - \frac{T}{T_c}\right)^{\frac{1}{2}}, \quad (3-2)$$

where Φ_0 is the magnetic flux quantum, $\xi_{ab}(0)$ is the in-plane Ginzburg–Landau coherence length at zero temperature, and d is the superconducting thickness.

The linear fits for $B_{c,\perp}$ yield out-of-plane zero-temperature critical fields $B_{c0,\perp}$ of 68 T and 29 T, for the 90% and 50% criteria, respectively. Correspondingly, the in-plane fits result in $B_{c0,\parallel}$ of 119 T and 71 T. Taking $B_{c,90\%}$ as the upper critical fields B_{c2} associated with pair breaking, the coherence length is estimated using $\xi_0 = \sqrt{(\Phi_0/2\pi B_{c2})}$, yielding an in-plane coherence length $\xi_{0\parallel} = 2.2$ nm and an out-of-plane coherence length $\xi_{0\perp} = 1.7$ nm. The superconducting thickness d is estimated as $d = \sqrt{(6\Phi_0 B_{c,\perp}/\pi B_{c,\parallel}^2)} = 4 \pm 3$ nm, which is on the same order as the film thickness. Notably, the extrapolated in-plane upper critical field $B_{c2,\parallel}(0)$ reaches approximately 119 T, which exceeds the conventional Pauli limit estimated by $B_P = 1.84 T_c = 82.8$ T where $T_c = 45$ K. However, since the fitting is based on measurements performed under magnetic fields up to only 14 T, the extrapolated value may be overestimated due to the limited field range. Further high-field measurements are therefore required to determine the intrinsic upper critical field more reliably.

Figure 3-6d shows the angular dependence of the critical temperature $T_{c,50\%}$,

measured by rotating the sample by an angle β relative to the film plane under a constant magnetic field of 14 T. The $T_{c,50\%}$ – β dependence is well captured by the Tinkham model for 2D superconductors, while the anisotropic three-dimensional (3D) Ginzburg–Landau model fails to reproduce the pronounced cusp near zero angle ^[112]. This further supports the quasi-2D nature of superconductivity in La_{2.85}Pr_{0.15}Ni₂O₇ thin films.

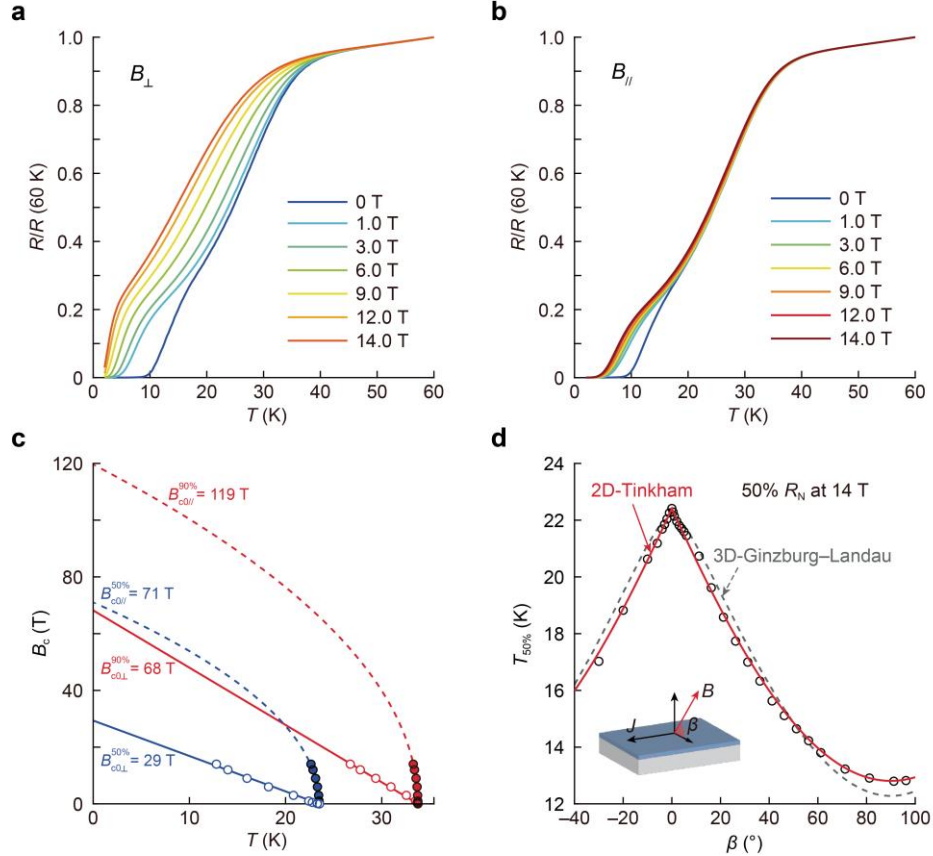


Figure 3-6 Magnetotransport properties of the La_{2.85}Pr_{0.15}Ni₂O₇ thin film. (a, b) Temperature-dependent resistance curves measured under magnetic fields applied perpendicular (a) and parallel (b) to the film plane. Resistance is normalized to its value at 60 K. (c) Temperature-dependent out-of-plane (open circles) and in-plane (solid circles) critical magnetic fields. Critical fields are extracted using both $T_{c,90\%}$ (red) and $T_{c,50\%}$ (blue), which correspond to the temperatures at which the resistance drops to 90% and 50% of the normal-state resistance R_N , respectively. Solid lines represent linear fits, while dashed curves correspond to fits using the Ginzburg–Landau model. (d) Angular dependence of the critical temperature $T_{50\%}$ under an applied magnetic field of 14 T. The inset illustrates the measurement geometry, where β is the angle between the magnetic field and the film plane. Open circles represent experimental data. The red solid curve and grey dashed curve represent fits using the two-dimensional Tinkham model and the three-dimensional Ginzburg–Landau model, respectively.

3.5 Thermal Instability

Despite the high-quality growth and robust superconductivity discussed above, the La_{2.85}Pr_{0.15}Ni₂O₇ thin films face challenges regarding long-term stability. They exhibit a gradual increase in resistance when maintained in a vacuum environment in PPMS at temperatures above 200 K (Figure 3-7). A similar resistance is also observed under ambient conditions at room temperature. This behavior degrades the superconducting performance of the films, and is attributed to oxygen loss.

The pronounced thermal instability of bilayer nickelate thin films, particularly under elevated temperatures or high-vacuum conditions imposes stringent requirements on sample preservation and long-distance transport of samples for further characterization, such as angle-resolved photoemission spectroscopy (ARPES) measurements at synchrotron facilities. Therefore, cold-chain transportation under high-vacuum conditions is essential to prevent oxygen loss and to protect the sample surface from gas adsorption. Such precautions are crucial for probing the intrinsic electronic properties of ambient-pressure superconducting bilayer RP nickelates using ARPES.

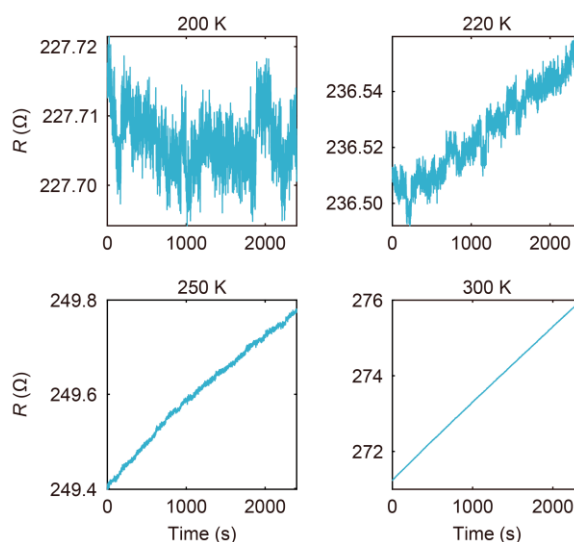


Figure 3-7 Oxygen loss in La_{2.85}Pr_{0.15}Ni₂O₇ thin films. Time-dependent resistance of a La_{2.85}Pr_{0.15}Ni₂O₇ thin film measured in the vacuum environment of the PPMS at temperatures of 200 K, 220 K, 250 K and 300 K.

3.6 Summary and Conclusions

This chapter reports the realization of ambient-pressure superconductivity in bilayer Ruddlesden–Popper (RP) nickelates, stabilized by epitaxial compressive strain from SrLaAlO₄ (SLAO) substrates. High-quality 3UC La_{2.85}Pr_{0.15}Ni₂O₇ thin films were grown on treated SLAO substrates using the GAE method, followed by ozone post-annealing. The representative sample exhibits a superconducting onset temperature $T_{c,\text{onset}} = 45$ K, notably exceeding the McMillan limit. Superconductivity is confirmed by the observation of both zero resistance and the Meissner diamagnetic effect.

Both ozone post-annealing and partial substitution of La with Pr are found to effectively suppress oxygen vacancies and significantly enhance the superconducting performance. Magnetotransport measurements reveal a pronounced anisotropic response to magnetic fields. In addition, the susceptibility of bilayer nickelates to oxygen loss at elevated temperatures highlights their thermal instability, necessitating a cold-chain transportation to preserve intrinsic properties for subsequent spectroscopic measurements such as ARPES.

Parallel to this work, independent studies have also reported signatures of superconductivity in La₃Ni₂O₇ thin films ^[97], supporting the robustness of ambient-pressure superconductivity in bilayer RP nickelates. These advances not only pave the way for ongoing spectroscopic investigations to uncover the electronic features responsible for high- T_c superconductivity in these systems, but also provides a promising route toward realizing ambient-pressure superconductivity in other RP nickelates including trilayer and hybrid phases.

CHAPTER 4 SUPERCONDUCTIVITY AND ELECTRONIC STRUCTURES OF NICKELATE THIN FILM SUPERSTRUCTURES

The realization of ambient-pressure superconductivity in bilayer Ruddlesden–Popper (RP) nickelate films ^[97,108,113–115] enables direct probing of the electronic band structure underlying the superconducting state using angle-resolved photoemission spectroscopy (ARPES). Figure 4-1 summarizes three ARPES measurements on (La,Pr)₃Ni₂O₇ or (La,Sr)₃Ni₂O₇ films grown on SrLaAlO₄ substrates ^[116–118].

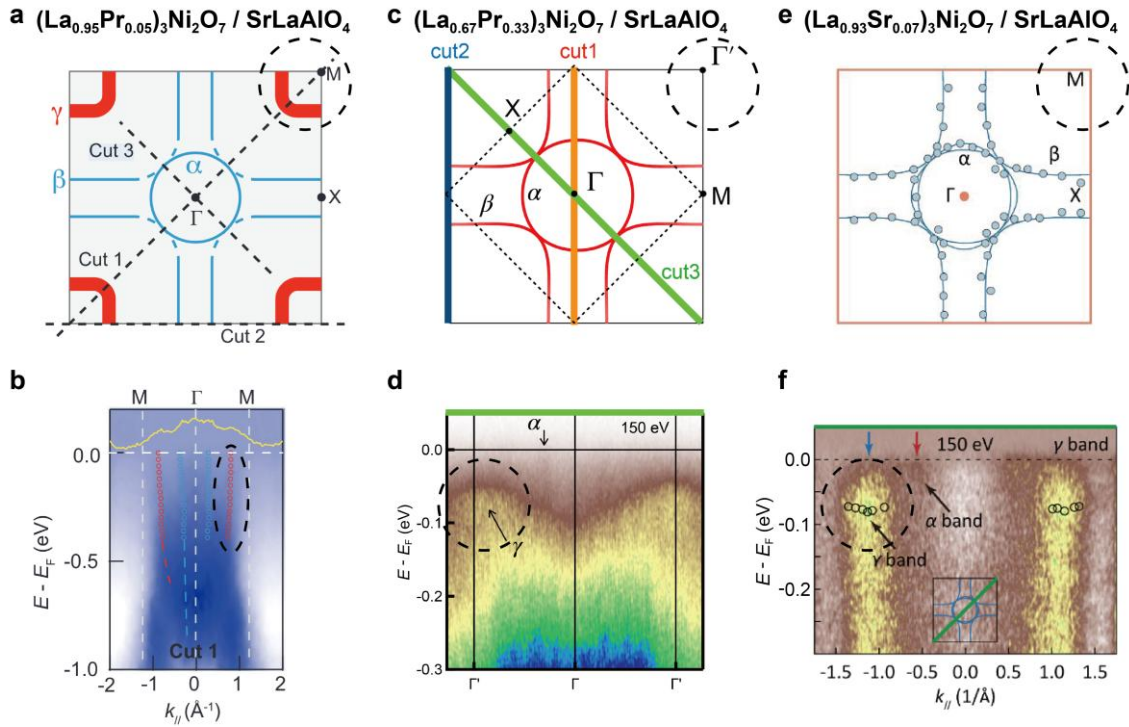


Figure 4-1 ARPES measurements of ambient-pressure superconducting bilayer nickelate thin films. (a) Schematic Fermi surface map of $(\text{La}_{0.95}\text{Pr}_{0.05})_3\text{Ni}_2\text{O}_7$ films grown on SrLaAlO₄ substrates based on ARPES measurements ^[116]. The γ band is highlighted by the dashed circle. (b) ARPES spectral cut along the M– Γ –M direction ^[116]. The yellow curve shows the momentum distribution curve (MDC) at the Fermi level. Blue and red open circles denote fitted peak positions from MDCs. The dispersion of the γ band is highlighted by the dashed circle. (c, d) Corresponding ARPES-derived schematic Fermi surface map and spectral cut for $(\text{La}_{0.67}\text{Pr}_{0.33})_3\text{Ni}_2\text{O}_7/\text{SrLaAlO}_4$ samples ^[117]. (e, f) Corresponding ARPES-derived schematic Fermi surface map and spectral cut for $(\text{La}_{0.93}\text{Sr}_{0.07})_3\text{Ni}_2\text{O}_7/\text{SrLaAlO}_4$ samples ^[118]. The absence of the γ band at the Fermi surface and its position below the Fermi level are highlighted by dashed circles.

All three measurements reveal a Fermi surface consisting of an electron-like pocket (α band) at the Brillouin zone (BZ) center, and a large hole-like β pocket around the BZ corner. Both bands primarily originate from Ni $d_{x^2-y^2}$ orbitals. However, a significant discrepancy persists regarding the presence of the Ni d_{z^2} -derived γ band at the Fermi level. Results for $(\text{La}_{0.95}\text{Pr}_{0.05})_3\text{Ni}_2\text{O}_7$ samples (Figure 4-1a and 4-1b) indicate that the γ band crosses the Fermi level ^[116], whereas measurements on $(\text{La}_{0.67}\text{Pr}_{0.33})_3\text{Ni}_2\text{O}_7$ (Figures 4-1c and 4-1d) and $(\text{La}_{0.93}\text{Sr}_{0.07})_3\text{Ni}_2\text{O}_7$ (Figures 4-1e and 4-1f) report that the γ band lies approximately 70–75 meV below the Fermi level ^[117,118]. These discrepancies may arise from differences in dopant species and doping levels, variations in oxygen stoichiometry, or possible contributions from intergrowths of other RP phases, given the thermodynamic metastability and sensitivity to oxygen off-stoichiometry of bilayer RP nickelates. In addition to the experimental controversy regarding the exact Fermi surface topology, the role of the γ band in the emergence of high-temperature superconductivity remains under active theoretical debate ^[8,54,55]. Therefore, more systematic and rigorous investigations are required to establish whether the γ band contributes to the Fermi surface of superconducting bilayer RP nickelates.

High-temperature superconductivity has also been reported in pressurized hybrid nickelates such as the 1212 phase ($\text{La}_5\text{Ni}_3\text{O}_{11}$, a hybrid of La_2NiO_4 and $\text{La}_3\text{Ni}_2\text{O}_7$ blocks) ^[83] and the 1313 phase ($\text{La}_3\text{Ni}_2\text{O}_7$, a hybrid of La_2NiO_4 and $\text{La}_4\text{Ni}_3\text{O}_{10}$ blocks) ^[86], while theoretical studies have proposed the 2323 phase ($\text{La}_7\text{Ni}_5\text{O}_{17}$, a hybrid of $\text{La}_3\text{Ni}_2\text{O}_7$ and $\text{La}_4\text{Ni}_3\text{O}_{10}$ blocks) as another promising candidate ^[119]. These results identify hybrid nickelates as a promising platform for comparative studies aimed at elucidating the shared origins of superconductivity across different RP-based structures.

This chapter reports the realization of ambient-pressure superconductivity in epitaxial thin films with monolayer–bilayer (1212, $(\text{La,Pr})_5\text{Ni}_3\text{O}_{11}$) and bilayer–trilayer (2323, $(\text{La,Pr})_7\text{Ni}_5\text{O}_{17}$) hybrid superstructures, together with the absence of superconductivity in monolayer–trilayer phase (1313, $(\text{La,Pr})_3\text{Ni}_2\text{O}_7$) under identical compressive strain. These hybrid superstructures, along with the pure bilayer nickelate (2222, $(\text{La,Pr})_3\text{Ni}_2\text{O}_7$), are systematically compared in

terms of their low-temperature transport properties, structural characteristics, magnetic responses and ARPES spectra.

4.1 Comparison of Various Superstructures

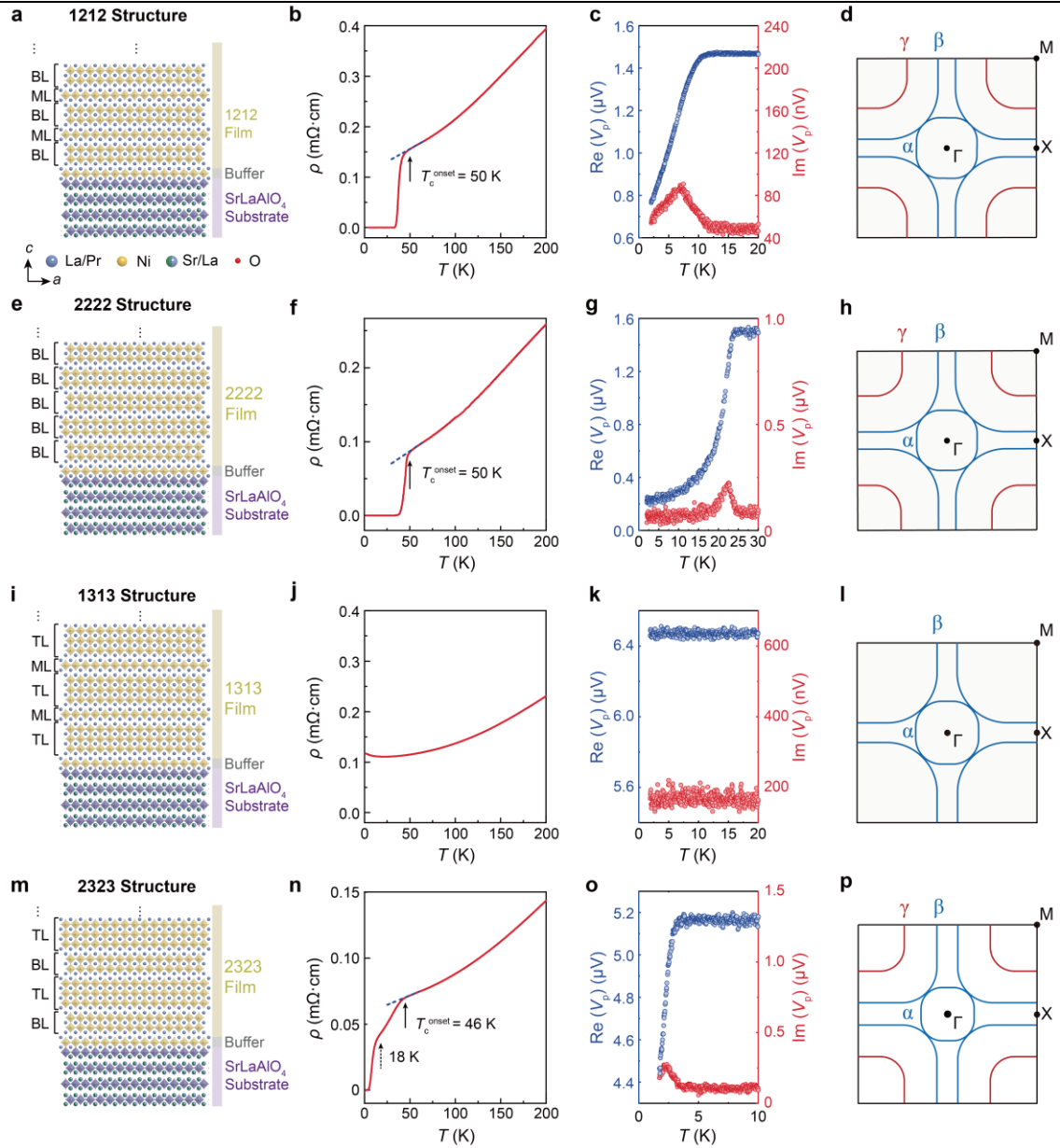
Figure 4-2 summarizes a comparative study of 1212, 2222, 1313 and 2323 nickelate thin films grown on SrLaAlO_4 substrates. Figures 4-2a, 4-2e, 4-2i and 4-2m present schematic illustrations of their crystal structures. These superstructures consist of alternating stackings of two different RP phases, constructed by pairing any two of the monolayer (ML), bilayer (BL) and trilayer (TL) units.

One-third of the La sites are substituted by Pr, as higher Pr doping levels have been demonstrated to effectively suppress oxygen vacancies and enhance superconducting performance^[59,113]. This substitution enables sufficient oxidizing capability and allows optimal oxygen stoichiometry to be achieved by tuning ozone concentration or temperature alone, without the need for post-annealing.

The observation of both zero resistance and the Meissner effect in the 1212, 2222 and 2323 superstructures confirms their superconducting nature, as evidenced by temperature-dependent resistivity (ρ - T) curves and diamagnetic responses. In contrast, the 1313 film displays metallic behavior with a slight resistivity upturn appearing below 23 K. Figure 4-3 presents the ρ - T curves of three representative samples for each superstructure, demonstrating high robustness and reproducibility. The maximum superconducting onset temperatures ($T_{c,\text{onset}}$) for the 1212, 2222 and 2323 superstructures are 50 K, 55 K and 46 K, respectively, all exceeding the McMillan limit (40 K). The corresponding maximum zero-resistance temperatures ($T_{c,0}$) are 30 K, 25 K and 3.5 K.

The schematic Fermi surfaces for the four superstructures, derived from ARPES measurements, are shown in Figures 4-2d, 4-2h, 4-2l and 4-2p. For the superconducting 1212, 2222 and 2323 systems, the Fermi surface consistently consists of an electron-like α pocket at the BZ center (Γ), a hole-like β pocket around the zone corner (M), and notably, a prominent hole-like γ pocket surrounding the M point. In contrast, the Fermi surface of the non-superconducting 1313 superstructure contains only the α and β pockets, with the γ pocket absent. Detailed ARPES data will be presented later.

CHAPTER 4 SUPERCONDUCTIVITY AND ELECTRONIC STRUCTURES OF NICKELATE THIN FILM SUPERSTRUCTURES



CHAPTER 4 SUPERCONDUCTIVITY AND ELECTRONIC STRUCTURES OF NICKELATE THIN FILM SUPERSTRUCTURES

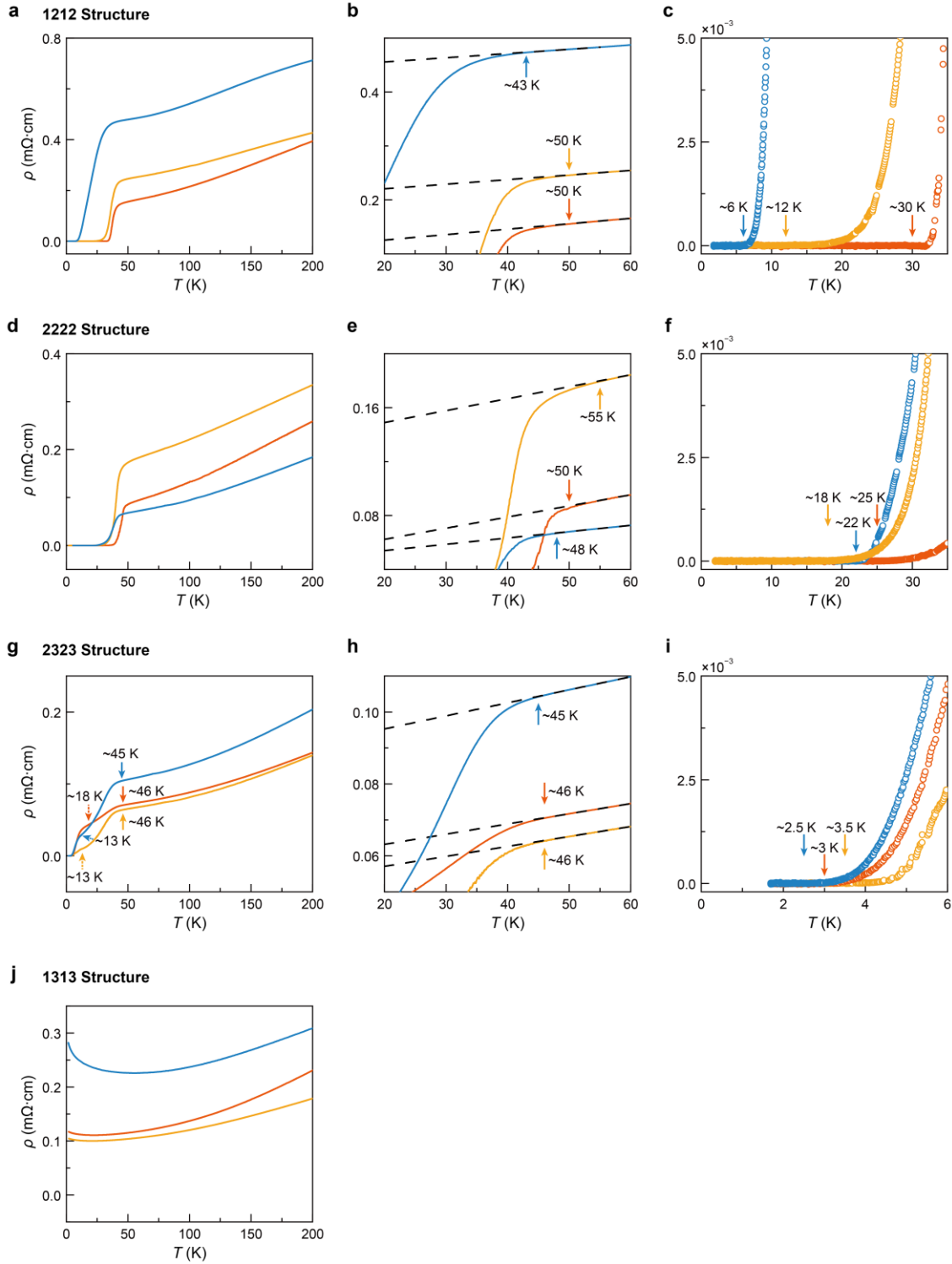


Figure 4-3 Representative ρ - T curves. (a-c) ρ - T curves of three representative 1212 films, and enlarged views near the $T_{c,onset}$ and $T_{c,0}$ regions. Dashed black lines represent linear fits to the normal-state resistivity. (d-f) Corresponding ρ - T curves for 2222 films. (g-i) Corresponding ρ - T curves for 2323 films. $T_{c,onset}$ and the second onset temperature ($T_{c,2nd\ onset}$) are indicated by solid and dashed arrows in (g), respectively. $T_{c,2nd\ onset}$ is defined as the temperature at which the temperature derivative of resistivity (dp/dT) exhibits a second rise upon cooling. (j) ρ - T curves of three representative 1313 films.

4.2 Thin-Film Growth and Structural Characterization of Nickelate Superstructures

All samples were prepared on as-received SrLaAlO₄ (001) substrates (MTI-Kejing), using the GAE method ^[94]. During growth, NiO_x and La_{0.67}Pr_{0.33}O_y targets were alternately ablated. The ablation sequences for the 1212 and 1313 superstructures followed the stacking order of their corresponding crystal structures. For example, the growth sequence of the 1212 superstructure was [(La,Pr)O–NiO₂–(La,Pr)O]–[(La,Pr)O–NiO₂–(La,Pr)O–NiO₂–(La,Pr)O]. For the growth of the 2222 and 2323 structures, a buffer layer with the sequence (La,Pr)O–NiO₂–(La,Pr)O was first deposited to mitigate interfacial defects and stabilize the layered architecture during subsequent deposition ^[120].

The reflective high-energy electron diffraction (RHEED) oscillations patterns shown in Figure 4-4 provide detailed insight into the deposition sequence for each superstructure. The RHEED intensity increases during ablation of the NiO_x targets and decreases when the La_{0.67}Pr_{0.33}O_y target is deposited. This behavior differs from conventional unit-cell-by-unit-cell growth using a single target where the RHEED intensity undergoes a full oscillation cycle (decline and rise), corresponding to the completion of one unit cell and not directly reflecting surface chemistry ^[93]. In contrast, the lay-by-layer epitaxy mode of GAE, terminates the sample surface with different chemical environments, depending on the ablated target. As a result, the rise and fall of the RHEED intensity can be correlated with the target being ablated, providing monitoring of the growth sequence.

The film stoichiometry was controlled by precisely tuning the number of laser pulses required to deposit a complete atomic layer. Calibration of the pulse numbers for both targets was performed by synthesizing 3UC (La,Pr)₃Ni₂O₇ films on SrLaAlO₄ substrates. The X-ray diffraction (XRD) patterns of the calibration sample exhibit at least the (004) diffraction peak, indicating the formation of a long-range bilayer phase. This ensures near-stoichiometric growth conditions when synthesizing more complex hybrid RP superstructures.

The La_{0.67}Pr_{0.33}O_y and NiO_x targets were synthesized from a stoichiometric mixture of Pr₆O₁₁/La₂O₃ powders, and NiO powder, respectively. The La_{0.67}Pr_{0.33}O_y target was sintered twice (6 h each) at 1100 °C, and the NiO_x target

was sintered once for 6 h at the same temperature. Film growth was carried out at temperatures between 760 °C and 850 °C under a mixed O₂/O₃ atmosphere. The total pressure was maintained at 10 Pa, with ozone partial pressures ranging from 1 Pa to 3 Pa. The laser fluence was set to 1.4–1.7 J·cm⁻², with a repetition rate of 4 Hz. After deposition, the samples were cooled at a rate of 100 °C/min to below 100 °C before being transferred to the load-lock chamber, in order to prevent oxygen loss.

Scanning transmission electron microscopy (STEM) combined with atomically resolved energy-dispersive X-ray spectroscopy (EDS) was employed to probe the microscopic structure of the 1212, 2222, 1313 and 2323 films grown on SrLaAlO₄ substrates (Figure 4-5). In high-angle annular dark-field (HAADF) STEM images (Figures 4-5a, d, g, j), the characteristic stacking sequences are clearly observed: monolayer/bilayer blocks in the 1212 phase, bilayer/bilayer blocks in the 2222 phase, monolayer/trilayer blocks in the 1313 phase and bilayer/trilayer blocks in the 2323 phase. Large-area HAADF images of phase-pure regions are presented in Figure 4-6. Corresponding EDS maps for Ni (Figures 4-5b, e, h, k) further highlight these stacking configurations.

Notably, growth of all four structures on as-received SrLaAlO₄ substrates begins with the same buffer layer, (La,Pr)O–NiO₂–(La,Pr)O. This leads to interfacial reconstruction and the formation of a (La,Pr,Sr)₃(Ni,Al)₂O₇ bilayer structure at the interface, which plays a role analogous to (La,Sr)₃Al₂O₇ in mitigating interfacial defects and facilitating high-quality epitaxy.

Out-of-plane XRD patterns are shown in Figures 4-5c, f, i and l. All films exhibit well-defined diffraction peaks without detectable impurity phases, confirming high crystalline quality at the macroscopic scale. The presence of Kiessig fringes around the primary peaks further indicates smooth surfaces and sharp interfaces. For the superconducting 1212 film grown on SrLaAlO₄ substrates, the c-axis lattice constant is determined to be 16.78 Å, corresponding to an approximately 1.2% elongation compared to the bulk value of 16.575 Å [83]. HAADF–STEM images reveal coherent in-plane strain throughout the thickness without relaxation, resulting in an in-plane compressive strain of approximately 2%, comparable to that observed in bilayer films. The extracted c-axis lattice constants

for the 2222, 1313 and 2323 films are 20.75 Å, 20.57 Å and 24.63 Å, respectively.

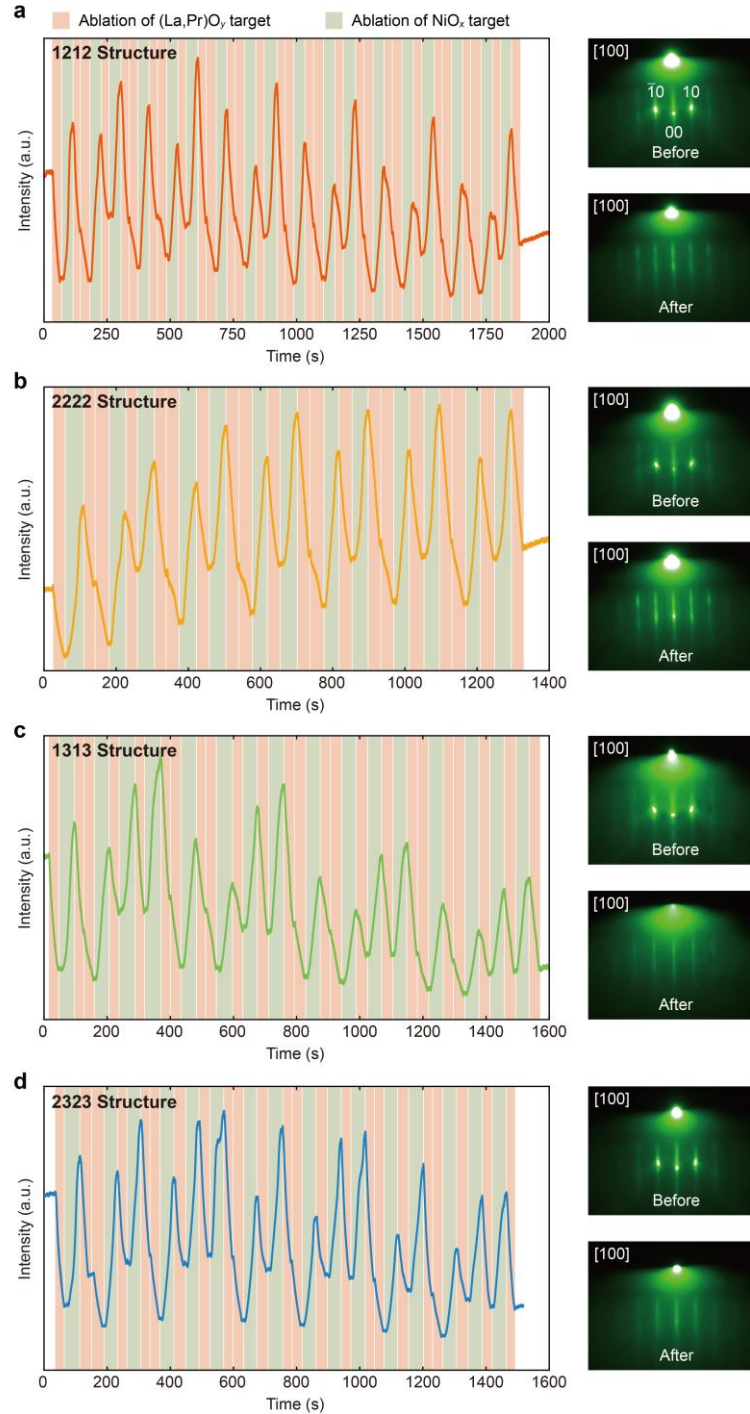


Figure 4-4 RHEED oscillations during thin-film growth. RHEED intensity oscillations and corresponding diffraction patterns recorded before and after the growth of 1212 (a), 2222 (b), 1313 (c) and 2323 (d) films. The oscillations reflect the layer-by-layer growth process, precisely matching the target stacking sequence. For example, one unit cell of the 1212 phase is deposited in the sequence: [(La,Pr)O–NiO₂–(La,Pr)O]–[(La,Pr)O–NiO₂–(La,Pr)O–NiO₂–(La,Pr)O–NiO₂–(La,Pr)O].

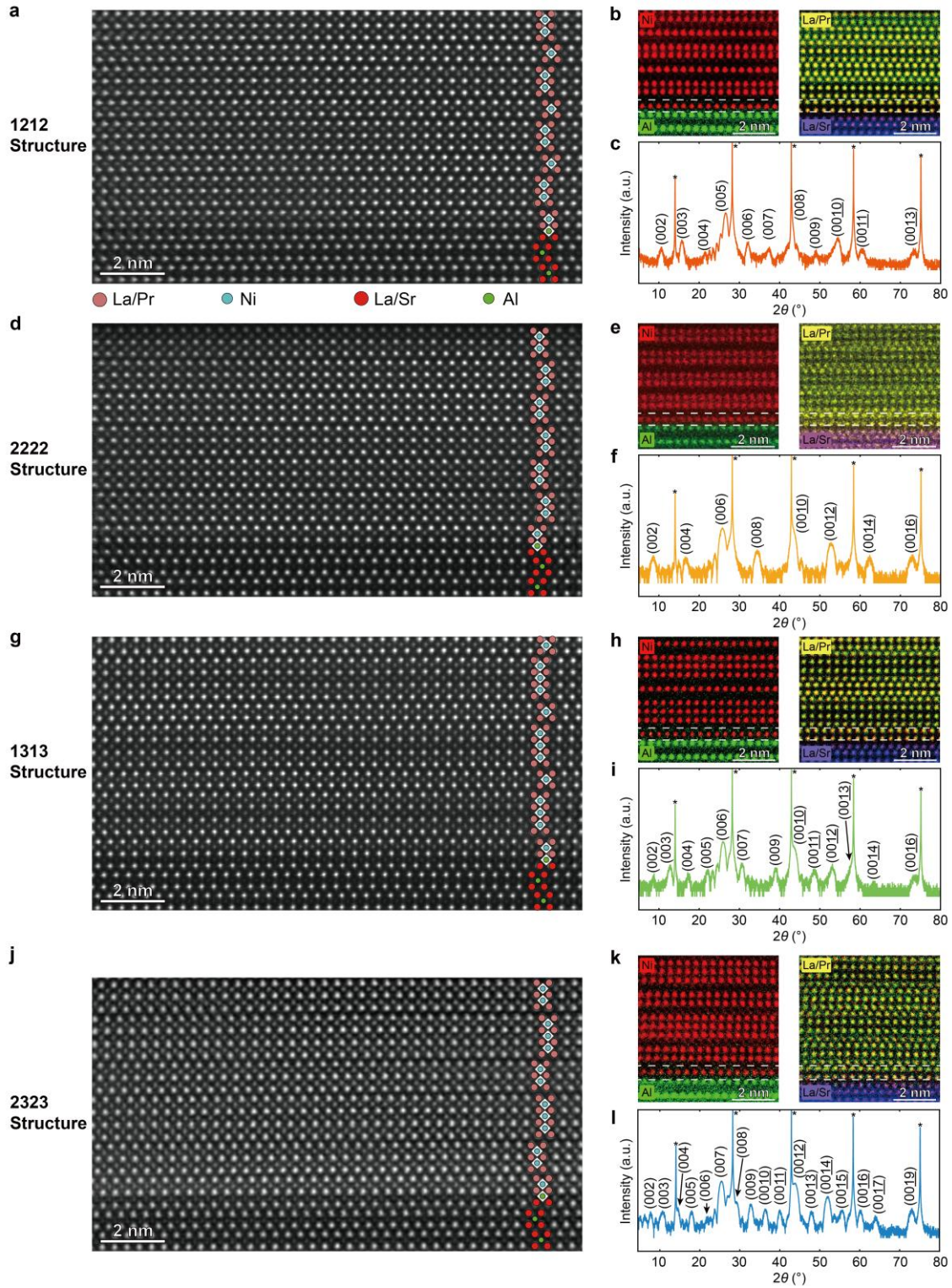


Figure 4-5 STEM and EDS characterizations of 1212, 2222, 1313 and 2323 nickelate thin films. (a) HAADF-STEM image of a 1212 film on SrLaAlO_4 . (b) Corresponding EDS elemental maps (Ni, Al, La, Pr and Sr), with white dashed lines marking the boundaries between the film, buffer layer and substrate. (c) Out-of-plane XRD pattern of a 6UC 1212 film on SrLaAlO_4 . HAADF images, EDS maps and XRD patterns for a 3UC 2222 film (d-f), a 4UC 1313 film (g-i) and a 3UC 2323 film (j-l).

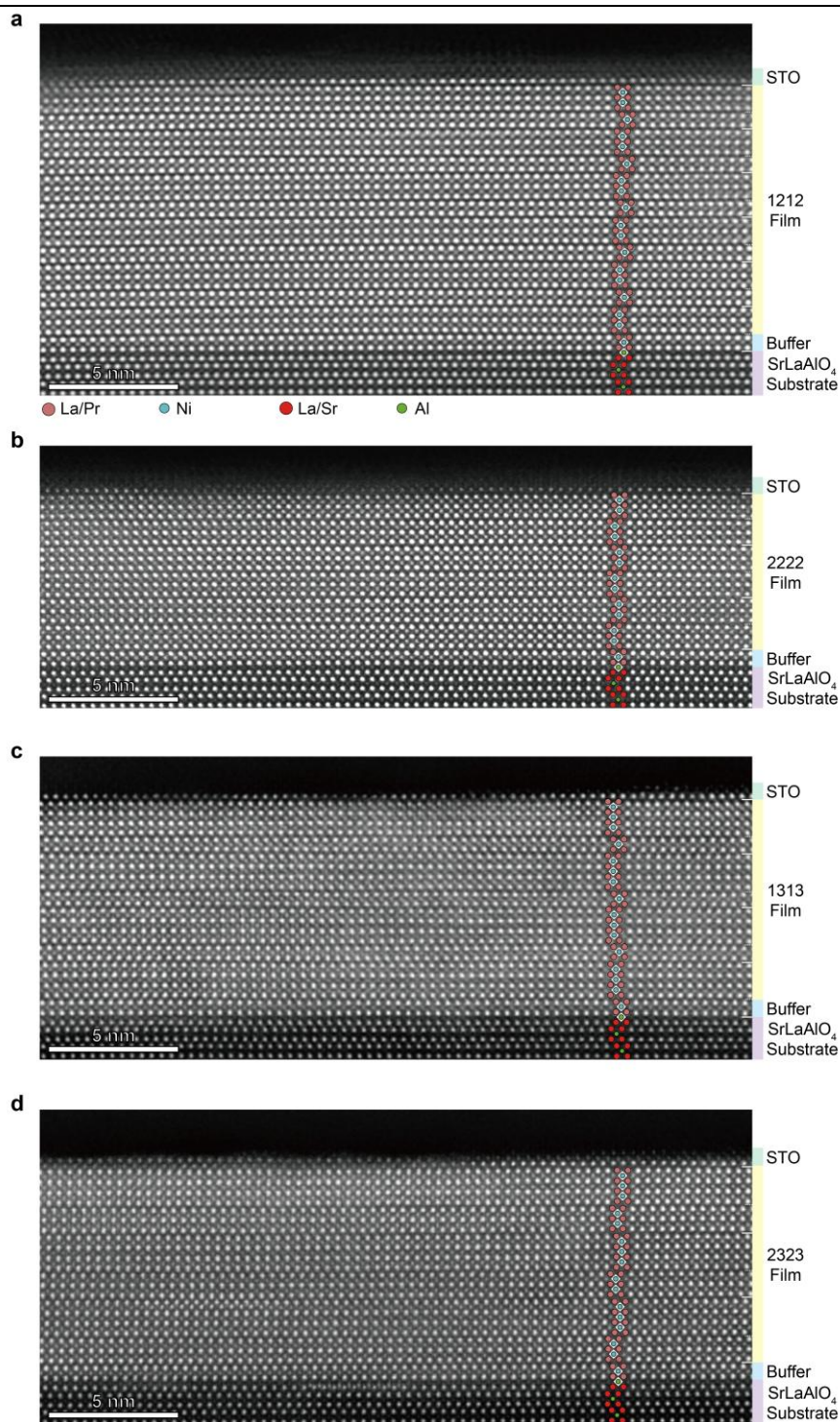


Figure 4-6 HAADF images of the 1212 (a), 2222 (b), 1313 (c) and 2323 (d) films on SrLaAlO₄ substrates with a large field of view. Regions corresponding to the STO capping layer, film, buffer layer and substrate are indicated by colored rectangles. Solid white lines mark the unit-cell boundaries, while dashed white lines separate different constituent blocks within each unit cell. All samples prepared for STEM characterization were capped with SrTiO₃ (STO) to prevent damage during focused ion beam (FIB) processing. Scale bars: 5 nm (a–d).

The superconducting performance of the 1212 and 2323 films was optimized by tuning thermodynamic growth conditions to achieve optimal oxygen stoichiometry, after the cation stoichiometry had been carefully calibrated. For the 2323 thin films, a systematic increase in ozone partial pressure was employed to induce superconductivity. As shown in Figure 4-7a, increasing the ozone pressure from ~ 0.3 Pa to ~ 3 Pa leads to a continuous decrease in room-temperature resistivity. Correspondingly, the transport behavior evolves from weakly insulating, to exhibiting signatures of superconductivity with a subtle resistivity drop below 10 K, and eventually to a well-defined superconducting transition with $T_{c,\text{onset}}$ above 40 K and zero resistance achieved at $T_{c,0} \approx 3.5$ K.

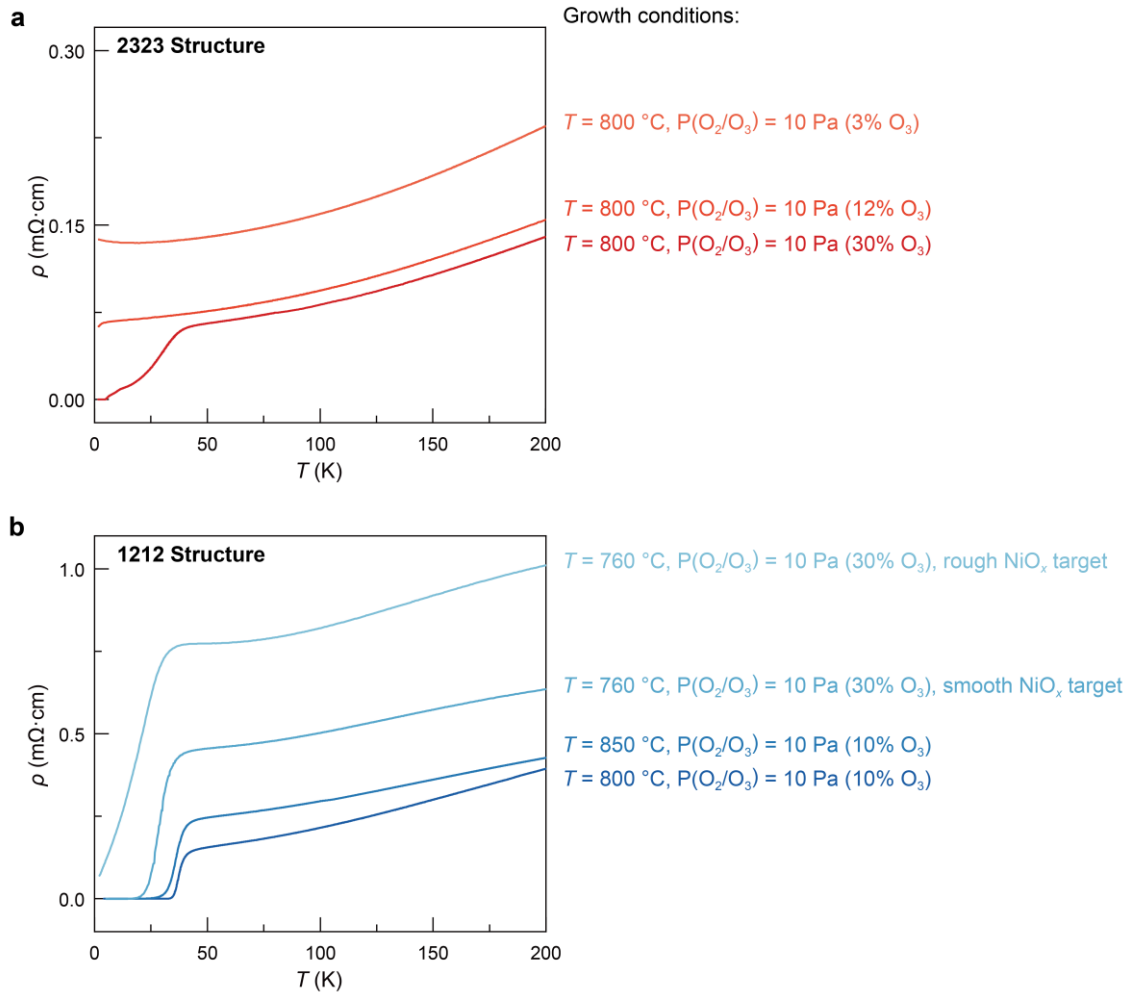


Figure 4-7 Transport properties of 2323 and 1212 thin films under varying growth conditions. ρ - T curves of 2323 films (a) and 1212 films (b) grown under different temperatures and oxidizing conditions. A color scale (red or blue, from light to dark) represents increasing oxidation strength of the corresponding growth conditions.

For the 1212 thin films (Figure 4-7b), although the growth parameters, temperature and ozone partial pressure, were not independently controlled, a similar trend is observed. Samples with lower room-temperature resistivity, indicative of reduced oxygen vacancy concentration, exhibit a more robust zero-resistance state. The optimal sample (darkest blue curve) reaches a $T_{c,0}$ of approximately 30 K, which is comparable to that of bilayer $(\text{La,Pr})_3\text{Ni}_2\text{O}_7/\text{SrLaAlO}_4$ films ^[113]. Notably, the top two samples were grown under identical temperature, oxidizing conditions, and laser fluence ($1.44 \text{ J}\cdot\text{cm}^{-2}$), yet their resistivities differ significantly. This discrepancy is attributed to differences in the surface roughness of the NiO_x target used for ablation. A smoother NiO_x target surface is expected to produce a more uniform laser plume and generate plasma species with higher kinetic energy. These energetic species interact more effectively with the background gas, thereby enhancing the oxidation capability during growth. Consequently, carefully sintered and polished NiO_x targets favor the growth of thin films with fewer oxygen vacancies, lower resistivity and improved superconducting performance.

In summary, beyond cation stoichiometry calibration which determines phase formation in the 2323 and 1212 hybrid superstructures, optimized oxidation conditions are crucial for achieving superior superconducting properties. Appropriate growth temperature and ozone partial pressure, together with sufficiently high kinetic energy of ablated species promoted by smooth NiO_x target surfaces, collectively suppress oxygen vacancies and enhance superconductivity in these films.

4.3 Magnetotransport Properties of 1212 and 2323 Films

The magnetic-field response of the 1212 and 2323 films reveals distinct differences between these two superconducting nickelate superstructures, as shown in Figure 4-8. Figure 4-8a and 4-8b present the anisotropic ρ - T responses of a 1212 thin film under perpendicular and parallel magnetic fields. The out-of-plane ($B_{c,\perp}$) and in-plane ($B_{c,\parallel}$) critical fields are extracted using both $T_{c,95\%}$ and $T_{c,50\%}$ criteria (Figure 4-8c). Under both criteria, $B_{c,\perp}$ exhibits a linear temperature dependence while $B_{c,\parallel}$ follows a square-root dependence, consistent with the 2D

Ginzburg–Landau model. Fitting the 95% data yields an in-plane coherence length $\xi_{ab}(0) \approx 1.9$ nm, comparable to that of bilayer nickelate films ^[97,108]. The effective superconducting thickness is determined to be $d = 5.7 \pm 0.8$ nm, on the same order as the film thickness (9.9 nm, 6UC). Furthermore, the angular dependence of $T_{c,50\%}$ in the 1212 film (Figure 4-8d) exhibits a sharp cusp near the in-plane field configuration, which cannot be captured by 3D Ginzburg–Landau model but is well described by the 2D Tinkham model. This behavior resembles that observed in pure bilayer 2222 films ^[108,114].

In contrast, although the 2323 thin film also exhibits anisotropic responses under perpendicular (Figure 4-8e) and parallel (Figure 4-8f) magnetic fields, its critical-field behavior (Figure 4-8g) deviates from that of both 1212 and 2222 phases. For the $T_{c,95\%}$ criterion, both $B_{c,\perp}$ and $B_{c,\parallel}$ can still be described within the 2D Ginzburg–Landau framework, yielding $\xi_{ab}(0) \approx 3.4$ nm and a superconducting thickness $d = 3.5 \pm 0.1$ nm (film thickness: 3UC, 8.3 nm).

However, for the $T_{c,50\%}$ criterion, both $B_{c,\perp}$ and $B_{c,\parallel}$ exhibit pronounced positive curvature, which cannot be captured by the 2D Ginzburg–Landau model. Instead, the data can be well fitted using Gurevich's two-band model ^[121]. Additionally, the angular dependence of $T_{c,50\%}$ in the 2323 film (Figure 4-8h) shows anomalous behavior. Near zero angle, $T_{c,50\%}$ exhibits an exceptionally sharp increase, resulting in an extremely narrow peak that cannot be reproduced using a single Tinkham model. To account for this, the data are divided into two angular regimes, one near the zero-angle region fitted by a Tinkham function, and the remaining data fitted by a separate Tinkham function.

These magnetotransport anomalies, together with the commonly observed two-step superconducting transition with the second transition occurring around 10–20 K (Figure 4-3g), suggest that the broad transition in the 2323 films (with $T_{c,onset}$ above 40 K but zero resistance only achieved at 2–3 K) is intrinsic in nature. A possible origin is that the insertion of a trilayer block (~ 1.4 nm) disrupts global phase coherence between bilayer superconducting units. In the 2323 superstructure, achieving a zero-resistance state likely requires coupling between bilayer blocks mediated by proximity-induced superconductivity within the intervening trilayer nickelates, implying the coexistence of two superconducting

components at low temperatures. By contrast, the insertion of a monolayer block (~ 0.6 nm) in the 1212 superstructure does not significantly disrupt global coherence between bilayer nickelates. As a result, the optimal $T_{c,0}$ of 1212 films reaches ~ 30 K (Figure 4-3c), comparable to that of pure 2222 films^[113]. This systematical evolution of superconducting behavior with structural spacer modulation provides important insight into the underlying mechanism of superconductivity in bilayer nickelates.

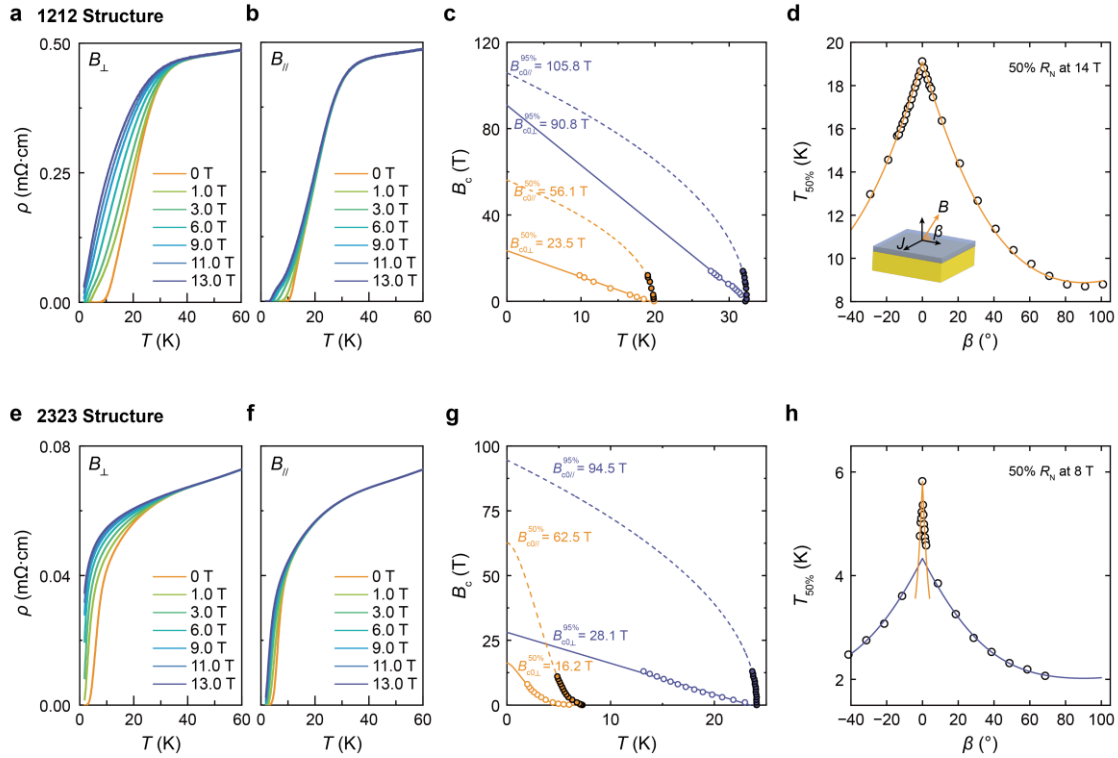


Figure 4-8 Magnetic-field responses of 1212 and 2323 nickelate thin films. (a, b) ρ - T curves of a superconducting 1212 film under magnetic fields applied perpendicular (a) and parallel (b) to the film plane. (c) Temperature dependence of the in-plane (solid circles) and out-of-plane (open circles) critical fields. Critical fields are extracted using both $T_{c,95\%}$ (purple) and $T_{c,50\%}$ (orange). (d) Angular dependence of the critical temperature $T_{c,50\%}$ under an applied magnetic field of 14 T. The inset illustrates the measurement geometry, where β is the angle between the applied field and the film plane. Open circles represent experimental data. The orange solid curve is a fit to the Tinkham model. (e, f) Corresponding ρ - T curves of a superconducting 2323 film under perpendicular (e) and parallel (f) magnetic fields. (g) Temperature-dependent in-plane (solid circles) and out-of-plane (open circles) critical fields for the 2323 film. The 2D Ginzburg-Landau model is used to fit $B_{c,95\%}$, while Gurevich's two-band model is used for $B_{c,50\%}$. (h) Angular dependence of $T_{c,50\%}$ for the 2323 film under an applied magnetic field of 8 T. The data are divided into two angular regimes for fitting. The sharp peak near zero angle is fitted with one Tinkham function (orange curve), while the broader background is fitted with another (purple curve).

4.4 Electronic Band Structures

The comparative ARPES studies of 1212, 2222, 1313 and 2323 superstructure thin films are presented in Figure 4-9. Different photon energies are employed, as the spectral intensities of various bands are selectively enhanced at specific photon energies. This effect likely arises from the variation in photoemission cross-sections of different orbitals rather than being simply attributed to k_z dispersion. The Fermi surface maps of superconducting 1212 and 2222 films (Figures 4-9a and 4-9c) reveal similar topologies, consisting of α and β pockets, along with a prominent γ pocket at the Brillouin zone corner (M point). Their corresponding spectral cuts along the M–X–M high-symmetry direction (Figures 4-9b and 4-9d) show that the γ band crosses the Fermi level (E_F). In addition, a pronounced vertical dispersion near the M point is observed, whose origin becomes clearer in the ARPES spectra of the 1313 superstructure.

Figures 4-9e and 4-9f present the Fermi surface map and corresponding spectral cut of the non-superconducting 1313 film. The α and β bands form the underlying Fermi pockets, similar to those in the 1212 and 2222 films. In contrast, the γ band is located approximately 70 meV below E_F , which is further shifted downward compared to bulk 1313 compounds where it lies about 20 meV below E_F . This band exhibit a relatively flat dispersion and develops a slight dip near the M point, which evolves into a nearly vertical, momentum-independent intensity tail. This waterfall-like feature may originate from strong electron correlations in the d_{z^2} orbital, and has also been observed in infinite-layer nickelate thin films [41,42] and bulk trilayer RP nickelates [122].

Figures 4-9g and 4-9h show the ARPES results of the superconducting 2323 film. Two γ bands are clearly resolved in the spectral cut (Figure 4-9h). One γ^{II} band crosses E_F (marked by red open circles), resembling the behavior in 1212 and 2222 phases, while another γ^{III} band lies below E_F (marked by red solid circles), similar to the 1313 phase. Considering that the monolayer RP nickelate is insulating and does not contribute to the photoemission intensity near E_F , the γ^{II} and γ^{III} bands can be reasonably attributed to bilayer and trilayer RP nickelates, respectively, under the present strain and oxidation conditions.

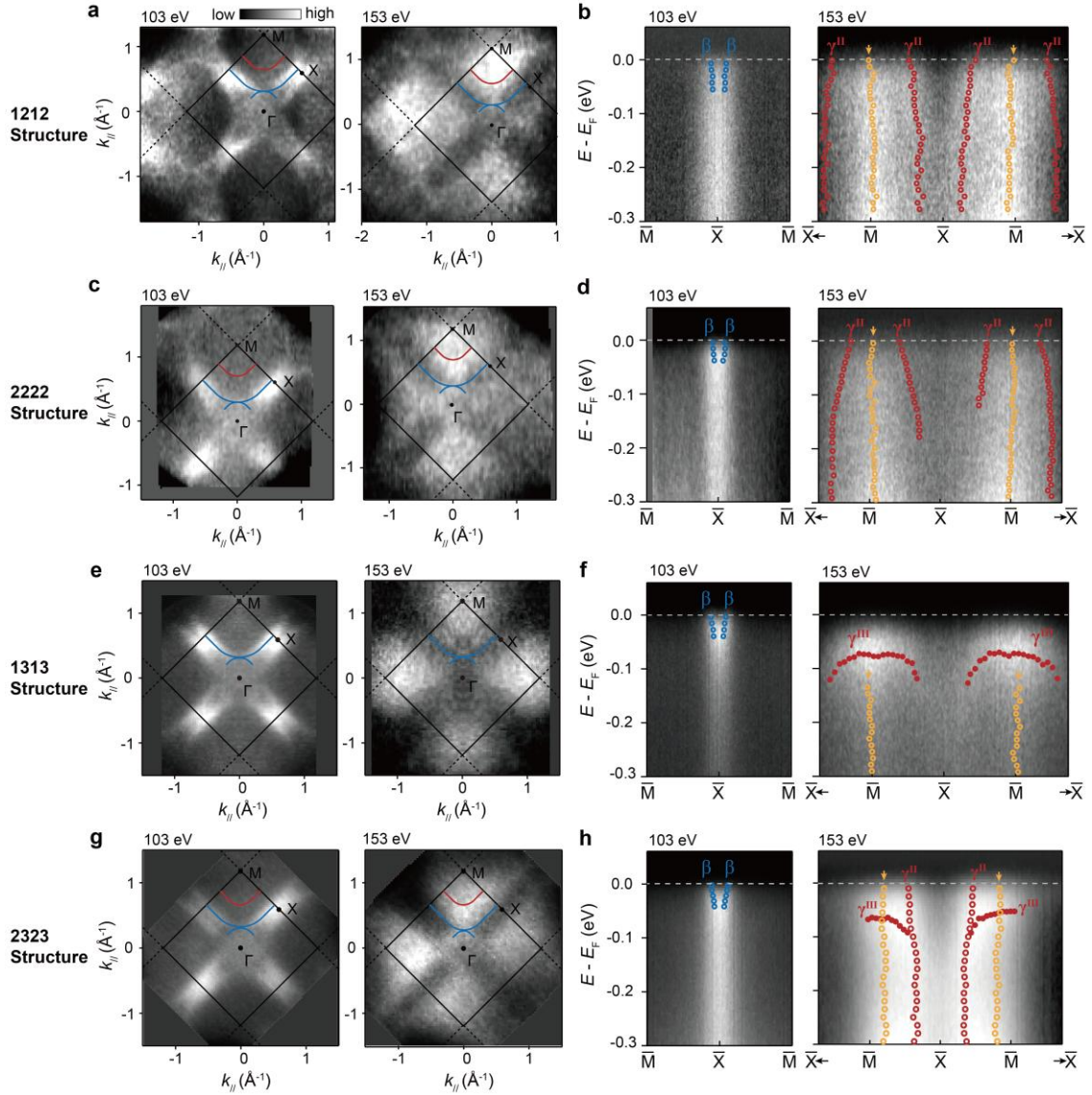


Figure 4-9 Electronic band structures of 1212, 2222, 1313 and 2323 nickelate thin films. (a) Fermi surface map of the 1212 film measured using photon energies of 103 eV (left) and 153 eV (right). The integration window is 50 meV around E_F . Schematic Fermi surface contours are overlaid on the experimental data. (b) ARPES spectral cuts of the 1212 film along the M–X–M direction. Peak positions extracted from momentum distribution curve (MDC) fits are indicated by open circles. The yellow arrow highlights the vertical dispersion near the M point. The β and γ bands are more pronounced at 103 eV (left) and 153 eV (right), respectively. (c, d) Fermi surface map and spectral cuts of the 2222 film. (e, f) Fermi surface map and spectral cuts of the 1313 film. Solid circles are derived from energy distribution curve (EDC) fits. (g, h) Fermi surface map and spectral cuts of the 2323 film. The 1212, 2222 and 2323 films are bilayer-terminated, while the 1313 film is trilayer-terminated. Film thicknesses are 7 nm (1212), 5 nm (2222), 8 nm (1313) and 6 nm (2323).

The orbital character of the γ^{II} and γ^{III} bands is further investigated via polarization-dependent ARPES measurements on the superconducting 2323 film.

Figure 4-10a illustrates the measurement geometry, in which the d_{z^2} orbital intensity is enhanced under linear vertical (LV) polarization. Figure 4-10b presents spectral cuts along the $M-\Gamma-M$ direction measured using linear horizontal (LH) (left) and LV (right) polarized photons. Under LH polarization, only the β band is observed, confirming its $d_{x^2-y^2}$ -derived character. In contrast, the γ^{II} and γ^{III} bands are clearly resolved under LV polarization, confirming their d_{z^2} -derived nature. The residual intensity of the β band under LV polarization is attributed to contributions from hybridized oxygen p orbitals.

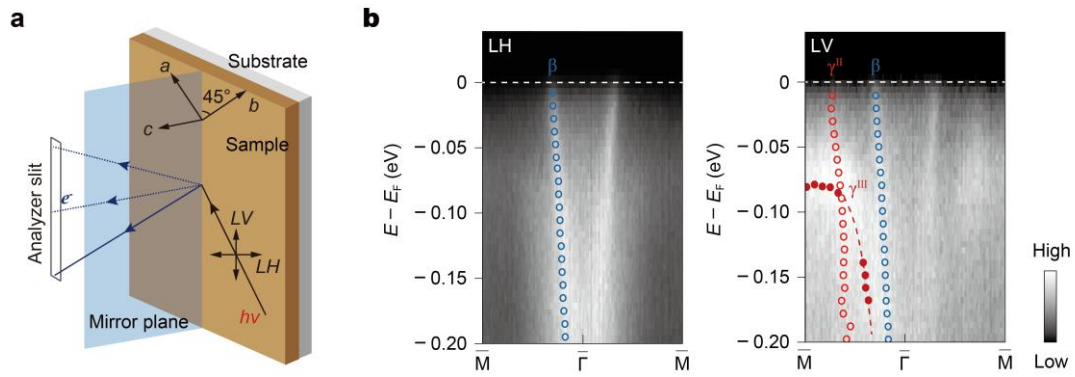


Figure 4-10 Polarization-dependent ARPES measurements of the 2323 superstructure thin film. (a) Measurement geometry with polarized photons. (b) ARPES spectral cuts along the $M-\Gamma-M$ direction measured with linear horizontal (LH, left) and linear vertical (LV, right) polarized photons at 103 eV. The film thickness is 5 nm with trilayer termination.

Considering the susceptibility of bilayer nickelate thin films to thermal oxygen loss, all samples for ARPES measurements were cooled to below 100 °C after growth before being transferred into the load-lock chamber and subsequently loaded into a cryogenic ultra-high-vacuum suitcase equipped with an ion pump. The base pressure of the suitcase was maintained below 5×10^{-10} torr. The samples were then rapidly cooled to below 200 K in the suitcase and maintained at this low temperature throughout the transportation process to the ARPES end station at the synchrotron, which typically took approximately 24 h. During measurements, the sample holder temperature was kept below 15 K, and the base pressure of the beamline station was lower than 7×10^{-11} torr. No additional *in-situ* annealing or surface cleaning was performed prior to ARPES measurements. Although weak surface adsorption under prolonged low-temperature storage in ultra-

high vacuum cannot be completely excluded, such effects are expected to be consistent across all samples and therefore unlikely to affect the comparative conclusions regarding the intrinsic electronic structure differences between superconducting and non-superconducting phases. Despite the possible adsorption effect, this cold-chain protocol effectively preserves the superconducting properties and minimizes surface oxygen loss of the ARPES samples during transportation. The ARPES measurements were carried out at beamline BL03U of the Shanghai Synchrotron Radiation Facility.

In summary, the superconducting 1212, 2222 and 2323 phases all exhibit a γ^{II} band crossing E_{F} , while the γ^{III} band in the non-superconducting 1313 phase remains below E_{F} . These comparative results suggest a close correlation between the presence of a d_{z^2} -derived γ band at the Fermi level and the emergence of superconductivity in RP nickelates.

4.5 Summary and Conclusions

This chapter presents a systematic comparative study of three nickelate superstructures alongside the pure bilayer 2222 phase. Ambient-pressure superconductivity is realized in the 1212 and 2323 superstructures, both exhibiting superconducting onset temperature exceeding the McMillan limit, enabled by epitaxial compressive strain imposed by SrLaAlO_4 substrates. Under the same strain conditions, the 1313 superstructure displays weakly insulating behavior.

Magnetotransport measurements reveal that 2323 phase possesses distinct characteristics compared to the closely related 1212 and 2222 phases. The ρ - T curves of 2323 consistently show a two-step superconducting transition and its temperature-dependent critical fields are well described by Gurevich's two-band model. This anomalous behavior suggests that global phase coherence in the 2323 superstructure may be established via proximitized superconductivity within the intervening trilayer blocks, which couple the superconducting bilayer units.

ARPES measurements uncover the key electronic distinctions among these four nickelate phases, particularly in terms of the position of the γ band. In the superconducting 1212 and 2222 phases, the γ band crosses the Fermi level and forms the underlying Fermi pocket. In contrast, in the non-superconducting 1313

phase, the γ band lies approximately 70 meV below E_F . Notably, the superconducting 2323 superstructure hosts two γ bands, a γ^{II} band attributed to the bilayer unit that crosses E_F , and a γ^{III} band attributed to the trilayer unit that remains below E_F . This comparison identifies the position of the d_{z^2} -derived γ band relative to the Fermi level as a key electronic factor distinguishing superconducting and non-superconducting phases.

These findings not only expand the family of nickelate superconductors at ambient pressure, but also provide compelling experimental evidence for the critical role of the d_{z^2} orbital in shaping high-temperature superconductivity in Ruddlesden–Popper nickelates.

CHAPTER 5 CONCLUSION AND OUTLOOK

5.1 Conclusion

This dissertation systematically investigates the realization and underlying mechanisms of ambient-pressure superconductivity in Ruddlesden–Popper (RP) nickelate thin films. By employing the advanced Gigantic-Oxidative Atomic-Layer-by-Layer Epitaxy (GAE) methodology, ambient-pressure superconductivity has been realized in bilayer RP nickelate thin films, $(\text{La,Pr})_3\text{Ni}_2\text{O}_7$, as well as in related hybrid superstructures, $(\text{La,Pr})_5\text{Ni}_3\text{O}_{11}$ (1212 phase) and $(\text{La,Pr})_7\text{Ni}_5\text{O}_{17}$ (2323 phase). Comparative ARPES studies reveal the critical role of the d_{z^2} -derived γ band at the Fermi level in the emergence of high-temperature superconductivity in RP nickelates.

The main conclusions are summarized as follows:

(1) By systematically exploring the thin-film growth of $(\text{La,Ca})_3\text{Ni}_2\text{O}_7$ on LaAlO_3 substrates under varied thermodynamic conditions using the GAE methodology, a clear decoupling between phase formation and oxygen stoichiometry control has been established. The growth of high-quality bilayer nickelate films relies on the precise calibration of the pulse numbers for each target to ensure complete atomic layer coverage. A two-step calibration protocol comprising ratio calibration and periodicity calibration guided by XRD patterns is proposed. Once the desired phase is stabilized, the oxygen stoichiometry can be flexibly tuned by leveraging the strong oxidizing capability of GAE, enabled by high ozone concentrations during growth. This methodology provides a solid foundation for robust sample optimization in subsequent studies.

(2) By growing $\text{La}_{2.85}\text{Pr}_{0.15}\text{Ni}_2\text{O}_7$ films on SrLaAlO_4 substrates using GAE, superconductivity in bilayer RP nickelates has been successfully realized at ambient pressure, stabilized by compressive strain and optimized oxygen stoichiometry. The dual evidence of zero resistance and the Meissner effect confirm the superconducting nature. The superconducting onset temperature, $T_{\text{c,onset}} \approx 45$ K, exceeds the McMillan limit, placing nickelates among high-temperature superconductors at ambient pressure.

(3) Taking advantage of the atomic-level control enabled by the GAE method for synthesizing designed heterostructures, ambient-pressure superconductivity is further realized in $(\text{La}_{0.67}\text{Pr}_{0.33})_5\text{Ni}_3\text{O}_{11}$ and $(\text{La}_{0.67}\text{Pr}_{0.33})_7\text{Ni}_5\text{O}_{17}$ superstructure thin films grown on SrLaAlO_4 substrates. Under identical strain conditions, the hybrid $(\text{La}_{0.67}\text{Pr}_{0.33})_3\text{Ni}_2\text{O}_7$ (1313 phase) films exhibit weakly insulating behavior. Comparative ARPES measurements across these superstructures and the pure bilayer 2222 phase establish a strong correlation between Fermi surface topology and superconductivity. In particular, the d_{z^2} -derived γ band crossing the Fermi level (E_F) was identified as the critical electronic origin of superconductivity in RP nickelates, highlighting their multi-orbital nature and distinguishing them from single-band cuprates ^[123].

In summary, these findings not only establish bilayer nickelates and their derived superstructures as a robust platform for exploring high-temperature superconductivity at ambient pressure, but also provide a promising roadmap for engineering superconductivity in correlated oxide heterostructures.

5.2 Outlook

Despite these advances, ambient-pressure superconductivity in trilayer RP nickelates remains elusive. In 1313 films grown on compressively strained SrLaAlO_4 substrates, the γ band is further shifted downward relative to the bulk, in contrast to the bilayer 2222 phase where compressive strain lifts the γ band to cross E_F . This opposite trend suggests that tensile strain (e.g., via LSAT or SrTiO_3 substrates) may be a promising route for inducing superconductivity in trilayer nickelates at ambient pressure.

Such efforts would enable systematic comparisons between bilayer and trilayer RP nickelates using spectroscopic probes such as ARPES to elucidate why T_c declines in the trilayer system, opposite to the trend observed in the multilayer cuprates. These comparisons may offer important clues to the mechanism of high-temperature superconductivity and guide the design of materials with higher T_c .

REFERENCES

- [1] ONNES K. The Resistance of pure mercury at helium temperatures[J]. Communications from the Physical Laboratory of the University of Leiden, b, 1911, 120.
- [2] MEISSNER W, OCHSENFELD R. Ein neuer effekt bei eintritt der supra-leitfähigkeit[J]. Naturwissenschaften, 1933, 21: 787-788.
- [3] BARDEEN J, COOPER L N, SCHRIEFFER J R. Theory of superconductivity[J]. Physical Review, 1957, 108(5): 1175.
- [4] MCMILLAN W L. Transition temperature of strong-coupled superconductors[J]. Physical Review, 1968, 167(2): 331-344.
- [5] BEDNORZ J G, MÜLLER K A. Possible high T_c superconductivity in the Ba-La-Cu-O system[J]. Zeitschrift für Physik B Condensed Matter, 1986, 64(2): 189-193.
- [6] WU M K, ASHBURN J R, TORNG C J, et al. Superconductivity at 93 K in a new mixed-phase Y-Ba-Cu-O compound system at ambient pressure[J]. Physical Review Letters, 1987, 58(9): 908.
- [7] 赵忠贤, 陈立泉, 杨乾声, 等. Ba-Y-Cu 氧化物液氮温区的超导电性[J]. 科学通报, 1987, 32: 412-414.
- [8] PUPHAL P, SCHÄFER T, KEIMER B, et al. Superconductivity in infinite-layer and Ruddlesden-Popper nickelates[J]. Nature Reviews Physics, 2026, 8(2): 70-85.
- [9] STEGLICH F, AARTS J, BREDEL C D, et al. Superconductivity in the presence of strong Pauli paramagnetism: CeCu_2Si_2 [J]. Physical Review Letters, 1979, 43(25): 1892-1896.
- [10] KAMIHARA Y, WATANABE T, HIRANO M, et al. Iron-based layered superconductor $\text{La}[\text{O}_{1-x}\text{F}_x]\text{FeAs}$ ($x = 0.05-0.12$) with $T_c = 26$ K[J]. Journal of the American Chemical Society, 2008, 130(11): 3296-3297.
- [11] CHEN X H, WU T, WU G, et al. Superconductivity at 43 K in $\text{SmFeAsO}_{1-x}\text{F}_x$ [J]. Nature, 2008, 453(7196): 761-762.
- [12] LI D, LEE K, WANG B Y, et al. Superconductivity in an infinite-layer nickelate[J]. Nature, 2019, 572(7771): 624-627.
- [13] CHU C W, DENG L Z, LV B. Hole-doped cuprate high temperature superconductors[J]. Physica C: Superconductivity and its Applications, 2015, 514: 290-313.
- [14] HARTER J W. Angle-resolved photoemission spectroscopy of $\text{Sr}_{1-x}\text{La}_x\text{CuO}_2$ thin films grown by molecular-beam epitaxy[D]. Ithaca: Cornell University, 2013.
- [15] LEE Y S, BIRGENEAU R J, KASTNER M A, et al. Neutron-scattering study of spin-density wave order in the superconducting state of excess-oxygen-doped $\text{La}_2\text{CuO}_{4+y}$ [J]. Physical Review B, 1999, 60(5): 3643-3654.

REFERENCES

- [16] KEIMER B, KIVELSON S A, NORMAN M R, et al. From quantum matter to high-temperature superconductivity in copper oxides[J]. *Nature*, 2015, 518(7538): 179-186.
- [17] MOTT N F. The basis of the electron theory of metals, with special reference to the transition metals[J]. *Proceedings of the Physical Society. Section A*, 1949, 62(7): 416-422.
- [18] ANDERSON P W. Antiferromagnetism. Theory of superexchange interaction[J]. *Physical Review*, 1950, 79(2): 350-356.
- [19] LEE P A, NAGAOSA N, WEN X G. Doping a Mott insulator: Physics of high-temperature superconductivity[J]. *Reviews of Modern Physics*, 2006, 78(1): 17-85.
- [20] CHEN C T, SETTE F, MA Y, et al. Electronic states in $\text{La}_{2-x}\text{Sr}_x\text{CuO}_{4+\delta}$ probed by soft-x-ray absorption[J]. *Physical Review Letters*, 1991, 66(1): 104-107.
- [21] ANDERSON P W. The resonating valence bond state in La_2CuO_4 and superconductivity[J]. *Science*, 1987, 235(4793): 1196-1198.
- [22] NORMAN M R. Materials design for new superconductors[J]. *Reports on Progress in Physics*, 2016, 79(7): 074502.
- [23] ZHANG J, BOTANA A S, FREELAND J W, et al. Large orbital polarization in a metallic square-planar nickelate[J]. *Nature Physics*, 2017, 13(9): 864-869.
- [24] LI Z, GUO W, ZHANG T T, et al. Epitaxial growth and electronic structure of Ruddlesden–Popper nickelates ($\text{La}_{n+1}\text{Ni}_n\text{O}_{3n+1}$, $n = 1-5$)[J]. *APL Materials*, 2020, 8(9): 091112.
- [25] PAN G A, FERENC SEGEDIN D, LABOLLITA H, et al. Superconductivity in a quintuple-layer square-planar nickelate[J]. *Nature Materials*, 2022, 21(2): 160-164.
- [26] YAN X, ZHENG H, LI Y, et al. Superconductivity in an ultrathin multilayer nickelate[J]. *Science Advances*, 2025, 11(1): eado4572.
- [27] POLTAVETS V V, LOKSHIN K A, DIKMEN S, et al. $\text{La}_3\text{Ni}_2\text{O}_6$: A new double T'-type nickelate with infinite $\text{Ni}^{1+/2+}\text{O}_2$ layers[J]. *Journal of the American Chemical Society*, 2006, 128(28): 9050-9051.
- [28] LEE K, WANG B Y, OSADA M, et al. Linear-in-temperature resistivity for optimally superconducting $(\text{Nd,Sr})\text{NiO}_2$ [J]. *Nature*, 2023, 619(7969): 288-292.
- [29] ZENG S, TANG C S, YIN X, et al. Phase diagram and superconducting dome of infinite-layer $\text{Nd}_{1-x}\text{Sr}_x\text{NiO}_2$ thin films[J]. *Physical Review Letters*, 2020, 125(14): 147003.
- [30] LI D, WANG B Y, LEE K, et al. Superconducting dome in $\text{Nd}_{1-x}\text{Sr}_x\text{NiO}_2$ infinite layer films[J]. *Physical Review Letters*, 2020, 125(2): 027001.
- [31] TAKAGI H, IDO T, ISHIBASHI S, et al. Superconductor-to-nonsuperconductor transition in $(\text{La}_{1-x}\text{Sr}_x)_2\text{CuO}_4$ as investigated by transport and magnetic measurements[J]. *Physical Review B*, 1989, 40(4): 2254-2261.

REFERENCES

- [32] PARZYCK C T, GUPTA N K, WU Y, et al. Absence of $3a_0$ charge density wave order in the infinite-layer nickelate NdNiO₂[J]. Nature Materials, 2024, 23(4): 486-491.
- [33] HAYWARD M A, GREEN M A, ROSSEINSKY M J, et al. Sodium hydride as a powerful reducing agent for topotactic oxide deintercalation: synthesis and characterization of the nickel(I) oxide LaNiO₂[J]. Journal of the American Chemical Society, 1999, 121(38): 8843-8854.
- [34] HAYWARD M A, ROSSEINSKY M J. Synthesis of the infinite layer Ni(I) phase NdNiO_{2+x} by low temperature reduction of NdNiO₃ with sodium hydride[J]. Solid State Sciences, 2003, 5(6): 839-850.
- [35] LU H, ROSSI M, NAG A, et al. Magnetic excitations in infinite-layer nickelates[J]. Science, 2021, 373(6551): 213-216.
- [36] FOWLIE J, HADJIMICHAEL M, MARTINS M M, et al. Intrinsic magnetism in superconducting infinite-layer nickelates[J]. Nature Physics, 2022, 18(9): 1043-1047.
- [37] GOODGE B H, LI D, LEE K, et al. Doping evolution of the Mott–Hubbard landscape in infinite-layer nickelates[J]. Proceedings of the National Academy of Sciences, 2021, 118(2): e2007683118.
- [38] HEPTING M, LI D, JIA C J, et al. Electronic structure of the parent compound of superconducting infinite-layer nickelates[J]. Nature Materials, 2020, 19(4): 381-385.
- [39] LI D F. The discovery and research progress of the nickelate superconductors (in Chinese). Scientia Sinica-Physica, Mechanica & Astronomica, 2021, 51: 047405.
- [40] SAKAKIBARA H, USUI H, SUZUKI K, et al. Model construction and a possibility of cupratelike pairing in a new d^9 nickelate superconductor (Nd,Sr)NiO₂[J]. Physical Review Letters, 2020, 125(7): 077003.
- [41] SUN W, JIANG Z, XIA C, et al. Electronic structure of superconducting infinite-layer lanthanum nickelates[J]. Science Advances, 2025, 11(4): eadr5116.
- [42] XIANG D, YU F, XIAOXIAO W, et al. Cuprate-like electronic structures in infinite-layer nickelates with substantial hole dopings[J]. National Science Review, 2024, 11(8): nwae194.
- [43] LI C, CHEN Y, DING X, et al. Observation of electriddelike s states coexisting with correlated d electrons in NdNiO₂[J]. Physical Review Letters, 2025, 135(11): 116501.
- [44] OSADA M, WANG B Y, GOODGE B H, et al. Nickelate superconductivity without rare-earth magnetism: (La,Sr)NiO₂[J]. Advanced Materials, 2021, 33(45): 2104083.
- [45] PARZYCK C T, WU Y, BHATT L, et al. Superconductivity in the parent infinite-layer nickelate NdNiO₂[J]. Physical Review X, 2025, 15(2): 021048.
- [46] SAHIB H, RAJI A, ROSA F, et al. Superconductivity in PrNiO₂ infinite-layer nickelates[J]. Advanced Materials, 2025, 37(16): 2416187.
- [47] CHOW S L E, LUO Z, ARIANDO A. Bulk superconductivity near 40 K in hole-doped SmNiO₂ at ambient pressure[J]. Nature, 2025, 642(8066): 58-63.

REFERENCES

- [48] ZENG S, LI C, CHOW L E, et al. Superconductivity in infinite-layer nickelate $\text{La}_{1-x}\text{Ca}_x\text{NiO}_2$ thin films[J]. *Science Advances*, 2022, 8(7): eabl9927.
- [49] OSADA M, WANG B Y, LEE K, et al. Phase diagram of infinite layer praseodymium nickelate $\text{Pr}_{1-x}\text{Sr}_x\text{NiO}_2$ thin films[J]. *Physical Review Materials*, 2020, 4(12): 121801.
- [50] WEI W, VU D, ZHANG Z, et al. Superconducting $\text{Nd}_{1-x}\text{Eu}_x\text{NiO}_2$ thin films using in situ synthesis[J]. *Science Advances*, 2023, 9(27): eadh3327.
- [51] WANG N N, YANG M W, YANG Z, et al. Pressure-induced monotonic enhancement of T_c to over 30 K in superconducting $\text{Pr}_{0.82}\text{Sr}_{0.18}\text{NiO}_2$ thin films[J]. *Nature Communications*, 2022, 13(1): 4367.
- [52] SUN H, HUO M, HU X, et al. Signatures of superconductivity near 80 K in a nickelate under high pressure[J]. *Nature*, 2023, 621(7979): 493-498.
- [53] ZHAN J, GU Y, WU X, et al. Cooperation between electron-phonon coupling and electronic interaction in bilayer nickelates $\text{La}_3\text{Ni}_2\text{O}_7$ [J]. *Physical Review Letters*, 2025, 134(13): 136002.
- [54] WANG M, WEN H H, WU T, et al. Normal and Superconducting Properties of $\text{La}_3\text{Ni}_2\text{O}_7$ [J]. *Chinese Physics Letters*, 2024, 41(7): 077402.
- [55] WANG Y, JIANG K, YING J, et al. Recent progress in nickelate superconductors[J]. *National Science Review*, 2025, 12(10): nwaf373.
- [56] ZHANG Y, SU D, HUANG Y, et al. High-temperature superconductivity with zero resistance and strange-metal behaviour in $\text{La}_3\text{Ni}_2\text{O}_{7-\delta}$ [J]. *Nature Physics*, 2024, 20(8): 1269-1273.
- [57] CHEN X, CHOI J, JIANG Z, et al. Electronic and magnetic excitations in $\text{La}_3\text{Ni}_2\text{O}_7$ [J]. *Nature Communications*, 2024, 15(1): 9597.
- [58] WANG L, LI Y, XIE S Y, et al. Structure responsible for the superconducting state in $\text{La}_3\text{Ni}_2\text{O}_7$ at high-pressure and low-temperature conditions[J]. *Journal of the American Chemical Society*, 2024, 146(11): 7506-7514.
- [59] WANG N, WANG G, SHEN X, et al. Bulk high-temperature superconductivity in pressurized tetragonal $\text{La}_2\text{PrNi}_2\text{O}_7$ [J]. *Nature*, 2024, 634(8034): 579-584.
- [60] LI F, XING Z, PENG D, et al. Bulk superconductivity up to 96 K in pressurized nickelate single crystals[J]. *Nature*, 2026, 649(8098): 871-878.
- [61] CHEN K, LIU X, JIAO J, et al. Evidence of spin density waves in $\text{La}_3\text{Ni}_2\text{O}_{7-\delta}$ [J]. *Physical Review Letters*, 2024, 132(25): 256503.
- [62] KHASANOV R, HICKEN T J, GAWRYLUK D J, et al. Pressure-enhanced splitting of density wave transitions in $\text{La}_3\text{Ni}_2\text{O}_{7-\delta}$ [J]. *Nature Physics*, 2025, 21(3): 430-436.
- [63] GUPTA N K, GONG R, WU Y, et al. Anisotropic spin stripe domains in bilayer $\text{La}_3\text{Ni}_2\text{O}_7$ [J]. *Nature Communications*, 2025, 16(1): 6560.

REFERENCES

- [64] KAKOI M, OI T, OHSHITA Y, et al. Multiband metallic ground state in multilayered nickelates $\text{La}_3\text{Ni}_2\text{O}_7$ and $\text{La}_4\text{Ni}_3\text{O}_{10}$ probed by ^{139}La -NMR at ambient pressure[J]. Journal of the Physical Society of Japan, 2024, 93(5): 053702.
- [65] LIU Z, HUO M, LI J. Electronic correlations and partial gap in the bilayer nickelate $\text{La}_3\text{Ni}_2\text{O}_7$ [J]. Nature Communications, 2024, 15(1): 7570.
- [66] TANIGUCHI S, NISHIKAWA T, YASUI Y, et al. Transport, magnetic and thermal properties of $\text{La}_3\text{Ni}_2\text{O}_{7-\delta}$. Journal of the Physical Society of Japan, 1995, 64(5): 1644-1650.
- [67] DONG Z, WANG G, WANG N, et al. Interstitial oxygen order and its competition with superconductivity in $\text{La}_2\text{PrNi}_2\text{O}_{7+\delta}$ [J]. Nature Materials, 2025, 24(12): 1927-1934.
- [68] DONG Z, HUO M, LI J, et al. Visualization of oxygen vacancies and self-doped ligand holes in $\text{La}_3\text{Ni}_2\text{O}_{7-\delta}$ [J]. Nature, 2024, 630(8018): 847-852.
- [69] LIU Y B, MEI J W, YE F, et al. s^\pm -wave pairing and the destructive role of apical oxygen deficiencies in $\text{La}_3\text{Ni}_2\text{O}_7$ under Pressure[J]. Physical Review Letters, 2023, 131(23): 236002.
- [70] YANG J, SUN H, HU X et al. Orbital-dependent electron correlation in double-layer nickelate $\text{La}_3\text{Ni}_2\text{O}_7$ [J]. Nature Communications, 2024, 15(1): 4373.
- [71] YANG Y F, ZHANG G M, ZHANG F C. Interlayer valence bonds and two-component theory for high- T_c superconductivity of $\text{La}_3\text{Ni}_2\text{O}_7$ under pressure[J]. Physical Review B, 2023, 108(20): L201108.
- [72] LU C, PAN Z, YANG F, et al. Interlayer-coupling-driven high-temperature superconductivity in $\text{La}_3\text{Ni}_2\text{O}_7$ under Pressure[J]. Physical Review Letters, 2024, 132(14): 146002.
- [73] YANG Q G, WANG D, WANG Q H. Possible s_\pm -wave superconductivity in $\text{La}_3\text{Ni}_2\text{O}_7$ [J]. Physical Review B, 2023, 108(14): L140505.
- [74] ZHU Y, PENG D, ZHANG E, et al. Superconductivity in pressurized trilayer $\text{La}_4\text{Ni}_3\text{O}_{10-\delta}$ single crystals[J]. Nature, 2024, 631(8021): 531-536.
- [75] ZHANG J, PHELAN D, BOTANA A S, et al. Intertwined density waves in a metallic nickelate[J]. Nature Communications, 2020, 11(1): 6003.
- [76] DOU J, LI F, ZHANG M, et al. Intertwined charge and spin density waves in trilayer nickelate $\text{La}_4\text{Ni}_3\text{O}_{10}$ revealed by ^{139}La NQR[J]. Physical Review B, 2026, 113(5): 054522.
- [77] XU S, WANG H, HUO M, et al. Collapse of density wave and emergence of superconductivity in pressurized- $\text{La}_4\text{Ni}_3\text{O}_{10}$ evidenced by ultrafast spectroscopy[J]. Nature Communications, 2025, 16(1): 7039.
- [78] LI H, ZHOU X, NUMMY T, et al. Fermiology and electron dynamics of trilayer nickelate $\text{La}_4\text{Ni}_3\text{O}_{10}$ [J]. Nature Communications, 2017, 8(1): 704.

REFERENCES

- [79] XIE W. The search for superconductivity just got wider[J]. *Nature*, 2024, 631: 509-510.
- [80] LUO X, CHEN H, LI Y, et al. Electronic origin of high superconducting critical temperature in trilayer cuprates[J]. *Nature Physics*, 2023, 19(12): 1841-1847.
- [81] WANG Z, ZOU C, LIN C, et al. Correlating the charge-transfer gap to the maximum transition temperature in $\text{Bi}_2\text{Sr}_2\text{Ca}_{n-1}\text{Cu}_n\text{O}_{2n+4+\delta}$ [J]. *Science*, 2023, 381(6654): 227-231.
- [82] LI F, GUO N, ZHENG Q, et al. Design and synthesis of three-dimensional hybrid Ruddlesden-Popper nickelate single crystals[J]. *Physical Review Materials*, 2024, 8(5): 053401.
- [83] SHI M, PENG D, FAN K, et al. Pressure induced superconductivity in hybrid Ruddlesden-Popper $\text{La}_5\text{Ni}_3\text{O}_{11}$ single crystals[J]. *Nature Physics*, 2025, 21(11): 1780-1786.
- [84] SHI M, PENG D, LI Y, et al. Spin density wave rather than tetragonal structure is prerequisite for superconductivity in $\text{La}_3\text{Ni}_2\text{O}_{7-\delta}$ [J]. *Nature Communications*, 2025, 16(1): 9141.
- [85] SHI M, LI Y, WANG Y, et al. Absence of superconductivity and density-wave transition in ambient-pressure tetragonal $\text{La}_4\text{Ni}_3\text{O}_{10}$ [J]. *Nature Communications*, 2025, 16(1): 2887.
- [86] PUPHAL P, REISS P, ENDERLEIN N, et al. Unconventional crystal structure of the high-pressure superconductor $\text{La}_3\text{Ni}_2\text{O}_7$ [J]. *Physical Review Letters*, 2024, 133(14): 146002.
- [87] HUANG C, LI J, HUANG X, et al. Superconductivity in monolayer-trilayer phase of $\text{La}_3\text{Ni}_2\text{O}_7$ under high pressure[A]. Preprint at arxiv.org/abs/2510.12250 (2025).
- [88] ABADI S, XU K J, LOMELI E G, et al. Electronic Structure of the Alternating Monolayer-Trilayer Phase of $\text{La}_3\text{Ni}_2\text{O}_7$ [J]. *Physical Review Letters*, 2025, 134(12): 126001.
- [89] PAN G A, SEGEDIN D F, TENHUISEN S F R, et al. Superconducting phase diagram of multi-layer square-planar nickelates[A]. Preprint at arxiv.org/abs/2602.19093 (2026).
- [90] SUN W, LI Y, CAI X, et al. Electronic and transport properties in Ruddlesden-Popper neodymium nickelates $\text{Nd}_{n+1}\text{Ni}_n\text{O}_{3n+1}$ ($n = 1-5$)[J]. *Physical Review B*, 2021, 104(18): 184518.
- [91] PAN G A, SONG Q, FERENC SEGEDIN D, et al. Synthesis and electronic properties of $\text{Nd}_{n+1}\text{Ni}_n\text{O}_{3n+1}$ Ruddlesden-Popper nickelate thin films[J]. *Physical Review Materials*, 2022, 6(5): 055003.

REFERENCES

- [92] LIU Y, OU M, CHU H, et al. Growth and characterization of the $\text{La}_3\text{Ni}_2\text{O}_{7-\delta}$ thin films: Dominant contribution of the $d_{x^2-y^2}$ orbital at ambient pressure[J]. *Physical Review Materials*, 2024, 8(12): 124801.
- [93] LEI Q, GOLALIKHANI M, DAVIDSON B A, et al. Constructing oxide interfaces and heterostructures by atomic layer-by-layer laser molecular beam epitaxy[J]. *npj Quantum Materials*, 2017, 2(1): 10.
- [94] ZHOU G, HUANG H, WANG F, et al. Gigantic-oxidative atomic-layer-by-layer epitaxy for artificially designed complex oxides[J]. *National Science Review*, 2025, 12(4): nwae429.
- [95] SHEPELIN N A, TEHRANI Z P, OHANNESSIAN N, et al. A practical guide to pulsed laser deposition[J]. *Chemical Society Reviews*, 2023, 52(7): 2294-2321.
- [96] REN X, SUTARTO R, WU X, et al. Resolving the electronic ground state of $\text{La}_3\text{Ni}_2\text{O}_{7-\delta}$ films[J]. *Communications Physics*, 2025, 8(1): 52.
- [97] KO E K, YU Y, LIU Y, et al. Signatures of ambient pressure superconductivity in thin film $\text{La}_3\text{Ni}_2\text{O}_7$ [J]. *Nature*, 2025, 638(8052): 935-940.
- [98] LEE J H, LUO G, TUNG I C, et al. Dynamic layer rearrangement during growth of layered oxide films by molecular beam epitaxy[J]. *Nature Materials*, 2014, 13(9): 879-883.
- [99] NIE Y F, ZHU Y, LEE C H, et al. Atomically precise interfaces from non-stoichiometric deposition[J]. *Nature Communications*, 2014, 5(1): 4530.
- [100] ZHANG J, ZHENG H, CHEN Y S, et al. High oxygen pressure floating zone growth and crystal structure of the metallic nickelates $\text{R}_4\text{Ni}_3\text{O}_{10}$ ($\text{R} = \text{La}, \text{Pr}$)[J]. *Physical Review Materials*, 2020, 4(8): 083402.
- [101] BARONE M R, DAWLEY N M, NAIR H P, et al. Improved control of atomic layering in perovskite-related homologous series[J]. *APL Materials*, 2021, 9(2): 021118.
- [102] WANG G, WANG N N, SHEN X L, et al. Pressure-induced superconductivity in polycrystalline $\text{La}_3\text{Ni}_2\text{O}_{7-\delta}$ [J]. *Physical Review X*, 2024, 14(1): 011040.
- [103] BISWAS A, JEONG Y H. Strain effect in epitaxial oxide heterostructures[M] // *Epitaxy*. London: IntechOpen, 2017.
- [104] LOCQUET J P, PERRET J, FOMPEYRINE J, et al. Doubling the critical temperature of $\text{La}_{1.9}\text{Sr}_{0.1}\text{CuO}_4$ using epitaxial strain[J]. *Nature*, 1998, 394(6692): 453-456.
- [105] BOZOVIC I, LOGVENOV G, BELCA I, et al. Epitaxial strain and superconductivity in $\text{La}_{2-x}\text{Sr}_x\text{CuO}_4$ thin films[J]. *Physical Review Letters*, 2002, 89(10): 107001.
- [106] SCHLOM D G, CHEN L Q, FENNIE C J, et al. Elastic strain engineering of ferroic oxides[J]. *MRS Bulletin*, 2014, 39(2): 118-130.
- [107] BISWAS A, YANG C H, RAMESH R, et al. Atomically flat single terminated oxide substrate surfaces[J]. *Progress in Surface Science*, 2017, 92(2): 117-141.

REFERENCES

- [108] ZHOU G, LV W, WANG H, et al. Ambient-pressure superconductivity onset above 40 K in $(\text{La,Pr})_3\text{Ni}_2\text{O}_7$ films[J]. *Nature*, 2025, 640(8059): 641-646.
- [109] KIM J, KIM Y, MUN J, et al. Defect engineering in $A_2\text{BO}_4$ thin films via surface-reconstructed LaSrAlO_4 substrates[J]. *Small Methods*, 2022, 6(11): 2200880.
- [110] BISWAS A, ROSSEN P B, RAVICHANDRAN J, et al. Selective A- or B-site single termination on surfaces of layered oxide SrLaAlO_4 [J]. *Applied Physics Letters*, 2013, 102(5): 051603.
- [111] HARPER F E, TINKHAM M. The mixed state in superconducting thin films[J]. *Physical Review*, 1968, 172(2): 441-450.
- [112] WELP U, KWOK W K, CRABTREE G W, et al. Angular dependence of the upper critical field of $\text{YBa}_2\text{Cu}_3\text{O}_{7-\delta}$ single crystals[J]. *Physical Review B*, 1989, 40(7): 5263-5265.
- [113] LIU Y, KO E K, TARN Y, et al. Superconductivity and normal-state transport in compressively strained $\text{La}_2\text{PrNi}_2\text{O}_7$ thin films[J]. *Nature Materials*, 2025, 24(8): 1221-1227.
- [114] HAO B, WANG M, SUN W, et al. Superconductivity in Sr-doped $\text{La}_3\text{Ni}_2\text{O}_7$ thin films[J]. *Nature Materials*, 2025, 24(11): 1756-1762.
- [115] TARN Y, LIU Y, THEUSS F, et al. Reducing the strain required for ambient-pressure superconductivity in Ruddlesden-Popper bilayer nickelates[J]. *Advanced Materials*, 2026, 38(16): e20724.
- [116] LI P, ZHOU G, LV W, et al. Angle-resolved photoemission spectroscopy of superconducting $(\text{La,Pr})_3\text{Ni}_2\text{O}_7/\text{SrLaAlO}_4$ heterostructures[J]. *National Science Review*, 2025, 12(10): nwaf205.
- [117] WANG B, ZHONG Y, ABADI S, et al. Electronic structure of compressively strained thin film $\text{La}_2\text{PrNi}_2\text{O}_7$ [A]. Preprint at arxiv.org/abs/2504.16372 (2025).
- [118] SUN W, JIANG Z, HAO B, et al. Observation of superconductivity-induced leading-edge gap in Sr-doped $\text{La}_3\text{Ni}_2\text{O}_7$ thin films[A]. Preprint at arxiv.org/abs/2507.07409 (2025).
- [119] ZHANG Y, LIN L F, MOREO A, et al. Magnetic correlations and pairing tendencies of the hybrid stacking nickelate superlattice $\text{La}_7\text{Ni}_5\text{O}_{17}$ ($\text{La}_3\text{Ni}_2\text{O}_7/\text{La}_4\text{Ni}_3\text{O}_{10}$) under pressure[J]. *Physical Review B*, 2025, 112(2): 024508.
- [120] LYU W, NIE Z, WANG H, et al. Preparation and optimization of high-temperature superconducting Ruddlesden-Popper nickelate thin films[J]. *Acta Physica Sinica*, 2025, 74(22): 227403.
- [121] GUREVICH A. Enhancement of the upper critical field by nonmagnetic impurities in dirty two-gap superconductors[J]. *Physical Review B*, 2003, 67(18): 184515.

REFERENCES

- [122] DU X, WANG Y L, LI Y D, et al. Dichotomy in low- and high-energy band renormalizations in trilayer nickelate $\text{La}_4\text{Ni}_3\text{O}_{10}$: A comparison with cuprates[J]. Physical Review Letters, 2025, 135(14): 146506.
- [123] CHEN Z, HUANG H. The nickelate bridge between cuprate and iron-based superconductivity[J]. Quantum Frontiers, 2025, 4(1): 17.

APPENDIX A AI USAGE DECLARATION

In the process of writing this dissertation, I have utilized the AI language model, Gemini, developed by Google, to assist in polishing and refining the clarity and quality of the text. The AI was used specifically to enhance the fluency and cohesiveness of the language, while the core content, scientific ideas, analysis and conclusions remain my own. I have reviewed all suggestions provided by the AI and ensured that they align with my research objectives and academic standards.

ACKNOWLEDGEMENTS

These acknowledgements are dedicated to all those who have supported and encouraged me throughout my master's study, and throughout my life.

First and foremost, I would like to express my deepest appreciation to my supervisor, Prof. Zhuoyu Chen. He has provided invaluable guidance in shaping my research direction and refining my scientific thinking toward important problems. His patience and kindness have allowed me to grow at my own pace and gradually find my footing in research. Under his mentorship, I truly felt the wind of freedom blow throughout my master's study. I am sincerely grateful for his continuous support and warm encouragement during the most challenging moments of my research.

I would also like to thank all the teachers and members of our research group: Dr. Xiaoping Zhang, Dr. Haoliang Huang, Dr. Peng Li, Dr. Yueying Li, Dr. Heng Wang, Dr. Guangdi Zhou, Dr. Cui Ding, Dr. Wenhua Song, Fengzhe Wang, Wei Lv, Yaqi Chen, Lizhi Xu, Xianfeng Wu, Fei Peng, Enhao Zhang, Wei Wang, and Zhanzhan Zhang. I am deeply grateful to my colleagues for their generous help in experiments and study. Discussions with them have been a constant source of inspiration, from which I have learned immensely. The collaborative and supportive atmosphere in the laboratory has contributed significantly to my growth as a master's student. I would also like to sincerely thank Prof. Dawei Shen and Dr. Zhicheng Jiang for their valuable support during the ARPES experiments.

Finally, I would like to express my heartfelt gratitude to my parents. Their unconditional love, understanding and support have always been the strongest foundation of my academic journey. I am also deeply grateful to my petite amie. Her tenderness, companionship and quiet strength have carried me through this long journey with warmth and joy.

I would like to end with a reflection inspired by Maupassant: life, you see, is neither as bad nor as good as one believes. At times, we are so fragile that a single sentence can bring us to tears; at other times, we realize that, gritting our teeth, we have already walked a long, long way. I hope I can always carry the courage to step into whatever journey lies ahead.

RESUME AND ACADEMIC ACHIEVEMENTS

Resume

Zihao Nie was born in 2001, in Jingzhou, Hubei Province, China.

He began his bachelor's study in the Institute for Advanced Study, Shenzhen University in September 2019, majoring in physics, and got a Bachelor of Science degree in June 2023.

He has started to pursue a master's degree in Physics in the Department of Physics, Southern University of Science and Technology since September 2023.

Awards: Outstanding Graduate, awarded by Shenzhen University. Outstanding Innovative Talent Scholarship (First Prize, three consecutive years), Star of Double Innovations Scholarship (Group) (First Prize), and Star of Learning Scholarship (Second Prize), awarded by Shenzhen University. National Scholarship for Graduate Students (Master's), 2025.

Academic Achievements during the Study for an Academic Degree

Academic Articles:

- [1] **Nie, Z.**[†], Li, Y.[†], Lv, W.[†], Xu, L.[†], Jiang, Z.[†], Fu, P., Zhou, G., Song, W., Chen, Y., Wang, H., Huang, H., Lin, J., Jia, J.-F., Shen, D.*[†], Li, P.*[†], Xue, Q.-K.*[†], Chen, Z.*[†]. Superconductivity and electronic structures of nickelate thin film superstructures. *Nature* **652**, 628-634 (2026). ([†] These authors contributed equally; * denotes the corresponding author.)
- [2] Zhou, G.[†], Lv, W.[†], Wang, H.[†], **Nie, Z.**[†], Chen, Y., Li, Y., Huang, H., Chen, W.-Q., Sun, Y.-J., Xue, Q.-K.*[†], Chen, Z.*[†]. Ambient-pressure superconductivity onset above 40 K in (La,Pr)₃Ni₂O₇ films. *Nature* **640**, 641-646 (2025).
- [3] Lv, W., **Nie, Z.**, Wang, H., Chen, Y., Huang, H., Zhou, G., Xue, Q.-K., Chen, Z.*. Preparation and optimization of high-temperature superconducting Ruddlesden–Popper nickelate thin films. *Acta Physica Sinica* **74**, 227403 (2025).